ABSTRACT

HARIDASAN, VRINDA. Tunable Microwave Filter Design Using Thin-Film Ferroelectric Varactors. (Under the direction of Dr. Michael B. Steer.)

Military, space, and consumer-based communication markets alike are moving towards multi-functional, multi-mode, and portable transceiver units. Ferroelectric-based tunable filter designs in RF front-ends are a relatively new area of research that provides a potential solution to support wideband and compact transceiver units. This work presents design methodologies developed to optimize a tunable filter design for system-level integration, and to improve the performance of a ferroelectric-based tunable bandpass filter. An investigative approach to find the origins of high insertion loss exhibited by these filters is also undertaken.

A system-aware design guideline and figure of merit for ferroelectric-based tunable bandpass filters is developed. The guideline does not constrain the filter bandwidth as long as it falls within the range of the analog bandwidth of a system's analog to digital converter. A figure of merit (FOM) that optimizes filter design for a specific application is presented. It considers the worst-case filter performance parameters and a tuning sensitivity term that captures the relation between frequency tunability and the underlying material tunability. A non-tunable parasitic fringe capacitance associated with ferroelectric-based planar capacitors is confirmed by simulated and measured results. The fringe capacitance is an appreciable proportion of the tunable capacitance at frequencies of X-band and higher. As ferroelectric-based tunable capacitors form tunable resonators in the filter design, a proportionally higher fringe capacitance reduces the capacitance tunability which in turn reduces the frequency tunability of the filter. Methods to reduce the fringe capacitance can thus increase frequency tunability or indirectly reduce the filter insertion-loss by trading off the increased tunability achieved to lower loss. A new two-pole tunable filter topology with high frequency tunability ($> 30\%$), steep filter skirts, wide stopband rejection, and constant bandwidth is designed, simulated, fabricated and measured. The filters are fabricated using barium strontium titanate (BST) varactors. Elec-

tromagnetic simulations and measured results of the tunable two-pole ferroelectric filter are analyzed to explore the origins of high insertion loss in ferroelectric filters. The results indicate that the high-permittivity of the BST (a ferroelectric) not only makes the filters tunable and compact, but also increases the conductive loss of the ferroelectric-based tunable resonators which translates into high insertion loss in ferroelectric filters.

Tunable Microwave Filter Design Using Thin-Film Ferroelectric Varactors

by
Vrinda Haridasan

A dissertation submitted to the Graduate Faculty of
North Carolina State University
in partial fulfillment of the
requirements for the Degree of
Doctor of Philosophy

Electrical Engineering

Raleigh, North Carolina

2012

APPROVED BY:

Dr. Jon-Paul Maria	Dr. John F. Muth
Dr. Griff Bilbro	Dr. Michael B. Steer Chair of Advisory Committee

DEDICATION

To my dear and supportive husband, son and parents ...

BIOGRAPHY

Vrinda Haridasan received her Bachelor of Engineering (B.E.) degree in Electronics Engineering from Mumbai University's Vivekanand Education Society's Institute of Technology, India in 1997, and her M.S. degree in Electrical Engineering from the University of North Carolina at Charlotte in 1999. She worked in Teradyne Inc., Agoura Hills, CA from 1999 to 2004. As a hardware design engineer at Teradyne Inc., she designed, developed and verified Field Programmable Gate Arrays (FPGAs) and Application Specific Integrated Circuits (ASIC) for automatic test equipment (ATE) systems, and performed board-level validation of analog and digital features on the ATE systems. She was the technical prime for system level test development and validation of digital, analog, mixed-signal electronic and electromechanical systems at Solectron Corp. (now Flextronics), Creedmoor, NC, from 2005 to 2006.

She joined the PhD program in Electrical and Computer Engineering (ECE) at North Carolina State University (NCSU), Raleigh, North Carolina in August 2006. From 2006 to 2007, she was a research assistant at NCSU, where she worked on the barium strontium titanate based tunable filter design project. She went on to work at Vadum Inc., Raleigh, NC, on various RF and microwave design and development projects from 2008 to 2010. She returned back to work as a research assistant in the ECE department of NCSU in November 2009. Her main research interests include design, characterization, modeling, simulation, calibration and measurement of tunable RF, and microwave devices based on barium strontium titanate thin-films.

ACKNOWLEDGEMENTS

My dissertation research owes much to the continuous guidance, support, enthusiasm and vision of my thesis advisor, Dr. Michael B. Steer. I am deeply indebted to him for providing me the opportunity and freedom to explore my research interests while at the same time keeping me on track with his insightful questions and honest advice. Special thanks to Dr. Jon-Paul Maria for his support and stimulating research discussions. I would like to thank other members of my committee, Dr. John F. Muth and Dr. Griff Bilbro, for their valuable suggestions. I would also like to thank Dr. Doug Barlage, Dr. Angus Kingon and Dr. Kevin Gard for their comments and discussions.

Dr. Steven Lipa's help in the laboratory on numerous occasions is greatly acknowledged. Many thanks to Dr. Zhiping Feng for her help and many useful research discussions. It has been a pleasure to work with Dr. Peter Lam who worked on the filter processing side of the research and was always willing to provide his support and help. I would also like to thank Dr. Tom Jackson and Israel Ramirez from the Electrical and Computer Engineering Department at Penn State University for their knowledge and support in fabricating the filters. Many thanks to Siobhan Strange, Patsy Ashe, Elaine Hardin and Claire Sideri for always going out of their way to ensure that all the administrative tasks were handled smoothly.

I would like to thank my colleagues, Austin Pickles, Dr. Glenn Garner, Dr. Chris Saunders, Dr. Greg Mazzaro, Dr. Rob Harris, Justin Lowry, Dr. Jie Hu, Dr. Nikhil Kriplani, Dr. Alan Victor, Spencer Johnson, Suresh Venkatesh, and Shivam Priyadarshi for providing an enriching and enjoyable work environment at school, for their friendship and sense of humor. I am thankful to Dr. Aaron Walker and Dr. Mark Buff for their support while working at Vadum Inc.

Work in this dissertation was supported by Defense MicroElectronics Activity (DMEA) and by Office of Naval Research (ONR) as a subcontract from BAE, Inc. I would like to thank them for sponsoring this research. I would also like to acknowledge the customer support provided by Sonnet Software and Computer Simulation Technology (CST).

Special thanks are due to my family as this dissertation would not have been possible without their unwavering support. I would like to thank my husband, Vijoy, and son, Vidyuth, for their positive encouragement and enthusiasm through my graduate school experience. I would also like to thank my parents for teaching me the importance of perseverance and the power of positive thinking.

TABLE OF CONTENTS

LIST OF TABLES

LIST OF FIGURES

Chapter 1

Introduction

1.1 Trends In The Research Area of Interest

In the area of modern communications; military, space, and consumer markets are moving towards a single multi-functional and multi-band unit. The navy's multi-band terminal (NMT), designed by Raytheon, supports stealthy multi-band protective communications using a single device [10, 11]. NMT provides seamless connection between submarines or ships and the global communication grid. Multi-band transponders are often used on a satellite communication space-craft to serve different markets. Using a single transponder operating on different frequency bands makes the device lighter — a very desirable feature for being on-board a spacecraft [8]. A smart phone is not only a very popular multi-functional device in the consumer market, its popularity is making inventory-control companies and the military interested in exploiting its capabilities to serve their needs. Mobile wireless devices are gaining popularity in all these markets because of their compactness and portability. The onslaught of new technologies is pushing mobile device manufacturers towards user equipment that can operate in different parts of the world and work in different formats. Supporting wireless 3G/4G technologies, bluetooth, radio-frequency identification devices (RFID), and Wi-Fi together with voice and high-speed data operations require wireless devices to function as multi-mode devices [12].

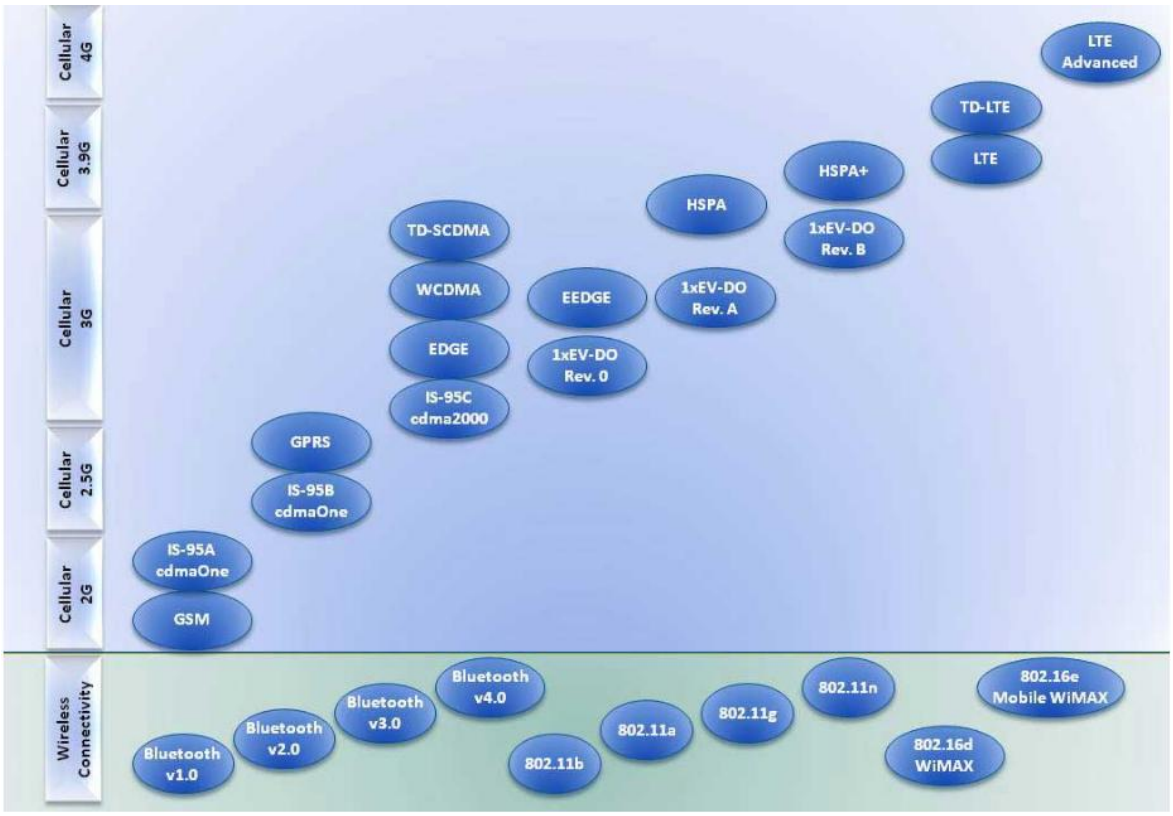

Figure 1.1: Evolution of different wireless and cellular standards in the consumer market. Credit: Aeroflex Test Solutions. After Wireless Design Magazine [1].

The multi-mode capability also allows the transceiver equipment to support both legacy customers as well as new services [13]. Figure 1.1 shows the different versions of the wireless and cellular standards in the consumer market. Some of the wireless standards like the global system for mobile communications (GSM) operate on multi-frequency bands. A quad-band GSM world phone operates at 850 MHz, 900 MHz, 1800 MHz and 1900 MHz.

In short, modern transceivers require wide tuning bandwidths, and must be compact and portable to support multi-mode and multi-band operations.

1.2 Scope Of The Research

Although communications over multi-octave tuning bandwidths is required, instantaneous broadband coverage is rarely required [14]. Frequency coverage by an RF front-end can be achieved in different ways: digitizing data immediately after the antenna and moving all further processing to the digital domain; using wideband analog circuitry with sub-sampling architectures; using discrete fixed narrowband circuitry for different frequency bands; or using a single, or a few, tunable narrowband circuits.

Moving all the processing to the digital domain by digitizing data immediately after the antenna is often stated as the ultimate goal of Software Defined Radios (SDRs). Although this would provide complete flexibility in being able to handle current and future wireless standards, the full SDR concept places currently unachievable demands on the performance and power consumption of analog to digital converters (ADCs). Wideband analog circuitry is an achievable option but the transceiver performance could be compromised due to the limited linearity of front-end components [15].

In all modern radio architectures the signal is eventually digitized with an almost inverse relationship between the number of digitizer bits (that relates to the dynamic range of conversion) and the number of samples per second (that determines the instantaneous input bandwidth). The often significant power consumed by the ADC is a function of both the number of bits and the sampling rate. Consequently, when the instantaneous desired RF coverage is narrow band, and the particular desired channel is known, it is typical to use fixed and perhaps channelized narrowband filtering and a low frequency ADC. Figure 1.2 is the block diagram of a typical transceiver. The transmit and receive RF-front end sections have many bandpass filters (highlighted in Figure 1.2) that each work at different center frequencies to provide the wideband support.

As the functionality and frequency bands supported by these transceivers grow; the number, size and the cost of the RF front-end filter modules grows. There is thus clearly a need for better (in terms of performance, feature size and device portability) frequency agile RF front-

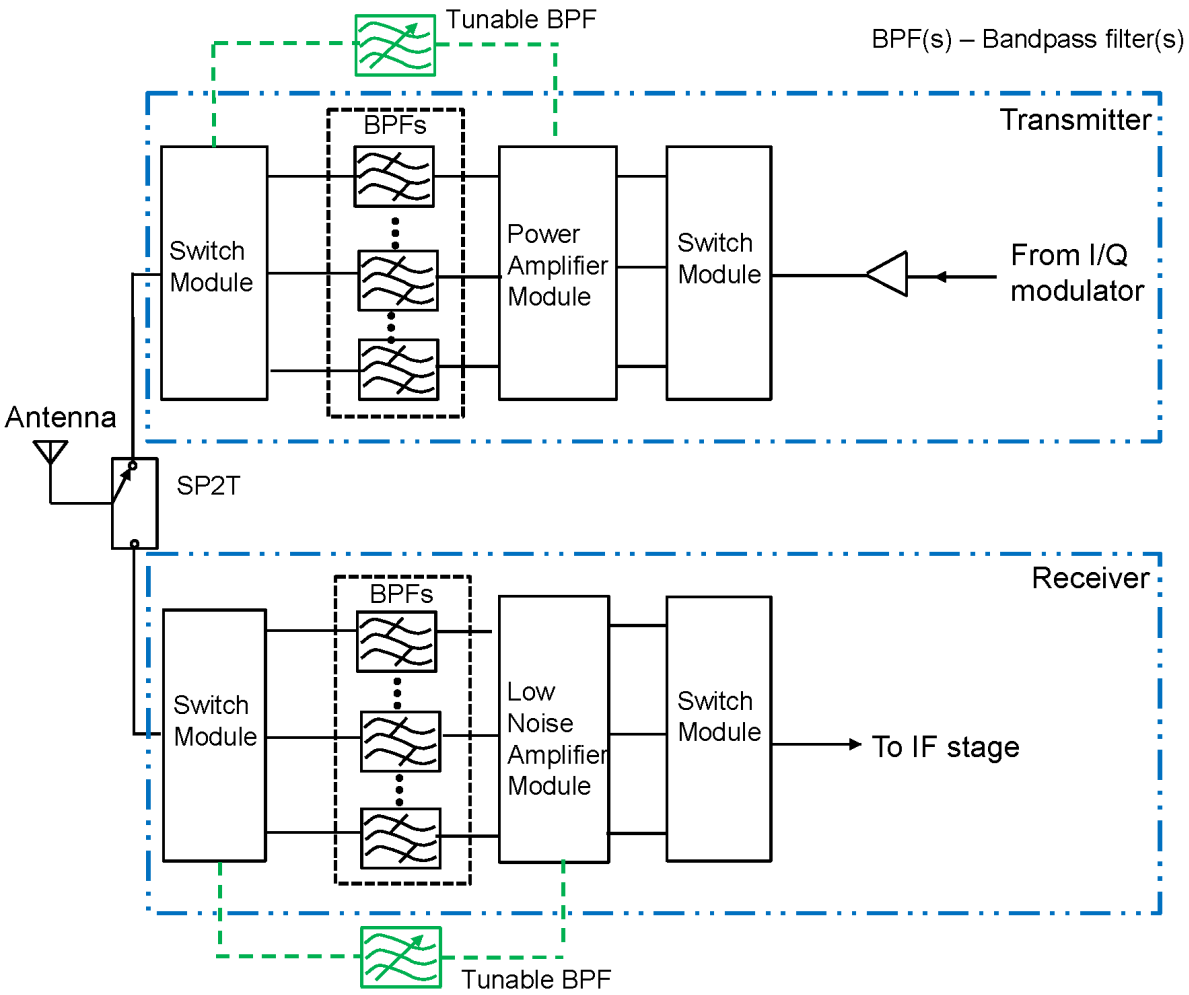

Figure 1.2: Block diagram of a typical transceiver widely used in communication systems today. There are many bandpass filters in the RF-front-end sections of the transmitter and receiver sections. They can be replaced in the future by a single (as shown) or a few tunable bandpass filter(s) tuned to different center frequencies by an external mechanical, magnetic or electronic control [2].

end filters.

Tunable filters can replace (as shown in Figure 1.2) the many bandpass filters with a single or a few filter(s) that can operate at different center frequencies using an external mechanical, magnetic or electronic control. There are however many different challenges associated with filters based on their topology and type of control used. This dissertation focusses on electronically tunable ferroelectric-based bandpass filter design.

1.3 Dissertation Motivations

Several different tunable ferroelectric-based bandpass filter designs have been discussed in the literature [4, 16, 17, 18, 19, 20, 21, 14].

A very popular metric that has been used by researchers to compare tunable RF and microwave filters in the past was defined by Pleskachev and Vendik [22, 23]. This metric works well to compare tunable filters with different topologies that are designed for different system requirements. However, there is no metric discussed in the literature that can be used in optimizing a tunable filter design for system-level integration.

Bandpass tunable filters have traditionally been designed to maintain a constant bandwidth in the entire tuning range. Various design guidelines have been developed to support the constant bandwidth approach [24, 25, 26]. Maintaining a constant bandwidth in the entire tuning range often increases the filter insertion-loss. This approach of constraining the filter-bandwidth is not necessary with the advent of newer ADCs in the market that have wide analog bandwidths (a 12-bit ADC with an analog bandwidth of 1 GHz is readily available) unless the filter tunability is very high ($> 30\%$ tunability) and the topology renders itself to increasingly wider filter-bandwidths during tuning.

A trade-off exists between filter tunability, insertion loss and bandwidth. Ferroelectric filters have typically been known to have high insertion loss especially when tunability is high (> 5 dB worst case insertion loss when tunability is close to 20%) [18, 19]. A filter designed with small filter-tunability ($< 15\%$ tunability) can often yield low-insertion loss ferroelectric based tunable

filters. Similarly, a wide-bandwidth filter can be designed to lower the insertion-loss. However, filters with narrow and moderate filter-bandwidths (< 1 GHz) and very high-tunability ($> 30\%$ tunability), often give rise to high-insertion loss ferroelectric filters. There is thus a need to improve the performance characteristics of such ferroelectric filters.

As discussed above, the insertion loss of ferroelectric-based tunable filters is known to be high although a deterministic approach to isolate the source of loss in these filters by analyzing and drawing inferences from the measured and EM simulation results has not been established.

1.4 Research Questions

The following are the research questions being addressed in this dissertation:

1. How can tunable ferroelectric filters be designed to optimize for system integration?
2. How can higher performance ferroelectric filters be designed?
3. Why do ferroelectric filters have high insertion loss?

1.5 Original Contributions

A figure of merit (FOM) was developed to make a tunable filter design more suited to be part of a system. A ferroelectric filter that improved the tunability ($> 30\%$) while keeping the bandwidth constant was designed. The root-cause of high insertion loss in ferroelectric filters was investigated. This section lists the original contributions. Appropriate chapters where these original contributions are elaborated on are indicated. The contributions from others in the research group are explicitly stated whenever a co-development effort led to the fulfillment of a task.

In the original contributions listed below, all the filters were fabricated using lithography and material processing techniques by other members of the research group.

1. A design guideline and a figure of merit (FOM) for a tunable ferroelectric filter design was developed to optimize the design for system-level integration. Filters were fabricated

based on this FOM. The simulated and measured results were compared. (Chapter 4)

2. An electromagnetic (EM) model for a barium strontium titanate (BST)-based planar capacitor was developed to study the parasitic effect associated with these capacitors. Simulated and measured results were used to confirm the existence of a parallel non-tunable fringe capacitance that reduces the frequency tunability in microwave filters at high frequencies (X-band and above). Measurements were performed by other members of the research group for this particular task. (Chapter 3)

3. A two-pole tunable ferroelectric filter having a wide-tuning range and constant bandwidth was designed, simulated, fabricated and measured. Design work included working on circuit design as well as on the fabrication mask design. (Chapter 5).

4. The origins of high insertion loss associated with ferroelectric filters were explored and isolated using electromagnetic simulators and measured results. (Chapter 6).

5. A ferroelectric filter with a quasi-elliptic filter response was designed, fabricated and measured. (Appendix A)

1.6 Published Works

1.6.1 Journal Papers

1. V. Haridasan, P. G. Lam, Z. Feng, W. M. Fathelbab, J.-P. Maria, A. I. Kingon, and M. B. Steer, "Tunable ferroelectric microwave bandpass filters optimised for system-level integration," *IET Microwave, Antennas and Propagation*, vol. 5, no. 10, pp. 1234-1241, Jul. 2011.

2. P. G. Lam, V. Haridasan, Z. Feng, M. B. Steer, A. I. Kingon, and J.-P. Maria, "Scaling issues in ferroelectric barium strontium titanate tunable planar capacitors," *IEEE Trans. Ultrason., Ferroelectr., Freq. Control*, vol. 59, no. 2, pp. 198-204, Feb. 2012.

3. P. G. Lam, Z. Feng, V. Haridasan, A. I. Kingon, M. B. Steer, and J.-P. Maria, "The impact of metallization thickness and geometry for X-band tunable microwave filters," *IEEE Trans. Ultrason., Ferroelectr., Freq. Control*, vol. 56, no. 5, pp. 906-911, May 2009.

1.6.2 Conference Papers

1. V. Haridasan, Z. Feng, P. G. Lam, M. B. Steer, J-P. Maria, A. I. Kingon, and W. M. Fathelbab, "Bandwidth, Tunability and Insertion Loss of Microwave Bandpass Filters From 2 to 18 GHz Using BST Varactors," *Government Microcircuit Applications Conf.*, Orlando, FL Mar. 2009, pp. 517-520.

2. P. G. Lam , Z. Feng , V. Haridasan, M. B. Steer, A. I. Kingon, and J-P. Maria, "Integrated Microwave Frequency Tunable Bandpass Filter Using Barium Strontium Titanate Varactors," *IEEE Inter. Symp. On the Applications of Ferroelectrics*, Santa Re, NM, 2008, pp. 1-2.

3. Z. Feng, W. M. Fathelbab, P. G. Lam, V. Haridasan, J.-P. Maria, A. I. Kingon, and M. B. Steer, "A 6.2–7.5 GHz tunable bandpass filter with integrated barium strontium titanate (BST) interdigitated varactors utilizing silver/copper metallization," in 2009 *Radio and Wireless Symposium*, San Diego, CA, Jan. 2009, pp. 638-641.

4. Z. Feng, W. M. Fathelbab, P. G. Lam, V. Haridasan, J-P. Maria, A. I. Kingon and M. B. Steer, "Narrowband barium strontium titanate (BST) tunable bandpass filters at X-band," in 2009 *IEEE MTT-S Int. Microwave Symposium*, Boston, MA, Jun. 2009, pp. 1061-1064.

1.7 Unpublished Work

1. V. Haridasan, P. G. Lam, Z. Feng, J-P. Maria and M. B. Steer, "Electronically tunable ferroelectric bandpass filter with wide tuning range and constant bandwidth," *IEEE Trans. Microw. Theory Tech.*, In Preparation

2. V. Haridasan, P. G. Lam, J-P. Maria and M. B. Steer, "Identifying the origins of high insertion loss in interdigital ferroelectric varactor based bandpass filters," *IEEE Microwave and Wireless Components Letters*, In Preparation.

1.8 Dissertation Overview

This dissertation presents research work on tunable microwave bandpass filter design and characterization using thin-film frequency-agile ferroelectric varactors.

Chapter 2 documents the topologies and design techniques of the filter modules to meet the wide-band support required by RF front-end filters in modern transceivers as well as the state of the art performance of these front-end bandpass filters.

Chapter 3 discusses ferroelectricity and the different types of ferroelectric varactors fabricated. EM modeling of a ferroelectric varactor is performed and the results obtained are compared with results from measuring many individual planar capacitors. The existence of a parasitic non-tunable fringe capacitance that causes reduced frequency tunability at frequencies of X band and above is verified. These results can be used to design high-tunability capacitor topologies. A trade-off between the newly achieved increased tunability and insertion loss can bring down the loss of ferroelectric filters and enhance the performance of future ferroelectric based filter designs.

Chapter 4 develops a system-aware design guideline and figure of merit to optimize the performance of the tunable ferroelectric filter design. Filters are fabricated and the measured results are compared with EM simulated results. The FOM technique used widely in earlier research is compared and contrasted with the system-aware FOM. The application for which the new FOM is more suited is highlighted.

Chapter 5 presents in-depth detail of the design, simulation, operation and measured results of a new filter topology that provides constant bandwidth while also enhancing the frequency tunability of the filter.

Chapter 6 explores the reason behind the high insertion loss in ferroelectric filters by using

EM simulation tools and measured results. It isolates the source of this high-loss. These results can be used to enhance the performance of future ferroelectric filter designs.

Chapter 7 summarizes the research work performed, lists the significant results of this work and provides suggestions and topologies for future enhancements to ferroelectric filter designs.

1.9 Conclusion

This chapter discussed the trends in the research area of interest, and identified the scope of research, motivations for the research work and the questions that will be addressed by this research. Original contributions and publications were enumerated. Lastly, an overview of the entire dissertation was provided. The next chapter will present a literature review both in terms of a discussion of the different filter topologies as well as the performance of different bandpass filters published in literature using the topologies discussed.

Chapter 2

Literature Review

2.1 Introduction

Filters play a very important role in RF and microwave applications. They group (using bandpass filters) or separate (using band-stop or notch filters) the frequency ranges in the EM spectrum so that the spectrum can be used for multiple simultaneous applications with manageable interference from neighboring frequency bands. The need for wide-spectrum transceivers is on the rise due to the increase in demand for a single device that can support multi-functional, multi-standard applications. This has increased the demand for new RF front-end architectures and pre-select filter sub-modules in it. A number of stringent design specifications must be satisfied by RF front-end filters to enable concurrent spectrum usage. Newer applications in wireless communications add to the existing requirements placed on RF/microwave filters in terms of smaller size, weight and higher performance.

Bandpass filters are the most popular of the filter designs. All references to the term "filter(s)" in this dissertation will imply "bandpass filter(s)" unless they are explicitly identified otherwise. Based on their response, these filters can be classified as Butterworth (having a maximally flat passband response), Chebyshev (having steep passband to stopband transition with equi-ripple passband), Elliptic (having equi-ripple passband and stopband, and a large num-

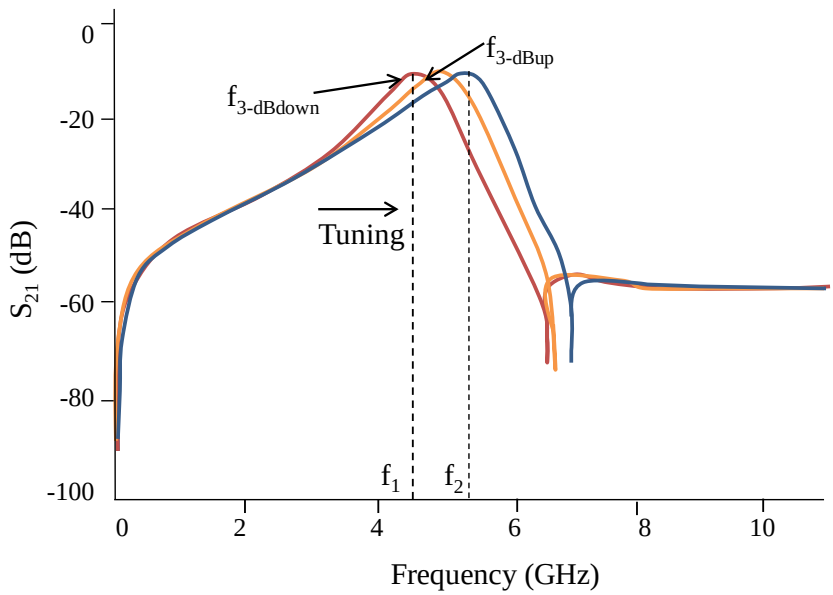

Figure 2.1: Transmission response of a typical tunable bandpass filter as the filter tunes to different center frequencies.

ber of transmission zeroes in the stopband) and Quasi-elliptic, Pseudo-elliptic or Generalized Chebyshev (with equi-ripple passband and only a few transmission zeroes in the stopband to increase the filter-skirt selectivity) filters [27].

Different filter topologies and designs that can support the demand for wideband transceivers exist. Before the filter topologies and designs are discussed, a review of filter performance parameters that are used for filter characterization and comparison are noteworthy.

2.2 Performance Metrics and Popular Terminologies In RF Front-End Filter Design

Bandpass filters can have a fixed-center frequency or can be tunable. Many fixed-frequency filters can be switched to support multiple frequency bands while a tunable filter can be tuned to support the same. A typical tunable bandpass filter shows multiple transmission responses as shown in Figure 2.1. A fixed-frequency bandpass filter has a similar response except there is

only one transmission response at a particular center frequency.

Bandwidth and insertion loss are two common parameters used to compare filters (tunable and fixed-center frequency filters). Filter bandwidth is typically defined at the 3-dB point on the transmission response. A 3-dB bandwidth is defined as the difference in frequency between the two points on the bandpass response that are 3-dB below the highest insertion loss (i.e., peak value of S_{21} dB in the graph). Bandwidth is defined as:

$$\mathrm{BW} = (\mathrm{f}_{3-\mathrm{dBup}} - \mathrm{f}_{3-\mathrm{dBdown}}), \tag{2.1}$$

where $\mathrm{f}_{3-\mathrm{dBup}}$ and $\mathrm{f}_{3-\mathrm{dBdown}}$ are defined as the 3-dB frequency points on the transmission response curve shown in Figure 2.1.

Insertion loss is the loss attributed to the filter and is defined as the geometric mean of $-S_{21}$ dB at both the 3-dB points (insertion loss is a positive number) as shown:

$$\mathrm{IL} = \sqrt{(\mathrm{IL}_{3-\mathrm{dBup}} \cdot \mathrm{IL}_{3-\mathrm{dBdown}})}. \tag{2.2}$$

The range of center frequency is an additional parameter that is presented for a tunable filter. The frequency range can also be expressed as tuning bandwidth (which is more commonly referred to as filter tunability). Filter tunability can be expressed as a percentage and is defined as

$$\%T_f = \left(\frac{f_2 - f_1}{f_1}\right) 100, \tag{2.3}$$

where f_1 and f_2 are the lower and upper center frequencies of the tuning range (see Figure 2.1).

It can also be defined as [28]

$$T_f = 2\left(\frac{f_2 - f_1}{f_2 + f_1}\right). \tag{2.4}$$

The insertion loss (IL in dB) and bandwidth (BW) are related to the filter unloaded Q-

factor (Q_U) by [29, 30, 31, 32]:

$$\mathrm{IL}|_{\mathrm{dB}} = \frac{4.34 f_0}{Q_U \mathrm{BW}} \sum_{i=1}^{n} g_i. \tag{2.5}$$

Here, f_0 is the center frequency of the filter, $\sum_{i=1}^{n} g_i$ is the sum of the reactive g-values in the lowpass filter prototype, n is the order of the filter.

The unloaded Q-factor is defined as the quality factor of a resonator when it is not connected or influenced by a load. External Q-factor is a term often used in filter design. It is different from the unloaded Q-factor (or the resonator Q). The external couplings connect the filter to the outside world [33]. External Q is determined by the amount of coupling between the first (or last resonator) to the input (or output) ports.

2.3 RF Front-End Filter Topologies

Wide tuning bandwidths required by modern RF front-end filters can be supported in two different ways - using multiple fixed frequency filters and using single or a few tunable filters as shown in Figure 2.2. The two fixed-frequency filter topologies are discussed in the following subsections. There are many different tunable filter topologies. They are hence briefly touched upon in this section and further elaborated in separate sections in this Chapter.

2.3.1 Fixed-frequency Filters With External Switches

In conventional filter design, frequency agility in RF front-end pre-selection filters is achieved by multiple fixed-frequency bandpass filters with external switches [34] as illustrated in Figure 2.3.

Six bandpass filters that cover the 1.05–2.15 GHz frequency band were designed using suspended substrate stripline technology by Packiaraj *et al.* [35]. Each of the six filters operated at a fixed-center frequency. They were connected with switches and cables so that individual filters could be switched on and off by Transistor-Transistor Logic (TTL) logic based switch control circuitry. The individual filters were placed in an aluminum housing for low cross-

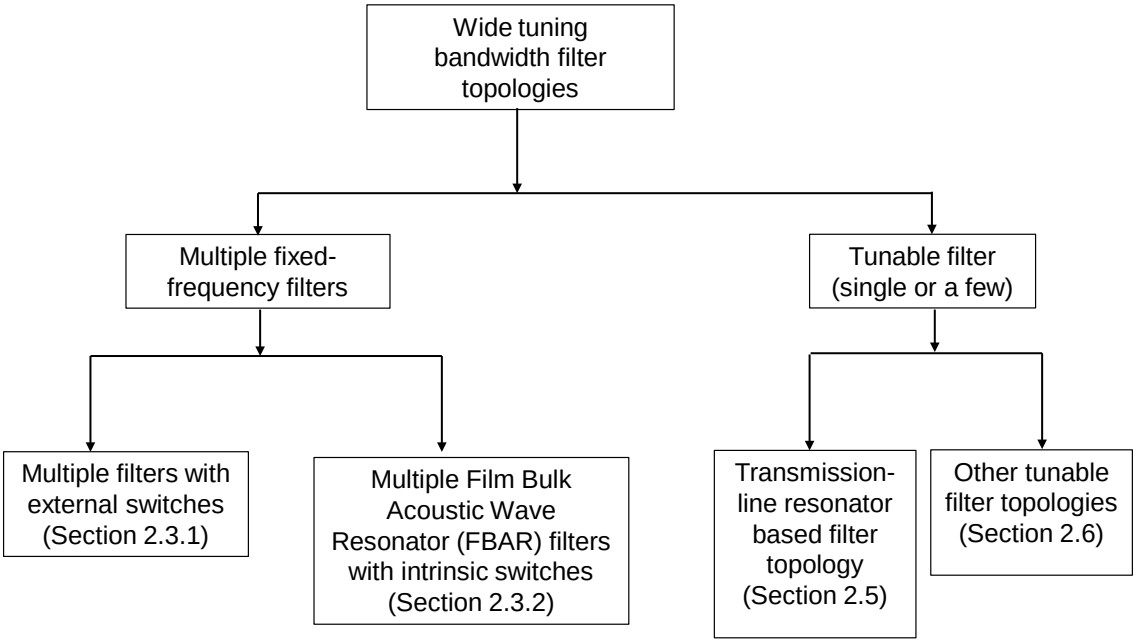

Figure 2.2: Wide tuning bandwidths required by modern RF front-end filters can be supported by multiple fixed frequency filters and single or a few tunable filter(s). These broad topology classifications can be further classified as shown.

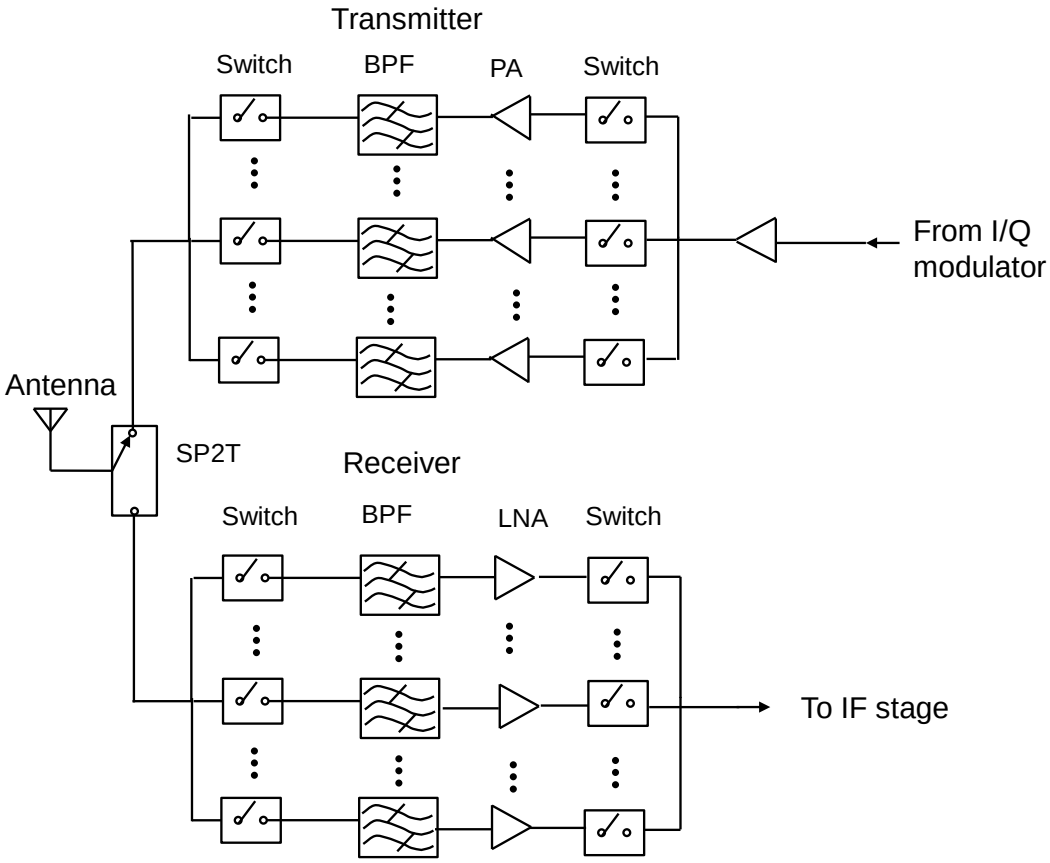

Figure 2.3: RF front-end filter topology with multiple fixed-frequency filters and external switches to support the demand for wide tuning bandwidth filters in transceivers [2].

coupling and high-isolation between the different filters. Single Pole Six Throw (SP6T) Gallium Arsenide (GaAs) Monolithic Microwave Integrated Circuit (MMIC) devices operating from 0.5–2.5 GHz were used as external switches and shielded cables were used for interconnections. The overall filter insertion loss was 4 dB with the switches and cables also contributing to the loss. The modular construction of this filter topology helped in easier testing of the individual filters, switches and cables.

The drawback of this topology is the increase in size and cost needed for wideband filter support. Research has thus focussed on alternate ways to design compact wide tuning bandwidth filters.

2.3.2 Fixed-frequency Filters With Film Bulk Acoustic Wave Resonator Filter Topology

Thin-film bulk acoustic wave resonator (TFBAR or more commonly FBAR) works on the same principal as a piezoelectric crystal (typically quartz crystal) oscillator wherein a crystal thickness that is an integer multiple of a half-wavelength generates an acoustic resonance with a resonant frequency, f_N such that:

$$f_N = (vN)/(2d). \tag{2.6}$$

Here, f_N is the resonant frequency, v is the acoustic velocity in the propagating medium, N is the integer multiplier and d is the thickness of the crystal. It is difficult to reduce the thickness of the quartz crystal to a few micrometers or lower hence quartz resonators work very well only under 200 MHz. For higher frequencies, thin-film piezoelectric materials like aluminum nitride (AlN) or zinc oxide (ZnO) are used [36]. Ferroelectric thin-films (like barium titanate or barium strontium titanate) that have high permittivities make these devices more compact compared to the conventional AlN or ZnO FBAR filters.

An intrinsically switchable FBAR filter bank using barium titanate (BTO) thin-film was

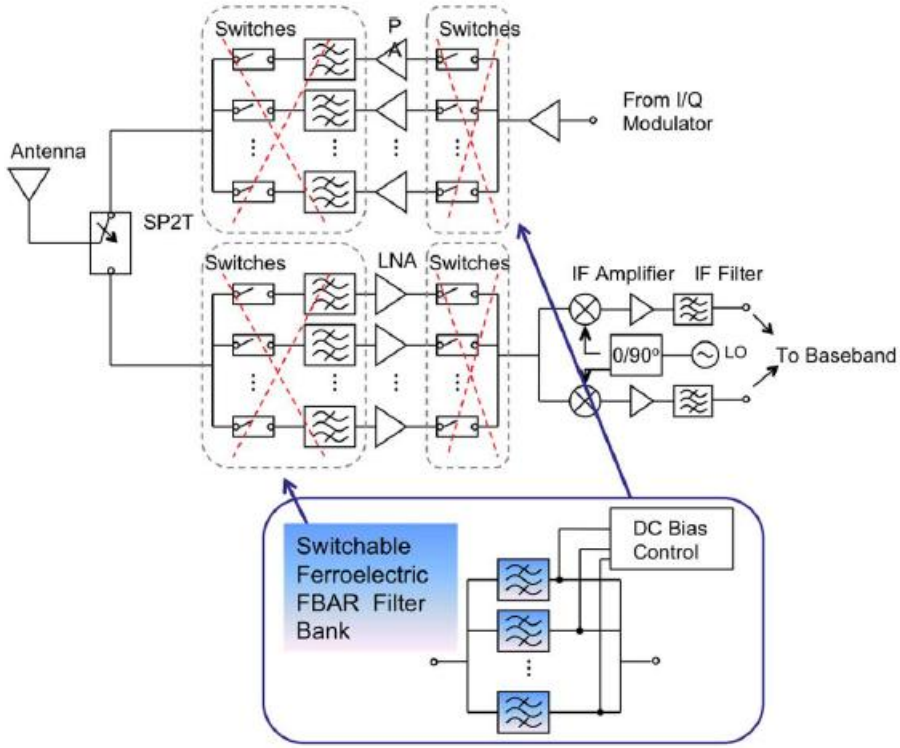

Figure 2.4: FBAR filters that can be intrinsically switched can replace conventional externally switched filter banks in wideband transceivers and cognitive radios. After Zhu *et al.* [2].

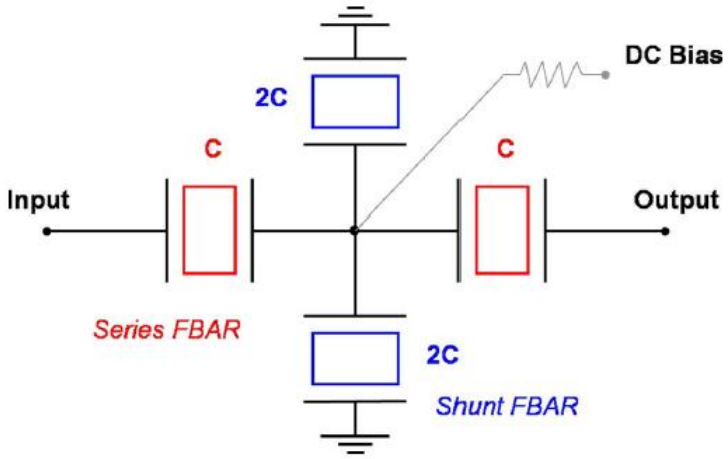

Figure 2.5: FBAR filter topology in a 1.5 stage ladder arrangement. After Zhu *et al.* [2].

reported by Zhu *et al.* [2] wherein a bias of 15 V DC turns on the filter operating at 2.4 GHz, 40 MHz bandwidth and 6.2 dB insertion loss while a -3 V DC turns off the filter with a 15 dB rejection. The electrostrictive property of BTO ferroelectric film is used to switch the filter on and off using a DC bias voltage. Figure 2.4 shows the arrangement of the FBAR intrinsically switchable filter bank and how they aim to replace the traditional external switch-based filter banks discussed in the previous subsection. The external switches in the RF path increase the filter loss. Thin-film FBAR switchable filters have smaller footprint and better filter performance than the externally switched filter banks. FBAR filters are typically arranged in a ladder type arrangement as shown in Figure 2.5. Each BTO resonator in the FBAR filter is made up of a BTO film sandwiched between two parallel platinum electrodes. The two series and two shunt resonators are placed in a 1.5 stage ladder type arrangement such that all the bottom electrodes of the resonators can be connected together and connected to a common DC bias voltage. A high resistivity Silicon Chromium (SiCr) line is used as the DC bias line. The total capacitance of the shunt resonator is twice the capacitance of the series resonator.

An FBAR filter using barium strontium titanate (BST) as the electrostrictive material is discussed in [37]. There are several advantages of using BST thin-films over BTO films. The electro-mechanical coupling for BST films is 7.0% compared to 4.0–5.0% for BTO films. The barium to strontium ratio in the BST film can be adjusted to fabricate FBARs that have no spontaneous polarization at room temperature hence a negative voltage (like that for a BTO resonator) may not be required to turn off the filter. The Q-factor for a BST based FBAR is higher than that for BTO FBAR resonators ($Q > 200$ for BST while Q is 60–100 for BTO resonators in the 1-2 GHz range). Hence the insertion loss for BST based FBAR filters is lower than their BTO counterparts [2].

2.3.3 Tunable Filter Topology

Adaptive reconfigurable RF-front ends are highly desirable in modern high-frequency systems. Tunable filters play an important role as frequency pre-selection filters in these front-ends. They

can be classified as mechanically tunable, magnetically tunable and electronically tunable [38]. Mechanical tunable filters have high unloaded Q-factors and high power-handling capability but their large size and weight restricts their use in modern transceivers where device portability is a desirable feature [8]. A Yttrium-iron-garnet (YIG) filter is one of the commonly available magnetically tunable filters. Carter presented YIG magnetic resonance based filters in [39] with a frequency range of 7-11 GHz, maximum bandwidth of 28 MHz and a worst case insertion-loss of 2 dB. RF input and output coils were arranged at right-angles and a YIG sphere was placed at the center of the axes for a single-resonator filter. A magnetic field applied to the YIG sphere together with the input RF signal interacted to produce a net magnetic moment that induced an output voltage in the RF output coil [39]. The magnetic field applied to the sphere was varied to tune the filter. These filters have very low tuning speeds on the order of tens of micro-seconds or a few milliseconds [34]. Modern tunable systems require tuning speeds in the lower micro-second and nano-second range which cannot be met by these filters. To achieve such high tuning speeds, electronically tuned filters are preferred [25].

This literature review will focus on electronically tunable filters compared to the magnetically or mechanically tuned filters. The electronically tunable filters have small size, and lower weight and are thus more suited to satisfy the requirement for portable modern transceivers. Most of the research has focussed on transmission-line resonator based electronically tunable filters. That being said, newer electronically tunable filters such as the evanescent mode and switched delay line filters have been successfully fabricated and published in recent research work. Hence, these newer topology filters will also be discussed in this chapter for completeness.

2.3.4 Summary

This section discussed broad filter categories that support wideband transceiver designs. Fixed-frequency topology using ferroelectric based FBARs (with intrinsic switches) provide one of the ways to reduce the overall size of the existing fixed-frequency design with external switches.

The other more popular approach using tunable filters is briefly discussed here with further elaborations in succeeding sections. Enabling technologies for tunable filters will be discussed in the next section.

2.4 Enabling Technologies For Tunable Filters

Three popular enabling technologies used for modern electronically tunable filters are RF micro electro-mechanical switches (MEMS), semiconductor varactors and ferroelectric materials.

RF MEMS switches and varactors have low loss and high linearity that are very desirable features in filter designs. The switches can be turned on or off using a DC actuation voltage and are typically available in the cantilever or rotary form [40]. Metal membranes with capacitive coupling form switched-capacitors are popular because of their low insertion loss, moderate actuation voltages, high linearity and fast switching speeds [40, 41]. MEMS based filter designs use two different tuning methods - analog and digital [42]. When the MEMS capacitors are varied continuously, the filter tuning is considered analog whereas when the MEMS-based tunable filter designs switch a capacitor in and out of the circuit, the filter tuning is considered digital. The digital method in filter tuning is not always desirable because the frequency response during tuning are not contiguous. Newer digital MEMS based tuning filters however use fine frequency resolution with higher number of bits that make the discrete frequency tuning appear continuous [42, 43]. MEMS based filters have complex packaging requirements and slow switching speeds in the μs range [44]. They are also prone to stiction and reliability issues.

Solid-state varactor diodes can be used as tunable capacitances that when connected in series with a transmission line, reduce the length of line required for resonance and also make the resonator tunable [3, 25]. Varactor diodes are usually operated in the reverse-bias mode by applying an external DC-bias voltage. A change in the DC-bias voltage changes the thickness of the depletion region of the varactor which in turn changes the capacitance value. Semiconductor varactors cannot typically handle high RF power levels because of the possibility of getting forward biased [45].

When a ferroelectric is used as an enabling technology, a DC bias voltage changes the permittivity of the ferroelectric material that in turn changes the capacitance of the varactors made using them [19, 14] or the inter-resonator coupling of the transmission line-resonators fabricated on them [4]. Using ferroelectric materials as a dielectric for the varactor is the most popular of the two methods. This tunable varactor is then connected in series with a transmission line to form a tunable resonator in filter design. The dielectric constant of ferroelectric materials like BST and strontium titanate (STO) are high (200-1000) which results in compact devices. When compared with MEMS devices, ferroelectric devices have faster response times in sub-microsecond ranges (compared to several microseconds for MEMS) [21], good power handling capabilities, higher reliability and no special packaging requirements. When compared with semiconductor varactors, they have higher power handling capability and potential to have higher Q at RF and microwave frequencies. As this dissertation focusses on ferroelectric based tunable filter design, Chapter 3 provides more details on the ferroelectric varactor.

2.5 Transmission-Line Resonator Based Tunable Filter Topologies

These resonator based topologies have transmission line sections that are made tunable using different enabling technologies. A number of resonators are coupled together in a certain topology to form filters of a specific order. There are many different transmission-line based topologies discussed in literature, a few of them will be discussed in the following sub-sections.

2.5.1 Combline Filter Topology

A combline and a modified combline filter are discussed in Chapters 4 and 5. Here, the basic topology of the combline filter is discussed. The combline filter consists of coupled parallel resonators such that the coupling is constrained between the nearest neighbors. The coupled lines are all shorted on one side with the capacitor loaded on the other side as shown in

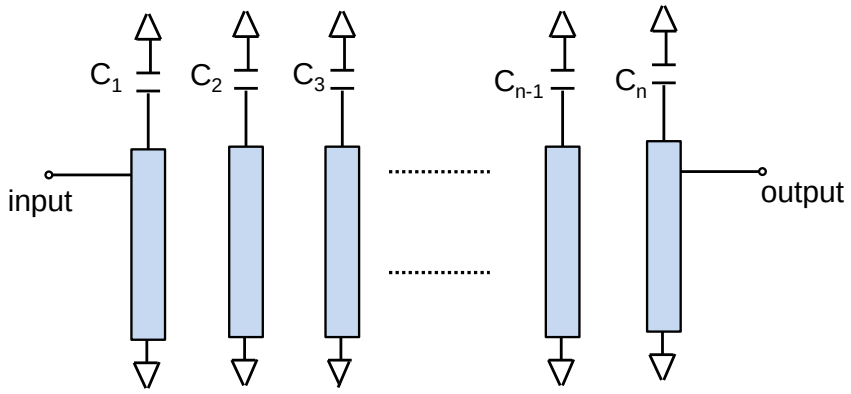

Figure 2.6: A basic combline topology is depicted here where a transmission line less than a quarter wavelength long is connected in series with a capacitor to form a resonator. Multiple resonators are coupled together to form a combline filter. The number of parallel resonators determine the filter-order.

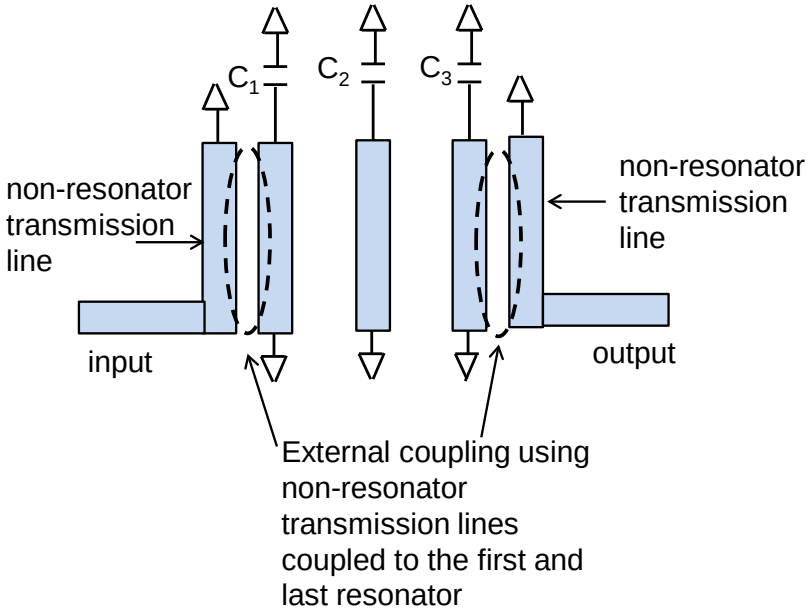

Figure 2.7: Layout of a combline filter with external coupling accomplished using non-resonator lines coupled to the first and the last resonator.

Figure 2.6. The capacitive loading of the resonator makes the filter both compact and tunable. Tapped input and output coupling (external coupling) is shown in Figure 2.6. The location of the tap-point on the first and the last resonator can be adjusted to change the external Q-factor. Two non-resonator transmission lines could also be placed close to the first and last resonators and external coupling could be accomplished without them directly making contact with the first and last resonators as shown in Figure 2.7. These external couplings act as impedance transformers. There are some advantages to using a non-contact gap for external coupling. The external Q is less affected by the resonator tuning compared to when tapped configuration is used. The high DC bias voltage applied to tune the resonator does not appear at the network analyzer RF ports [17]. The direct-tapped filters on the other hand are simpler and more compact.

The lumped capacitor makes the resonator lines $< \lambda_g/4$ long where λ_g is the guided wavelength of the resonator line in the medium of propagation at the filter midband. In the absence of the lumped capacitor, the resonator lines would be $\lambda_g/4$ long. If such a filter (i.e., with no lumped capacitor and resonator lines that are $\lambda_g/4$ long) is fabricated from a pure TEM mode transmission line such as stripline, no passband would exist [31, 46, 29]. The electric and magnetic coupling would cancel each other out without reactive loading at the ends of the resonator line elements. However, if such a filter (i.e., with no lumped capacitor and resonator lines that are $\lambda_g/4$ long) is fabricated using a microstrip transmission line, a passband would exist. This is because coupled microstrip lines are quasi TEM (not pure TEM) transmission lines and the even and odd mode phase velocities are different [31, 46, 47]. This example indicates how the same topology can result in different filter responses depending on the transmission medium (i.e., stripline or microstrip). Also, a combline filter has an asymmetrical passband response.

Hunter and Rhodes [25] designed a varactor based two-pole tunable combline filter. The filter was designed on suspended substrate stripline with a tuning frequency from 3.2 to 4.9 GHz, an insertion loss in the 3 to 5.4 dB range and a constant bandwidth of 200 MHz $\pm 10\%$. The electrical length of the resonator lines were designed to be 53° to achieve tight bandwidth

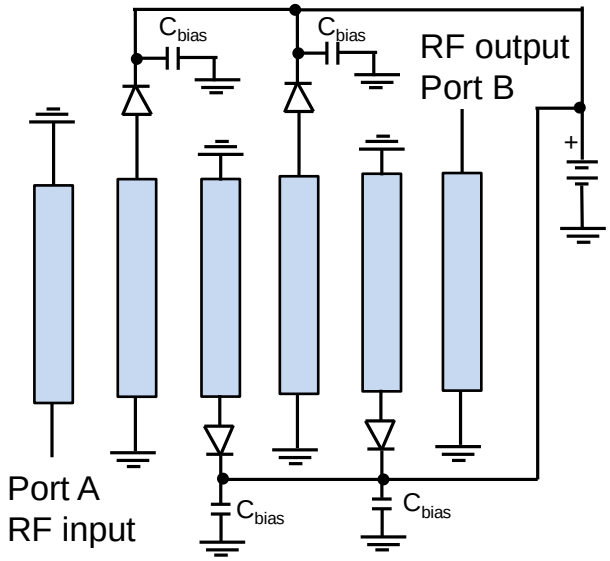

Figure 2.8: Topology of a four-pole varactor loaded inter-digital filter. After Brown and Rebeiz [3].

control.

2.5.2 Inter-digital Filter Topology

A tunable inter-digital filter has resonators that are short-circuited at one end and are connected to a varactor at the other-end. The adjacent resonators have alternate orientations. Brown and Rebeiz presented an inter-digital tunable filter with reverse-biased varactor diodes [3] on a suspended substrate stripline technology. A 127 μm thick duroid substrate with a dielectric constant of 2.2 was used. The circuit was suspended in an aluminum cavity. The topology of the four-pole inter-digitated filter operating from 700 MHz to 1.33 GHz with an insertion loss of 3 to 6 dB is shown in Figure 2.8. As shown, a shortened transmission line (i.e., $< \lambda/4$) is short-circuited at one end with a tunable varactor diode at the other end. The non-resonator inter-digital lines connected to the input and output ports are shorted lines that act as impedance transformers. The inter-digital filter has a highly-symmetric response. C_{bias} is added for biasing purposes between the bias line and ground and it acts as an RF short for the varactor and an

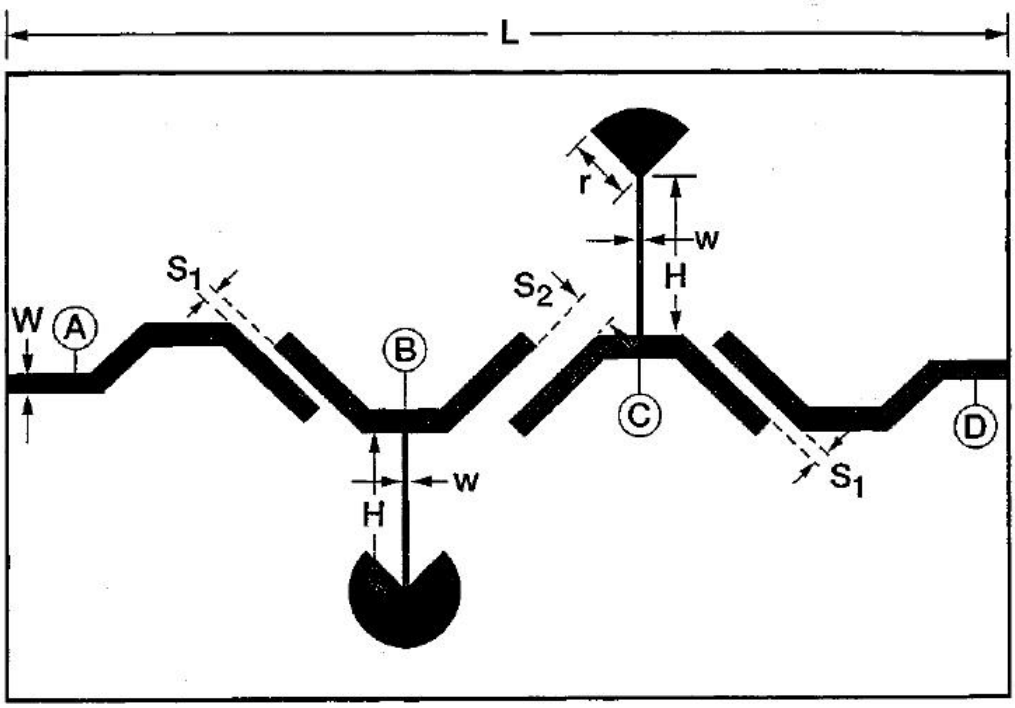

Figure 2.9: Topology of an edge-coupled ferroelectric based tunable filter. After Subramanyam *et al.* [4].

open circuit for the dc bias. The varactor diode is reverse biased. The width and spacing of the resonators determine the filter-bandwidth while the length of the resonator and the value of the tunable varactor diode determine the tuning range of the filter [3].

2.5.3 Parallel-Coupled or Edge-Coupled Filter Topology

Edge-coupled resonators typically are half-wavelength open resonators where the adjacent resonators have a coupling length of a quarter wavelength. A two-pole edge coupled microstrip technology based tunable ferroelectric filter was designed by Subramanyam *et al.* [4]. Figure 2.9 shows the edge coupled 50 Ω resonators lines. The geometry of the multi-layered microstrip structure is shown in Figure 2.10. A 254 μm (10 mils) thick lanthanum aluminate (LAO) layer, a 0.3 μm strontium titanate (STO) layer and a 0.35 μm yttrium barium copper oxide (YBCO) High Temperature Superconductor (HTS) were stacked together on a 2 μm gold (Au) ground

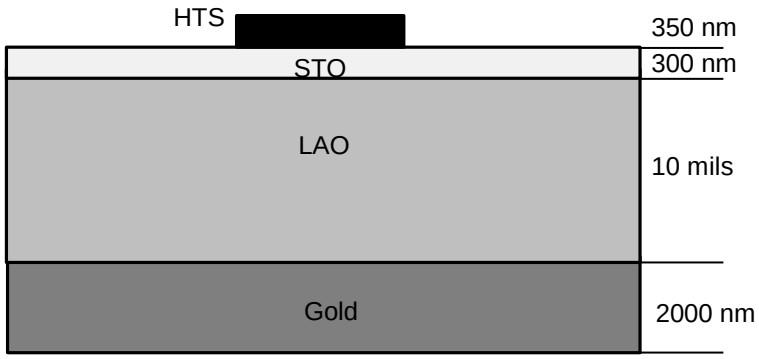

Figure 2.10: Multi-layered microstrip structure. After Subramanyam *et al.* [4].

layer. The dielectric permittivity of STO (ferroelectric material) was varied between 3000 to 300 at 77 K when the DC bias voltage varied from 0 to ±500. DC-bias was applied through the radial stubs to tune the ferroelectric STO material. Unipolar (i.e., A and C were connected to a positive bias voltage while B and D were connected to ground) and bipolar biasing (i.e., A and C were connected to a positive bias voltage while B and D were connected to a negative bias voltage) schemes were used to tune the filter. Bipolar biasing allowed for a more symmetrical passband. The filter tuned at 77 K from 17.4 GHz to 19.10 GHz (9.77 %) with an insertion loss in the 5 to 2.2 dB range.

2.5.4 Zig-Zag Hairpin-Comb Filter Topology

A typical hairpin-line filter topology is shown in Figure 2.11a in which the orientation of the hairpin resonators alternate [5]. This results in higher-coupling as the electric and magnetic couplings add up. Such structures are very useful for compact filter applications with moderate filter bandwidths. However, they do not work well for compact narrow bandwidth filter applications. A modified hairpin-comb topology is depicted in Figure 2.11b in which the orientation of the hairpin resonators are more suited for compact narrow-band applications. This is because the electric and magnetic couplings in this resonator structure tend to cancel each other [5]. The resonator couplings in this configuration results in a transmission zero. If this topology is

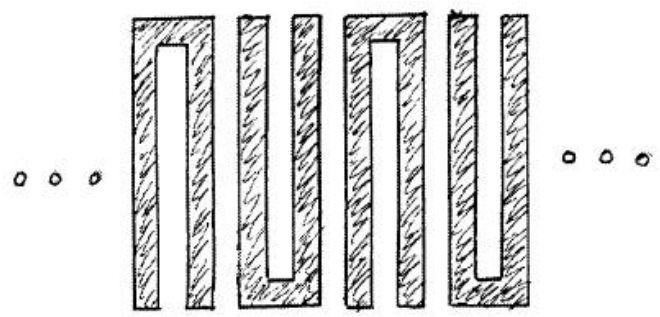

(a)

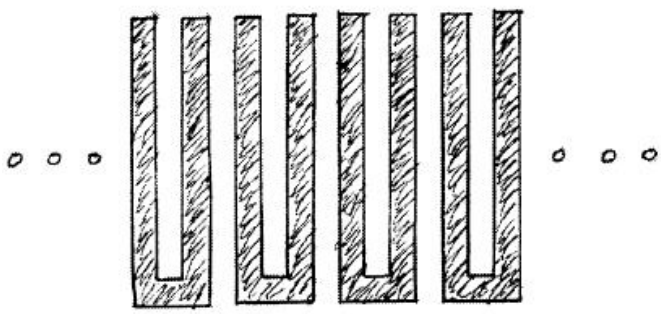

(b)

Figure 2.11: Hairpin topologies. After Matthaei [5]: (a) hairpin-line topology; and (b) hairpin-comb topology.

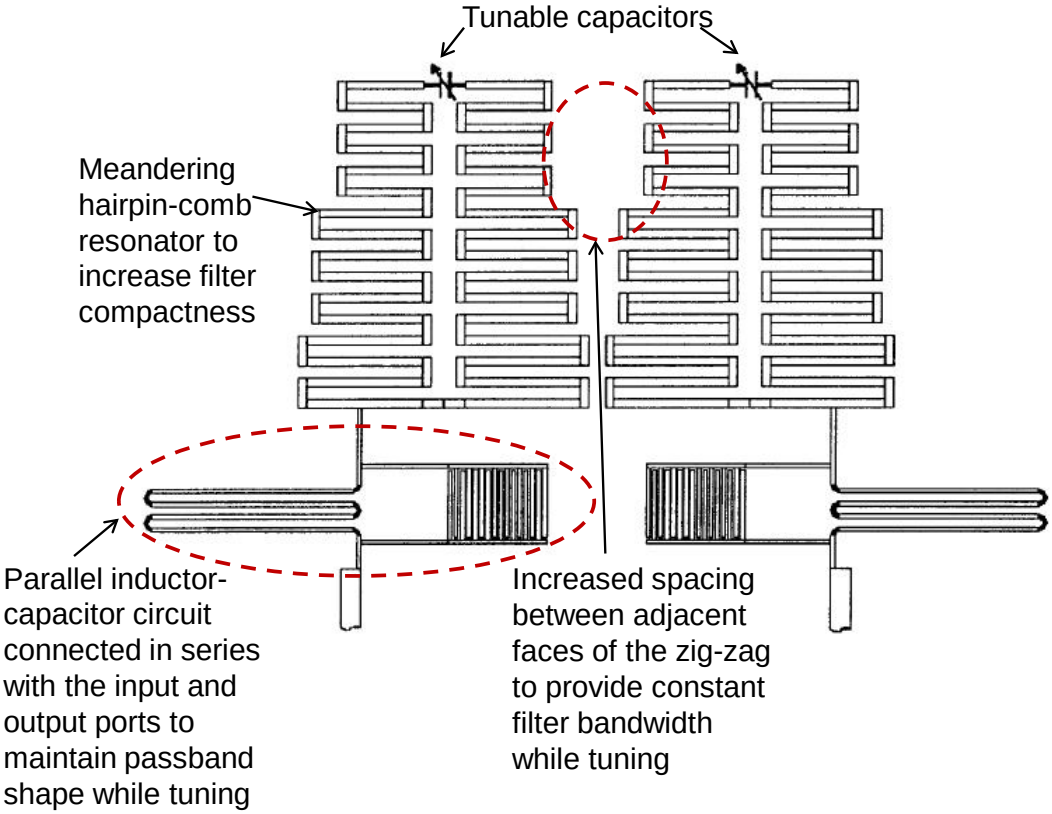

Figure 2.12: Topology of a tunable zig-zag hairpin-comb filter topology. After Matthaei [5].

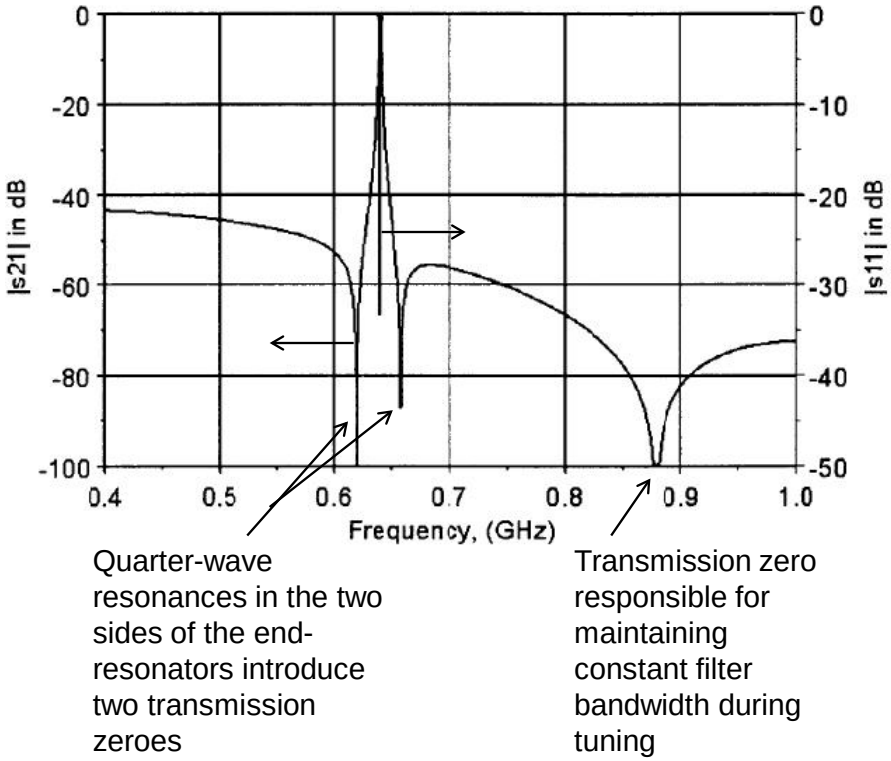

Figure 2.13: Response of a two-pole zig-zag hairpin-comb filter shown in Figure 2.12 at a particular fixed value of tunable capacitance. After Matthaei [5].

fabricated using stripline, the transmission zero occurs on the upper side of the passband while if this topology is fabricated using microstrip configuration, the transmission zero occurs on the lower side of the passband. However, a lumped capacitor added between the resonators across the open-ends of the resonator structure can be used to move the location of the transmission zero from below to above the passband [5, 48].

For certain applications where further filter compactness is desired, such as in wireless applications, a zig-zag or meandered hairpin-comb topology was proposed by Matthaei [5]. The meandering of the resonator lines create vertical and horizontal sections on the resonator. The vertical section of the resonator close to the inter-resonator gap is responsible for inter-resonator coupling while the horizontal sections on each resonator do not couple much. To provide a tunable zig-zag hairpin-comb filter topology, some modifications were made as shown in Figure 2.12. Filter bandwidth is dependent on the coupling between the resonators. To provide a constant bandwidth across the entire filter tuning range, a transmission zero was introduced in the stop-band at a frequency location such that as the passband shifted to higher frequencies during tuning, this transmission zero would prevent the widening of the passband. Based on the response of the two-pole zig-zag hairpin-comb structure, an attenuation pole (or transmission zero) existed in the stop band but it was located too far along the frequency axis to prevent the widening of the bandwidth. Hence, the transmission zero was moved to a lower frequency by introducing an equivalent negative capacitance coupling between the resonators. This was physically accomplished by widening the spacing between the zig-zag resonators at the upper end of the resonator structure while maintaining the spacing at the lower end of the resonator. To maintain the shape of the passband during tuning, the external Q between the end-resonators and the terminations should increase as the tuning frequency increases. A parallel L-C resonator introduced in series with the input and the output of the filter forced the external Q to increase approximately linearly with the increase in tuning frequency. Figure 2.13 is the filter response for a fixed value of the tunable capacitor. The quarter wave-resonances in the two sides of the end resonators caused the input and output taps to be shorted at

two-frequencies on either sides of the passband resulting in two transmission zeroes. The filter was fabricated using thallium barium calcium copper oxide (TBCCO) super conductor on a 0.508 mm magnesium oxide (MgO) substrate. This filter is appropriately suited for via-less, narrow-band, constant bandwidth, compact, quasi-elliptic response tunable filter applications.

2.5.5 Discussion

A common thread in all of these transmission-line resonator based tunable filter topologies is that the resonator is made tunable with a varactor (or tunable capacitor). These varactors in fabricated tunable filter devices are made using one of the enabling technologies described earlier. Being part of the resonator, these enabling technologies significantly influence the loss, tunability, linearity and power handling capacity of the resonators and the corresponding filters made by suitably coupling the set of resonators. Ferroelectric transmission-line resonator-based tunable filter design, the focus of this dissertation, can be designed using any of the topologies discussed in this section. In this dissertation, the three-pole combline ferroelectric filter is discussed in Chapter 4. Chapter 5 introduces a new topology for a two-pole ferroelectric filter based on the combline topology with additional modifications to increase the filter-skirt selectivity, to maintain a constant filter bandwidth and provide a wide stopband.

2.6 Other Tunable Filter Topologies

In this section newer topologies such as evanescent mode and switched-delay line tunable filters will be discussed to provide a complete picture of the different ways in which research is advancing to handle the need for better frequency agile filters.

2.6.1 Evanescent Mode Tunable Filters

Waveguide filters usually operate above a cut-off frequency for a particular mode of propagation. They have high-Q but being half-wavelength filters are typically large. A type of waveguide filter that operates below cut-off frequency is called evanescent mode filter. They have certain

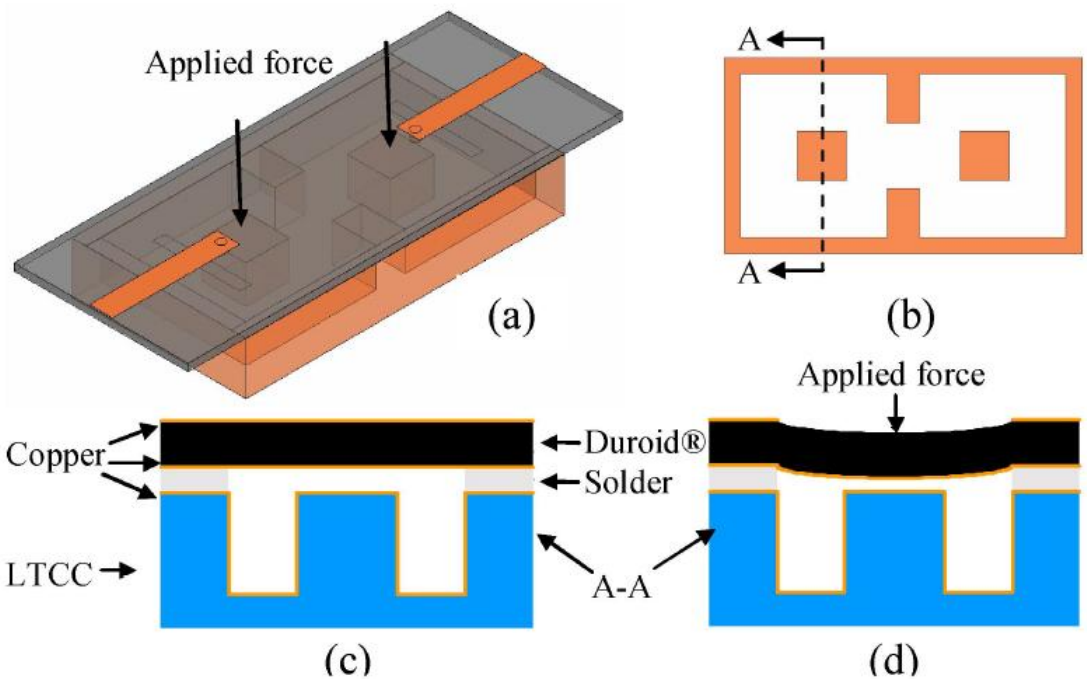

Figure 2.14: Evanescent tunable cavity filter. After Joshi *et al.* [6]: (a) a two-pole evanescent cavity filter; (b) top-view of the evanescent cavity filter showing two capacitive posts and the iris openings that controls the bandwidth of the filter; (c) cross-sectional view of the filter showing the membrane when no force is applied by the piezoelectric actuator; and (d) cross-sectional view of the filter showing the membrane bent inward due to a force applied by the actuator that changes the capacitance and the tuning frequency of the filter.

desirable features such as small size, high-Q and improved spurious-free regions [6]. When a waveguide operates below the cut-off frequency, it acts as an inductive element [49]. By themselves, these evanescent cavities are non-propagating — evanescent as the name suggests are waves that do not propagate. When such cavities are loaded with capacitive elements, they become capacitively loaded cavity resonators that can be coupled to form filters. Evanescent waveguide filters are waveguide coupled versions of combline filters [50]. The screws at the junction of the cut-off and the conventional waveguides establishes a TEM mode in a direction normal to the axis of the waveguide. The propagation through the evanescent cavity filter is through coupled TEM modes.

In tunable transmission-line resonator filters the inductive element is the transmission line. The overall unloaded Q of such resonator-based filters is dependent on the unloaded Q of the capacitors and the unloaded Q of the inductive element. The inductive element in evanescent mode filters is the shortened waveguide cavity that has a far greater unloaded Q (> 1000) compared to the transmission lines. The overall unloaded Q-factor of evanescent-mode filters can thus be potentially higher than that of transmission-line resonator based filters. The evansecent mode cavity resonator using polymer-based fabrication loaded by two parallel-plates is known to have a very high-overall unloaded Q of 1940 [51].

A widely tunable high-Q evanescent air-filled cavity bandpass filter designed on a Low Temperature Co-fired Ceramic (LTCC) substrate was discussed by Joshi *et al.* [6]. A Rogers Duroid® flexible substrate acts as a membrane for the tunable capacitor and forms the top of the filter as shown in Figure 2.14a. There are two evanescent cavity resonators to provide a two-pole filter response. The coupling between them is controlled by irises as shown in the Figure 2.14b. A capacitive post is added to the center of each evanescent cavity resonator which reduces the center frequency of each resonator from 21.21 GHz to 4.16 GHz. The cross-section of the filter in Figure 2.14c shows the static state of the filter without any force applied by the piezoelectric actuator. A piezoelectric actuator was used to move the membrane causing a change in capacitive loading thereby tuning the filter. Figure 2.14d shows the bent membrane on application of force by the piezoelectric actuator. The filter was tuned in the 2.71–4.03 GHz range with an insertion loss in the 1.3-2.4 dB range. The unloaded Q of the resonator was in the 360-700 range. Piezoelectric actuators are not very popular because of the overall increased filter size, high power consumption and hysteresis effects [52]. A MEMS based tunable evanescent cavity resonator discussed by Liu *et al.* [52] that is electrostatically activated aims to resolve the disadvantages of the piezoelectrically tunable design.

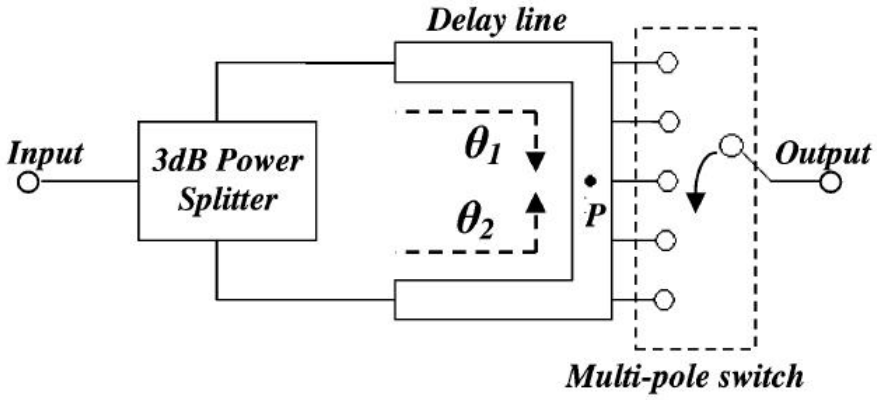

Figure 2.15: Switched delay-line resonator. After Wong and Hunter [7].

2.6.2 Switched-Delay Line Tunable Filters

A switched-delay line resonator is shown in Figure 2.15 [7]. A 3-dB power splitter is used to split the input signal into two parallel delay lines the output of which is combined by a multi-pole RF switch. The phase difference between the two parallel delay paths are responsible for the transmission response of the switched delay-line resonator. The path delays allow the signals in the two-paths to constructively interfere to create the passband and destructively interfere to create the stop-band. Two such resonators can be cascaded together in such a way that the length of delay line for the second resonator is doubled (compared to that of the first resonator) to produce a quasi-elliptic filter response with a transmission zero on either sides of the passband. However, the passband-bandwidth is not suited for narrow filter bandwidth and the stop-band rejection is not very high. In order to provide a better bandwidth control and higher stopband rejection a unit element (U.E) such as a quarter wavelength line is introduced as shown in Figure 2.16a. The U.E element determines the pass bandwidth and stop-band rejection without affecting the location of the transmission zeroes and poles as shown in Figure 2.16b. A switched-delay line filter in which a parallel coupled line is used as an U.E with frequency and bandwidth control for narrowband applications is discussed in [53].

One of the big advantages of these filters is that the switching element is part of the cou-

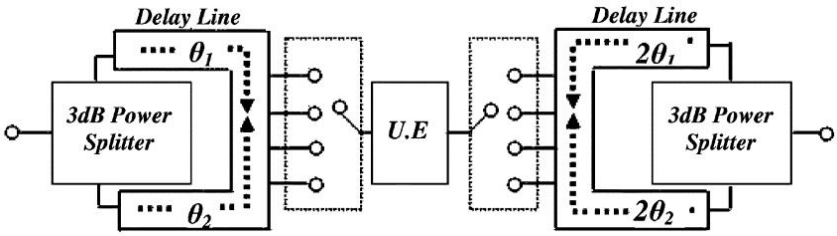

(a)

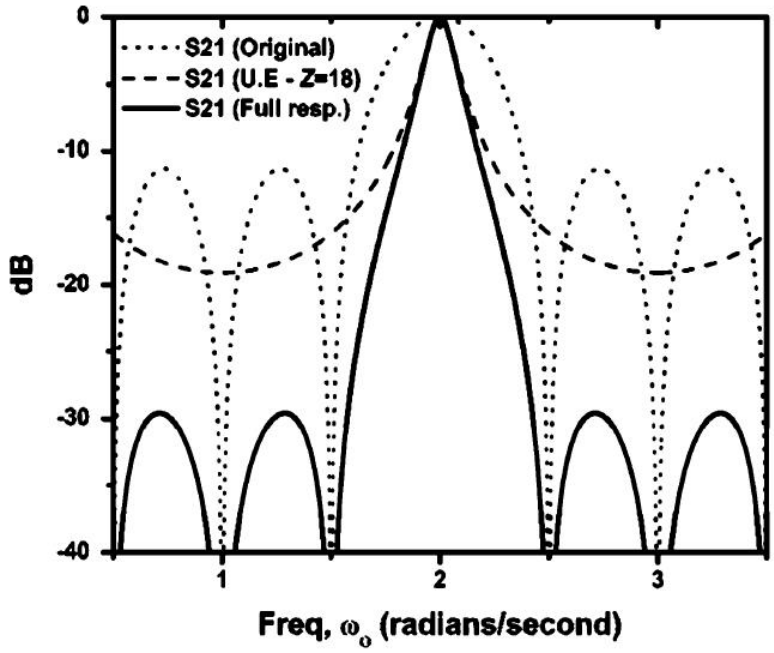

(b)

Figure 2.16: Two cascaded switched delay-line resonators with a unit element and its transmission response. After Wong and Hunter [7]: (a) topology of two cascaded switched delay-line resonators with a unit element; and (b) transmission response (S_{21} dB of the two-pole filter).

pling circuit and not part of the resonator. Hence, the non-linearity and losses associated with the switching element do not affect the filter insertion loss and linearity. The mid-band filter insertion loss remains unaffected by the filter-bandwidth in this topology which is not the case in transmission-line resonator based topologies where a narrow-band filter has higher insertion loss.

2.6.3 Discussion

The two filter topologies discussed in this section suggest other ways in which filters could be designed with higher unloaded Q without following the popular transmission-line resonator based design approach. The waveguide mode with the very high unloaded Q of the evanescent waveguide (as opposed to the transmission line) could provide higher overall Q and thus lower insertion loss. Another method of designing a high-performance filter would be to design switches in switched-delay line tunable filters using the desired enabling technology.

The next section discusses the performance of different ferroelectric-based tunable filter designs as ferroelectric is the chosen enabling technology for this research work.

2.7 Ferroelectric-Based Tunable Filter Design

The relative dielectric constant of ferroelectric films can be electronically tuned by the application of DC bias voltage which makes them very attractive for tunable filter applications. Thin films of barium strontium titanate (BST) or strontium titanate (STO) are typically used as tunable materials in ferroelectric filters. Depending on the curie temperature of the fabricated ferroelectric film, some of the filters operate at room temperature (RT) while others operate at a much lower temperature. Some of these filters use high-temperature superconductors (HTS) such as yttrium barium copper oxide (YBCO), in place of copper (Cu), silver (Ag) or gold (Au) metallization to reduce the conductive losses of the filter [4, 16, 17]. Filters operating at temperatures lower than room temperature require additional packaging as they must be enclosed in a box to cool them to the required cryogenic temperature of operation. Cryocoolers reduce

the filter portability and increase power consumption. The performance of some ferroelectric filters in recent published work is cited and discussed below.

Subramanyam *et al.* [4] demonstrated a HTS/STO-based two-pole coupled microstrip tunable ferroelectric bandpass filter operating at temperatures of ≤ 77 K. Low tuning (9.77%) and an insertion loss variation of 5 to 2.2 dB was reported. The bandwidth varied by 0.3 GHz within the tuning range. To reduce insertion loss and unintentional tuning of a HTS/ferroelectric filter, the ferroelectric layer was patterned in [16]. A tuning of 1.62% and an insertion loss variation of 1.6 to 0.35 dB was reported. Bandwidth variation of 0.03 GHz was observed. Three-pole interdigitated capacitor (IDC) based ferroelectric filters operating at 77 K was reported by Su *et al.* [17]. YBCO/BST was used as the metal/dielectric bi-layer. Each of the resonators of the filters was individually biased to optimize the return loss. The range of insertion loss reported for the YBCO/BST filter was 6 to 1.4 dB with a bandwidth variation of 0.05 GHz for a maximum tuning of 5.14%. A two-pole ferroelectric filter operating at room temperature was fabricated by Courrèges *et al.* [21]. Several BST capacitors were individually biased to achieve frequency tunability with a constant bandwidth and return loss. A frequency tuning of 7.37% with an insertion loss in the range of 2.75 to 2.2 dB and a maximum bandwidth variation of 0.06 GHz was reported. Two three-pole combline BST based bandpass filter were reported by Sigman *et al.* [18] that operated at zero-bias center frequency of 8.75 GHz and 11.7 GHz, and maximum bandwidths of 1.8 GHz and 1.7 GHz respectively. One of the measured filters had a tuning of 25.26%, insertion loss between 8 and 4 dB and a maximum bandwidth variation of 0.2 GHz within the tuning range at room temperature. The other filter had a tuning of 22.22%, insertion loss variation between 6 and 10 dB and a bandwidth variation of 0.1 GHz in the tuning range. The performance parameters of these filters are tabulated and compared in Chapter 5.

Very few published tunable ferroelectric microwave filter designs report high tunability ($\geq 20\%$). The tunability is not adequate to provide a feasible alternative to switchable filter banks. Chapter 5 of this thesis discusses details of a ferroelectric filter designed with high frequency tunability (36.5%). The filter is also designed to have a constant bandwidth with a

tolerance of ± 75 MHz. This ensures that the filter bandwidth for this high tunability filter remains below the acceptable system ADC analog-bandwidth.

2.8 Performance of Filters With Different Topologies

Table 2.1 summarizes the performance of filters with the different topologies using different enabling technologies discussed in this chapter. It can be seen that the ferroelectric filters have higher insertion loss especially if the tunability is high ($\geq 20\%$).

Ferroelectric filters have been known to have high insertion loss (irrespective of topology) but isolating the source of loss in these filters has been a formidable task to accomplish. Recent advancements in EM simulation tools and the computing power of newer computers have opened up an opportunity to make this exploration possible. Chapter 6 of this thesis aims to explore the reasons behind this high insertion loss associated with ferroelectric filters using EM simulations to design lower loss ferroelectric filters in the future without compromising other performance parameters such as tunability and bandwidth.

Table 2.1: Performance of Filters With Different Topologies Discussed In This Chapter (FBAR = Film Bulk Acoustic Resonator, MEMS = Micro Electro-Mechanical Switches, MIM = Metal Insulator Metal).

Reference	How is wide tuning bandwidth achieved?	Filter Topology	Center Frequency Tuning Element/ Material	Filter Performance		
				Insertion Loss (dB)	Bandwidth (GHz)	Frequency Range (GHz)
Packiaraj *et al.* [35]	Multiple fixed frequency filters	Fixed frequency filters with external switches (Section 2.3.1)	switches (controlled by driver and switching network)	4	0.25	1.5-2.15
Zhu *et al.* [2]	Multiple fixed frequency filters	Fixed frequency filters with FBAR topology (Section 2.3.2)	ferroelectric material	6.2	0.04	around 2.14 GHz
Carter [39]	Tunable filter	Magnetic resonance filter (Section 2.3.3)	Yttrium-Iron-Garnet (magnetic switch)	2	0.028	7.0-11.0
Hunter and Rhodes [25]	Tunable filter	Combline (Section 2.5.1)	semiconductor varactor	5.4	0.2	3.2-4.9
Nordquist *et al.* [54]	Tunable filter	Combline (Section 2.5.1)	RF MEMS switches and MIM capacitors	6.0	1.3	8.2-11.3
Brown and Rebeiz [3]	Tunable filter	Inter-digital (Section 2.5.2)	semiconductor varactor	5.8	0.188	0.7-1.33
Subramanyam *et al.* [4]	Tunable filter	Edge-Coupled (Section 2.5.3)	ferroelectric material	5	1.5	17.4-19.1
Matthaei [5]	Tunable filter	Zig-zag hairpin-comb (Section 2.5.4)	interdigital capacitors	1.2	0.017	0.498-0.948
Joshi *et al.* [6]	Tunable filter	Evanescent Mode (Section 2.6.1)	piezoelectric actuator based varactor	2.4	0.09	2.71-4.03
Wong and Hunter [7]	Tunable filter	Switched-delay line (Section 2.6.2)	diode switches	< 4	0.05	1-1.6 [60%]
Sigman *et al.* [18]	Tunable filter	Combline (Section 2.5.1)	ferroelectric material	8	1.8	8.75-10.96
Sigman *et al.* [18]	Tunable filter	Combline (Section 2.5.1)	ferroelectric material	10	1.7	11.7-14.3

2.9 Conclusion

This chapter provides relevant background information to set the stage for the succeeding chapters in the dissertation. The performance parameters and some terminologies commonly used in the RF front-end filter designs were presented. While fixed-frequency filters with external switches are used currently to support the demand for broad-band transceivers, other topologies like FBAR filters and tunable filters were discussed. Tunable filter topologies have emerged as one of the favored research paths to design future multi-mode, multi-functional hand-held devices. Tunable filter topologies use different enabling technologies such as MEMs, semiconductor varactors and ferroelectric materials. Using each of these technologies to design tunable filters however has its set of challenges. Different transmission-line resonator based tunable filter topologies such as combline, inter-digital, edge-coupled and hairpin-comb were discussed and elaborated by way of examples. The topology chosen can have an influence on the filter response characteristics. As an example, the combline filter topology has an asymmetrical filter response and wide stop band. The tunable ferroelectric three-pole design discussed in Chapter 4 is a combline-filter. Other tunable filter topologies that are not transmission-line resonator based such as the evanescent mode and switched-delay line topologies were also presented. These alternate topologies could reduce the insertion loss in future ferroelectric tunable filter designs. The topic of this dissertation involves ferroelectric varactor based tunable filter design. A brief introduction to ferroelectric as an enabling technology was provided in this chapter; the next chapter (Chapter 3) provides a more detailed review of ferroelectric varactors.

Chapter 3

Ferroelectric Varactors in Tunable Microwave Filters

3.1 Introduction

Ferroelectric materials are considered an enabling technology to design frequency-agile microwave filters. These materials have a strong non-linear field dependent permittivity that enables material tunability to be translated into frequency tunability. In this chapter, ferroelectric varactors that are integrated into tunable resonators to design microwave filters are discussed.

3.2 Ferroelectricity

In some non-conducting or dielectric materials, the constituent atoms are ionized such that the centers of positive and negative charges may not coincide even in the absence of an electric field. Such materials are said to exhibit spontaneous polarization. If the spontaneous polarization of a dielectric can be reversed by an electric field, they exhibit ferroelectricity. Contrary to the meaning of the suffix "ferro" in ferroelectric materials, most of these materials do not contain any iron. The term ferroelectricity was coined because of its analogy to ferromagnetism. Ferromagnetic materials like iron, spontaneously align themselves in small clusters called ferro-

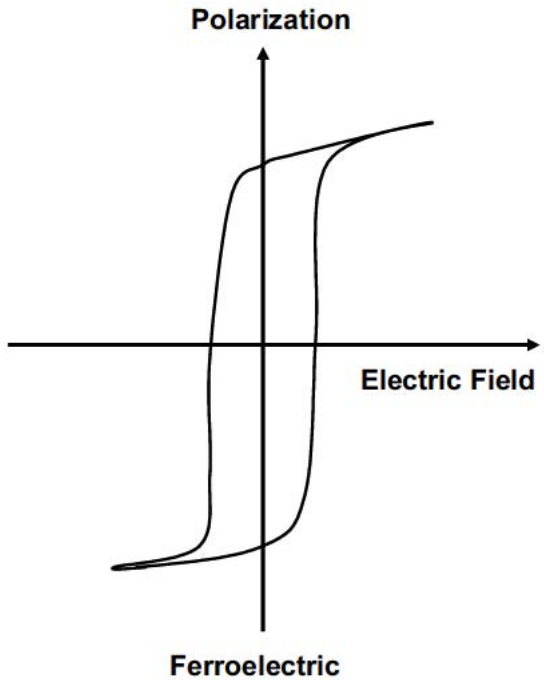

Figure 3.1: Polarization plotted as a function of electric field. Ferroelectric hysteresis effect is observed. After Nath [8].

magnetic domains. The net magnetic moment can be reversed by the application of a magnetic field [55].

Ferroelectric materials, like barium strontium titanate, strontium titanate and barium titanate are made up of tiny ionized-crystals. In a particular temperature range the positive and negative ions are displaced and they form tiny electric dipoles. In some crystals, these dipoles align themselves in clusters exhibiting a net electric dipole moment. In ferrolectric crystals these domains can be oriented in one direction by the application of an external electric field. Reversing the electric field causes the electric polarization to lag behind the applied external electric field — a phenomenon called ferroelectric hysteresis reminiscent of magnetic hysteresis as shown in Figure 3.1.

The property of ferroelectric materials are highly temperature dependent and in general an abrupt phase transition takes place above a temperature called the curie temperature (T_c) as

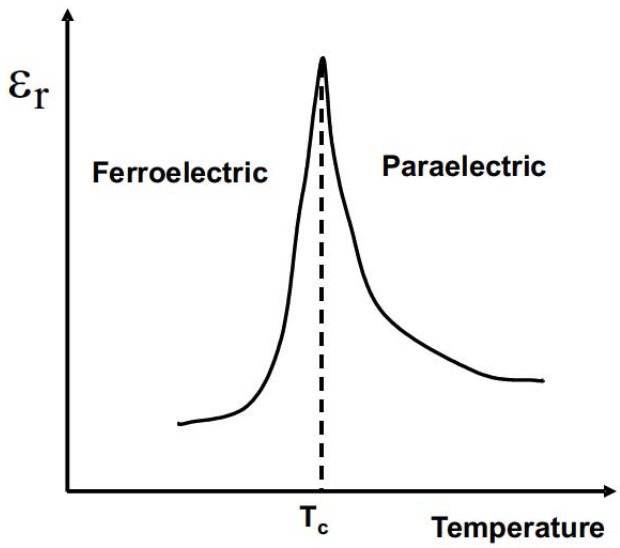

Figure 3.2: Dielectric permittivity as a function of temperature. T_c is the curie temperature. Below curie temperature the material is said to be in a ferroelectric phase while above the curie temperature the material is said to be in a paraelectric phase. After Nath [8].

shown in Figure 3.2. Ferroelectric materials are said to be in the paraelectric phase above the curie temperature which is characterized by the absence of domain walls and hysteresis. Ferroelectric phase is suited for applications like non-volatile memories where spontaneous polarization is used to store information in bits while paraelectric phase is typically used in applications that require lower losses like microwave devices. Figure 3.3 is a plot of polarization as a function of electric field for a ferroelectric material in the paraelectric phase. It must be noted that no hysteresis effect is observed in this plot. Although ferroelectric materials exhibit different phases, those used in the paraelectric phase are still referred to as ferroelectric materials.

There are a couple of interesting characteristics that warrant tailoring the curie temperature. The dielectric constant is the highest close to the curie temperature and the sensitivity of the dielectric constant to the applied electric field is the highest at this temperature as well. The curie temperature is changed by varying the doping ratio of the composite ferroelectric material. For example in barium strontium titanate (BST or $Ba_xSr_{1-x}TiO_3$ where x can take a value between 0 and 1), the value of x (doping ratio) is varied to change the phase transition

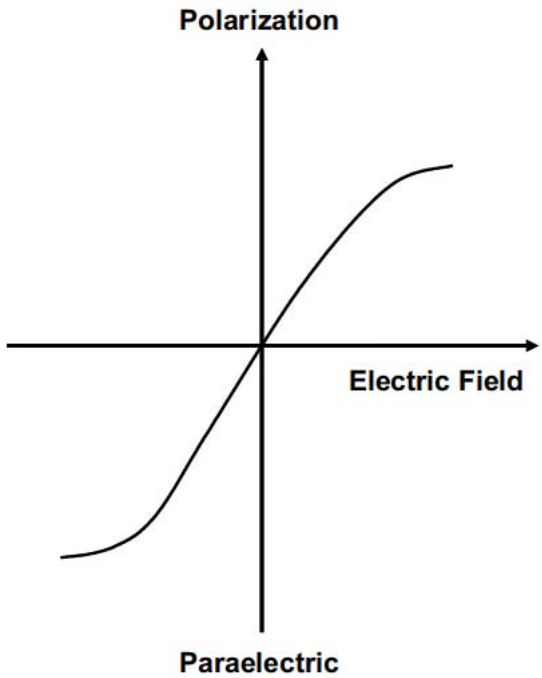

Figure 3.3: Polarization plotted as a function of electric field. The material is in a paraelectric phase and hence no hysteresis effect is observed. After Nath [8]

curie temperature. The value of x is typically close to 0.5 for room temperature applications and 0.1 if the material is used with high-temperature superconductors (HTS) [46]. The high-permittivity of BST films (300–1000), their low loss tangents (0.013–0.023), the ability to use them at room-temperature, and their large voltage dependent permittivity make them attractive among the ferroelectric materials for designing tunable microwave circuits. In this research work, paraelectric phase of barium strontium titanate at room temperature is used.

Ferroelectric materials can be used as thick-film (> 1.0 μm) or thin-film (< 1.0 μm). Filters and matching networks that use thick-film technology to deposit ferroelectric materials usually have lower tuning ranges when compared with those using thin-film ferroelectric materials. In addition, high frequency dispersion and low Q-factors are observed in devices using thick-film ferroelectric materials. Thin-films show a non-dispersive behavior upto 40 GHz. BST thin-films have higher tunability and require low tuning voltages (10-200 V) compared to their thick-film

counterparts. The lower tunability and higher tuning voltage can be attributed to the fact that only a thin-upper layer of the BST thick-film is tunable. This creates a parallel equivalent non-tunable parasitic capacitance with the top-layer tunable capacitance.

3.3 Ferroelectric Varactors - Metal-Insulator-Metal and Planar Capacitors

Ferroelectric varactors are used as tuning elements in frequency agile devices and allow a considerably smaller device footprints owing to their high-dielectric constant. They can be fabricated as Metal-Insulator-Metal (MIM) capacitors and interdigitated capacitors (IDC). The layout of MIM and IDC capacitors are shown in Figures 3.4 and 3.5 respectively. MIM capacitors have a bottom and top electrode with a dielectric sandwiched between them. Hence they are also called parallel-plate capacitors. IDC capacitors are planar or surface capacitors with a dielectric under the electrodes that are separated by a gap width.

MIM capacitors have a high capacitance density (10–40 fF/μm^2 range) and require low tuning voltages (10–30 V) [8]. They however have low power handling capability, poor linearity and require multiple-lithography steps compared to IDC capacitors. IDC capacitors have high power handling capability, better linearity, require only a single layer lithography. IDC capacitors however require high tuning voltages (75–100 V) and have low capacitance density compared to MIM capacitors. The use of MIM versus IDC capacitors for a particular application depends on system requirements such as ease of fabrication, linearity requirement, availability of tuning voltage sources and device portability.

In this work, planar IDC and gap capacitors are considered over MIM capacitors because of lithography challenges and the topology of the microwave filters chosen. The lithography patterning and alignment of the three-layered MIM structure was considered to be more challenging compared to the single layer lithography required for planar capacitors [9]. Furthermore, the filter topology used has multiple resonators each with its own ferroelectric capacitor. MIM based

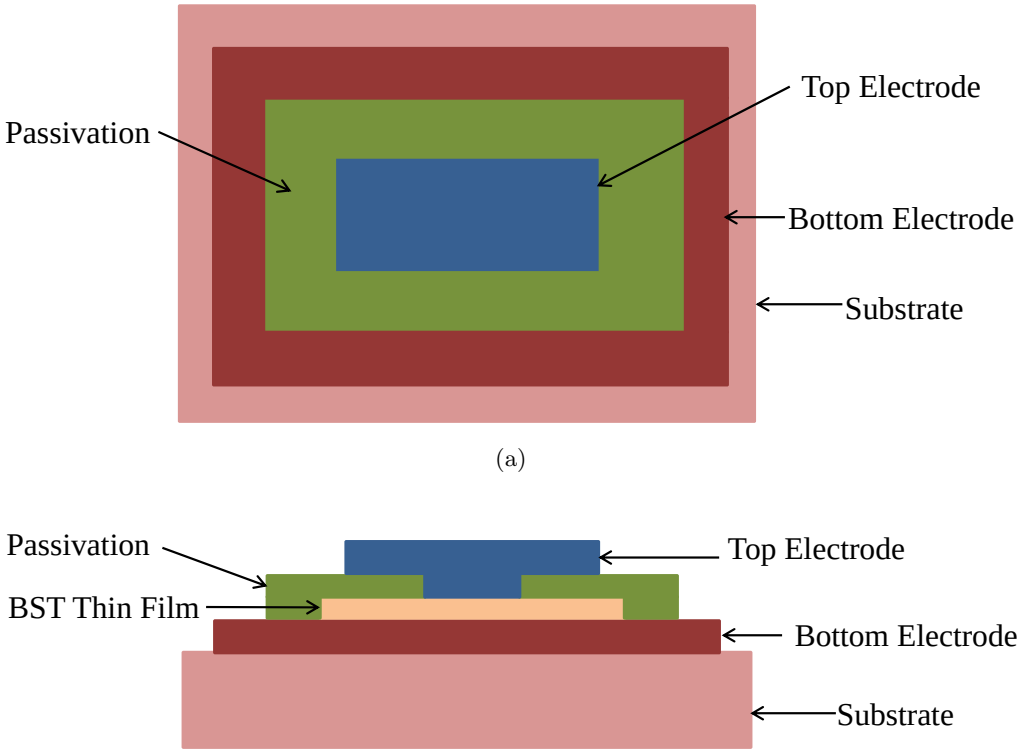

Figure 3.4: Metal-Insulator-Metal (MIM) capacitors: (a) top-view; and (b) side-view.

fabrication of multiple capacitors for the different resonators on the same filter can produce substantial variation in capacitance values. These capacitor value variations in the different resonators making up a filter could result in an increase in filter loss. Surface or planar capacitor are thus preferred.

3.4 Planar Capacitors — IDC and Gap Capacitors

As shown in Figure 3.5a, IDC capacitors have two electrodes with a lot of fingers. The gap lengths and gap widths are highlighted in the figure. The total capacitance is approximately the parallel combination of the individual gap capacitances across the fingers. Thus, increasing the number of fingers increases the total IDC capacitance. The gap width between the fingers

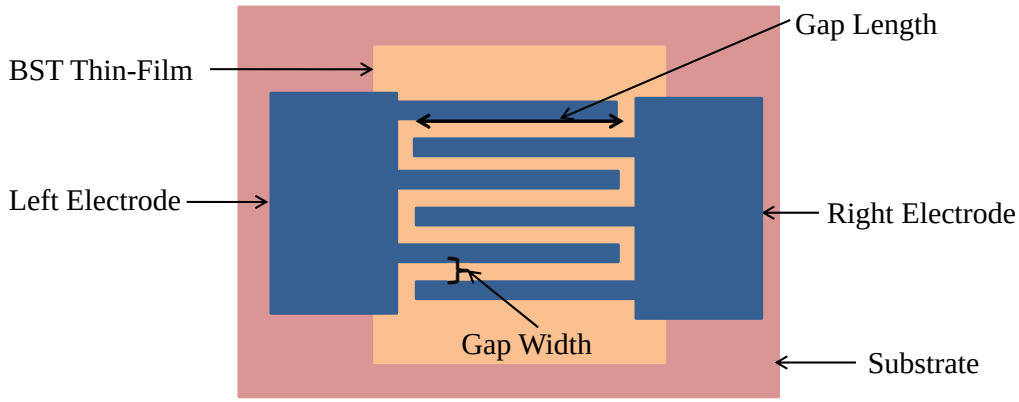

(a)

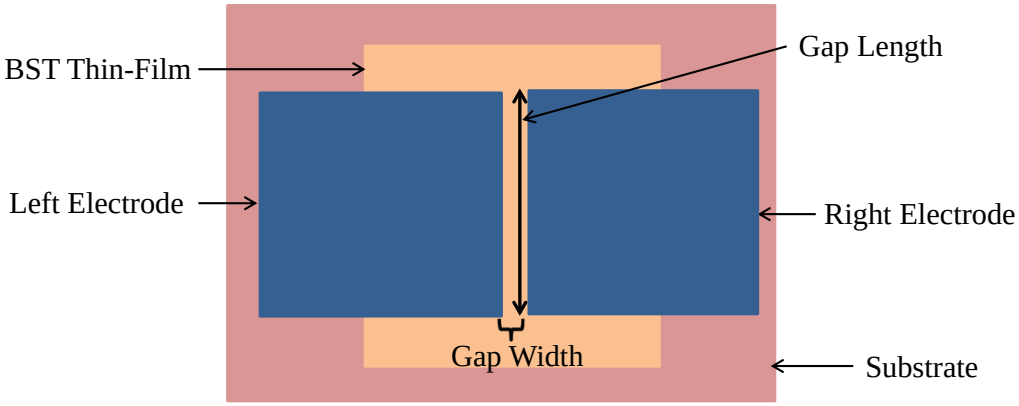

(b)

Figure 3.5: Planar capacitors (or surface capacitors): (a) IDC capacitor top-view; and (b) gap capacitor top-view.

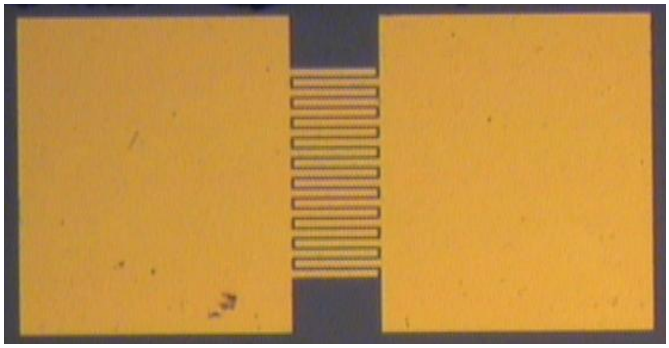

(a)

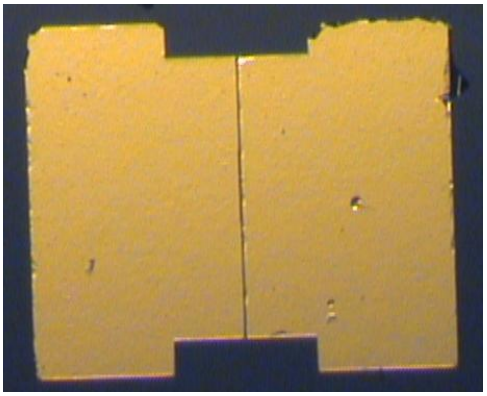

(b)

Figure 3.6: Top-view of fabricated planar capacitors showing the metal pattern: (a) IDC capacitor; and (b) gap capacitor.

can be adjusted to change the capacitance value although it also determines the sensitivity of the capacitor to the tuning voltage. To reduce the capacitance value it is therefore preferable to reduce the number of fingers or the gap lengths rather than the gap width.

The gap capacitor is a simpler subset of an IDC capacitor wherein the finger electrodes are replaced by two single electrodes separated by a gap as show in Figure 3.5b.

3.4.1 Device Characterization

BST-based IDC and gap capacitors are integrated with microstrip lines to form tunable resonators. Multiple resonators are coupled together in different filter topologies to create microwave filters as will be discussed in later chapters. Although these planar capacitors are used

in microwave filters that operate at high frequencies of 3–18 GHz, they are typically characterized at lower frequencies (1–100 MHz). Conductor losses and other parasitic effects become more pronounced at higher frequencies (> 100 MHz) which make it more difficult to characterize the tunable BST material.

Mulitple stand-alone IDC and gap capacitors as well as those integrated with tunable resonators in a filter topology are fabricated (using the same processing steps) and characterized. Figure 3.6 is an example of a fabricated stand-alone IDC and gap capacitor. The metal electrodes shown in Figure 3.6 is patterned on top of the alumina-BST (thin-film) composite substrate.

Tunability of the BST material is defined as:

$$\%T_{\mathrm{BST}}(V) = \frac{(\epsilon(0) - \epsilon(V))}{\epsilon(0)} \times 100 \tag{3.1}$$

where V is the voltage, $\epsilon(0)$ and $\epsilon(V)$ are the dielectric permittivites at 0 V and V V respectively [32]. It is easier to measure capacitance than the dielectric permittivity of the material. Hence, material tunability is characterized by measuring the tunability of a capacitor using BST as a dielectric material. Capacitance tunability can be expressed in percentage assuming a fixed voltage range. Tunability of a capacitor expressed in percentage is then defined as:

$$\%T_c = (\frac{C(0) - C(V)}{C(0)}) \times 100 \tag{3.2}$$

where $C(0)$ and $C(V)$ are the capacitances measured at voltages 0 V and V V.

The tunability of the capacitor and the loss tangents were measured using HP4192A impedance analyzer at 1 MHz between −35 V to +35 V applied DC bias. Figures 3.7 is a plot of capacitance (C-V graph) and loss tangent as a function of DC bias voltage for an IDC capacitor. The loss tangent data is used to measure the Q-factor of the capacitor as $Q_{\mathrm{cap}} = 1/(\tan\delta)$. Sometimes Q-factor is directly plotted inplace of $\tan\delta$. Figure 3.8 shows the C-V graph and the Q-factor graph for a gap capacitor.

These capacitors have very low level leakage current (in the pA range) as shown in Figure 3.9.

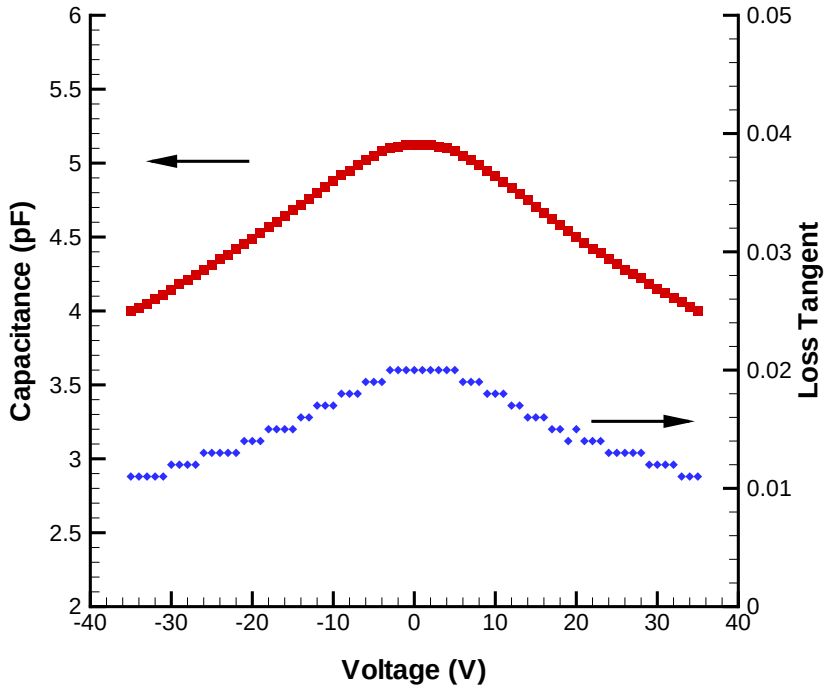

Figure 3.7: Capacitance and loss tangent as a function of bias voltage for an IDC capacitor.

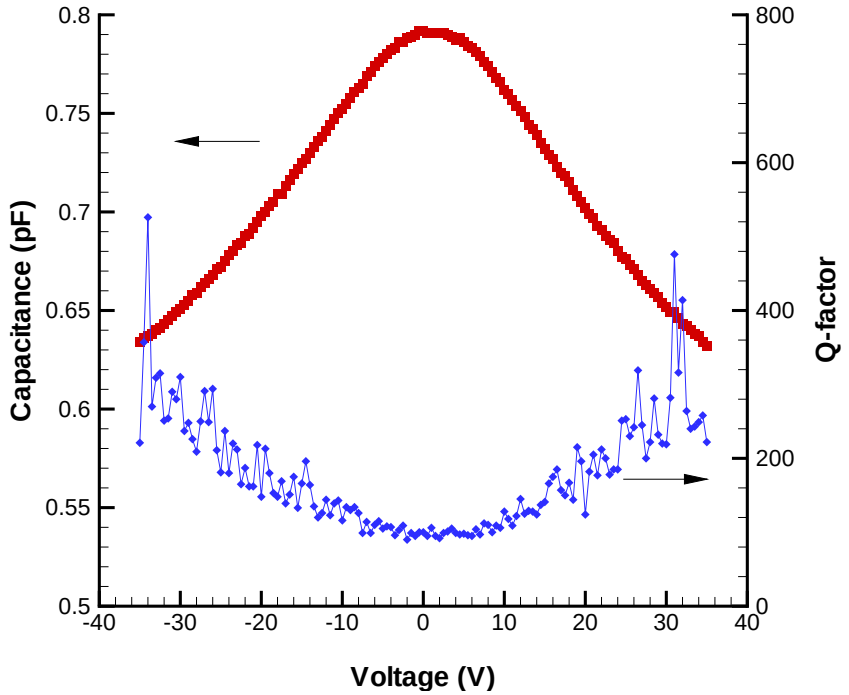

Figure 3.8: Capacitance and Q-factor as a function of bias voltage for a gap capacitor.

The leakage current was measured using Keithley 617 electrometer for a gap capacitor with a gap-width of 3 μ m. Ten measurements per voltage with a two second wait between each voltage step increase was used to measure the leakage current. Measurements were taken in increments of 0.5 V.

3.4.2 Series Capacitor Configuration in Fabricated Filters

In a tunable filter, the capacitance value of gap or IDC capacitors are varied by applying a DC bias voltage to change the dielectric permittivity of the underlying BST thin-film. In other words, these capacitors are used as varactors to tune the filter. In the fabricated filter, each tunable resonator has two IDC (or gap) capacitors connected in series to allow for DC bias as shown in Figure 3.10.

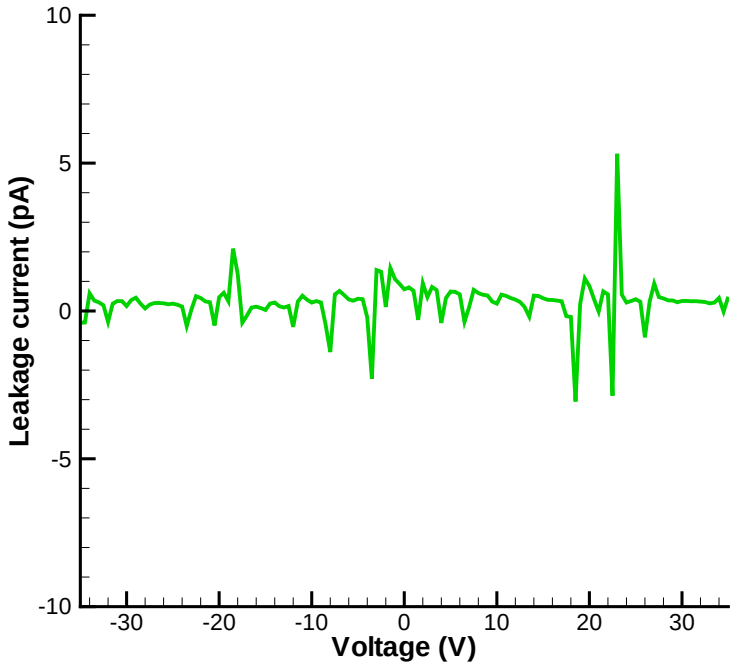

Figure 3.9: Leakage current in pA as a function of bias voltage.

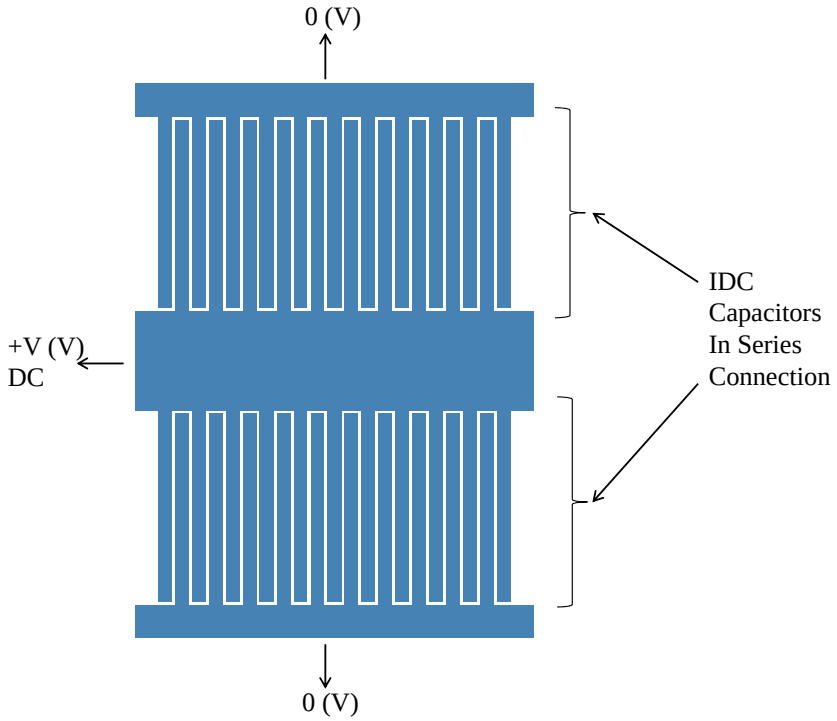

(a)

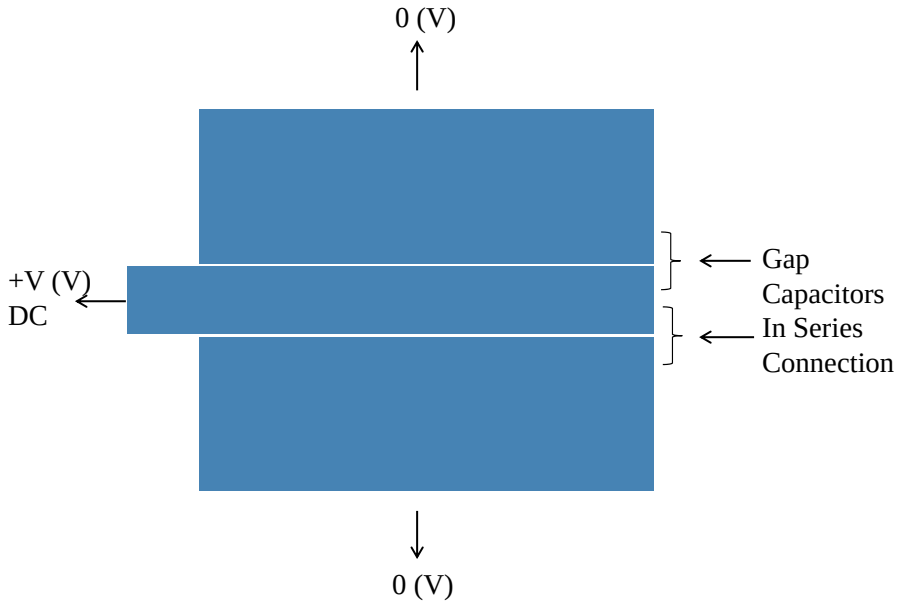

(b)

Figure 3.10: In a practical filter circuit, each tunable resonator has two IDC or gap capacitors connected in series configuration to allow for DC biasing: (a) IDC capacitors in series configuration; and (b) gap capacitors in series configuration.

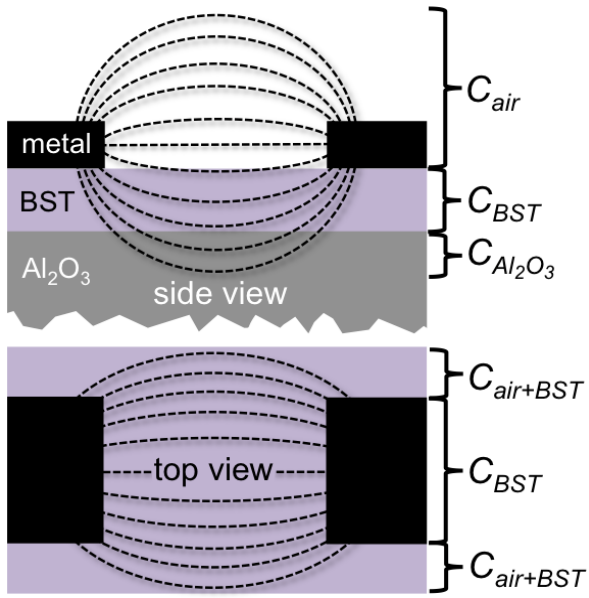

Figure 3.11: Electric field distribution in a gap capacitor. The field is distributed across air, BST and the alumina substrate. After Lam *et al.* [9].

3.5 Electromagnetic Modeling of Surface Capacitor

To study the parasitic effects of planar (or surface) capacitors, electromagnetic (EM) modeling and simulations of the capacitor layout was performed. For easier understanding a simpler gap capacitor structure is simulated. The next section briefly discusses the electric field distribution in a gap capacitor before addressing the simulation details and the results.

3.5.1 Electric Field Distribution In A Surface Capacitor

Figure 3.11 shows the side and top views of the gap capacitor. The two electrodes are separated by micron range gap widths. The field is not confined and is distributed as shown in Figure 3.11 between the BST dielectric, alumina substrate and air or low-permittivity dielectric used as a passivation layer. The parallel components of the capacitances are highlighted in Figure 3.11. It must be noted that C_{air} and $C_{\text{Al}_2\text{O}_3}$ are non-tunable parasitic capacitances whereas C_{BST} is the tunable capacitance. Non-tunable parasitic capacitors also appear in parallel across tunable

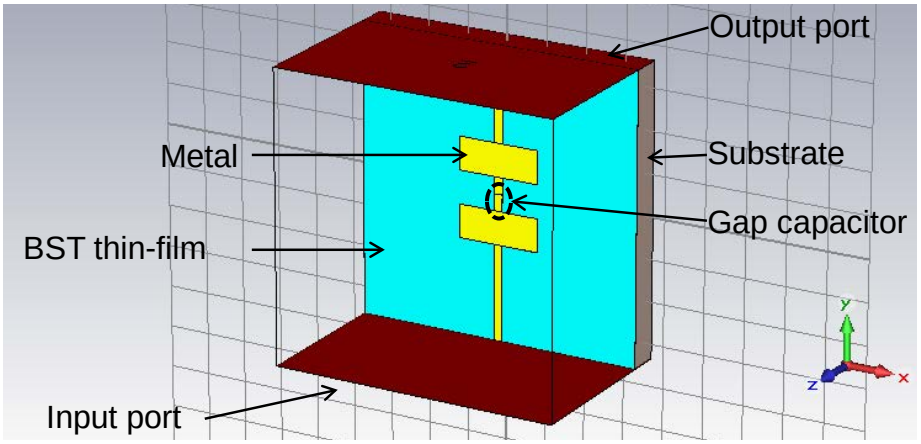

Figure 3.12: Capacitor layout simulated in CST Microwave Studio. A 381 μm thick alumina substrate, 0.5 μm thick barium strontium titanate (BST) layer and 0.35 μm thick metal trace are depicted in the layout. Two waveguide simulator ports are attached to the input and output metal traces.

IDC capacitors. Hence, larger external bias voltages are required to tune a surface capacitor compared to the bias voltages required by the MIM capacitors that do not have these associated parasitic capacitors.

3.5.2 Gap capacitor EM model

The simulations were performed using Computer Simulation Technology's (CST) Microwave Studio Suite [56], a 3-D electromagnetic simulation solver. The layout of the simulated capacitor with a gap width of 3 μm is shown in Figure 3.12. The dielectric stack is represented in the simulator as 381 μm alumina substrate with a BST thin-film of 0.5 μm thickness on top of it. A simple metal layout pattern with two electrodes separated by a gap-width and a thickness of 0.35 μm represents the gap capacitor. Parametric analyses of the capacitor for different gap lengths were performed using a frequency-domain solver to extrapolate the zero-length capacitance (or length-independent fringe capacitance). Simulations could not be performed at 10 MHz because the increased meshing required (to ensure accuracy of results) at low frequencies caused a drastic increase in memory and simulation time. A slightly higher simulation frequency of 100 MHz is

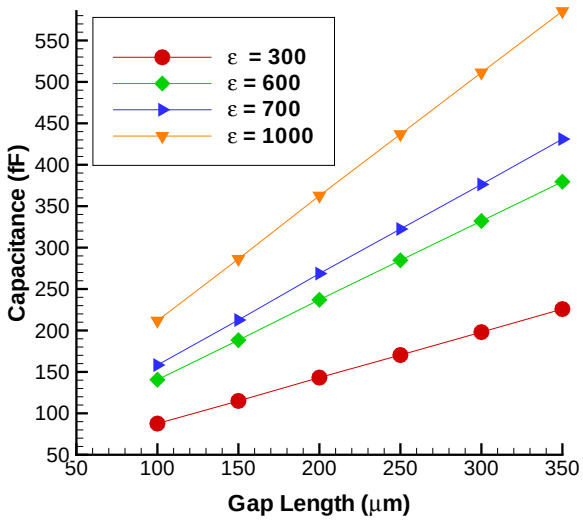

Figure 3.13: Simulation of the capacitance versus gap length as a function of the permittivity of barium strontium titanate.

used as a trade-off. Although the simulations were performed at 100 MHz, their results can be compared with the results measured at 10 MHz as differences in capacitance values, if any, at such low frequencies are practically negligible.

3.5.3 Simulation results

The dielectric permittivity of the BST was varied (300, 600, 700, and 1000) and the corresponding fringe capacitances were obtained as shown in Figure 3.13. It is observed that the y-intercepts on the plots in Figure 3.13 indicate that the capacitance at zero-length is not 0 fF. From the plots, fringe capacitances of 32 fF, 45 fF, 49.5 fF and 62.6 fF were obtained for dielectric permittivities of 300, 600, 700 and 1000 respectively. Local and global hexahedral meshes were unchanged while simulating devices with different permittivities to allow comparison of their fringe capacitance values. The fringe capacitance and the slope of the curves exhibit linear dependence with the permittivity value. The fringe capacitance increased as the dielectric permittivity of the BST was increased, suggesting that a lower overall permittivity is preferred for lowering the non-tunable fringe capacitance although a lower permittivity would result in

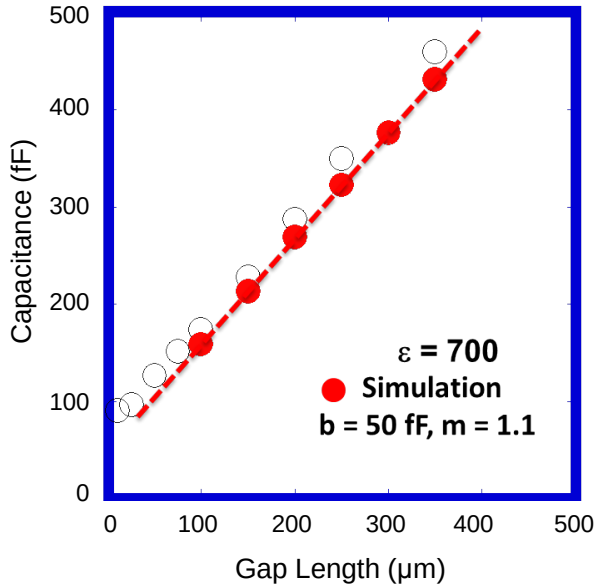

Figure 3.14: Simulation data for capacitance versus gap length for a permittivity of 700 overlaid on the measurement data at low gap length dimensions. After Lam *et al.* [9].

larger device size, and, in most cases, a lower tuning range. It is theorized that the parasitic non-tunable capacitance becomes a significant proportion of the total capacitance as the total capacitance values are reduced to tune filters at higher frequencies. This could contibute to the reduced frequency tuning observed at higher frequency (X-band and above) compared to that achieved at lower frequency. To confirm the existence of fringe capacitance values that limit capacitance tunability and hence frequency tunability at higher frequencies, several capacitors were fabricated and measured.

3.5.4 Discussion

BST material was deposited on ceramic alumina substrate (Coorstek Inc., Golden, CO) by RF magnetron sputtering. A stoichiometric $Ba_{0.7}Sr_{0.3}TiO_3$ target was used as the source material. The BST was patterned using photolithography and etched off with a 1% HF solution. Removing the BST layer from all regions except the immediate vicinity of the gap capacitors is important for minimizing insertion loss in a fully processed filter. Subsequently, the substrate was annealed

in air at 900°C for 20 hours to fully densify and crystallize the dielectric. Additional fabrication details can be found in [9]. Several interdigitated simple gap capacitors were prepared using one lithographic step with pattern formation by lift-off. Gap capacitors with gap widths in the 2–5 μm range and gap lengths in the 10–4000 μm range were fabricated. Three gap capacitors of the same physical gap width and length were fabricated on a single substrate and three such substrates were fabricated. A comparison of the simulation and measured results indicate that a permittivity value of 700 displayed the closest line fitting match to the measured data, as shown in Figure 3.14. From extrapolation of the simulation results, it is found that using a simulated permittivity value of 750 gives line fitting that is almost identical to the measured data. Though permittivity is difficult to extract from planar capacitor measurements, preparing BST films under similar conditions in an MIM arrangement yields permittivity values in the range of 700 to 1000, depending on the specific substrate/electrode combinations and thermal budgets. Consequently the fit between modeling and experiment appears self consistent. Fringe capacitances of 50–70 fF were measured which closely agree with the simulated results.

The measured data from the gap capacitors were further used to compute tunability as expressed in Equation (3.2) where V V was set to 35 V. Thus the average tunability computed from nine different capacitors of the same gap length were used to plot the tunability curves shown in Figure 3.15 [9]. While saturation in % capacitance tunability is observed for gap lengths > 1000 μm, a sharp drop in tunability is observed for gap-lengths < 1000 μm (i.e., for capacitances required to design filters in the X-band and beyond). The drop in tunability is observed for all gap-widths. The results also suggest a lower tunability despite no change in the BST dielectric and its underlying material tunability. The field distribution as shown in Figure 3.11 results in parasitic non-tunable capacitive elements in parallel. In the range of 1 pF, these elements become significant in their impact on observable tuning. These results could in part be the reason behind the reduced frequency tunability observed in tunable filters operating at X-band and beyond compared to those that operate in the low-GHz range. These results also suggest that the tunability (both capacitor tunability and corresponding frequency

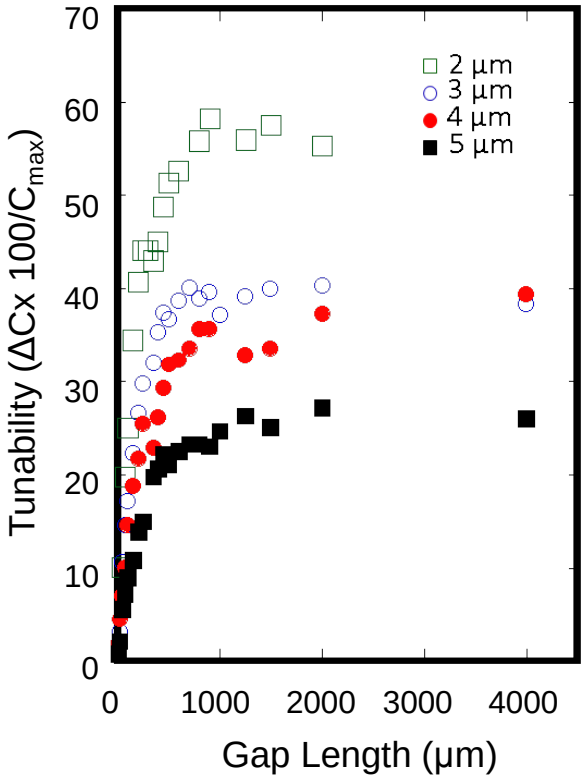

Figure 3.15: Capacitance tunability for gap capacitors as a function of gap length. Data sets for 2 μm, 3 μm, 4 μm, and 5 μm gaps are shown simultaneously. Each data point corresponds to an average calculated from six capacitors. In some cases, data points are missing; this corresponds to sizes for which the complete sets of functional capacitors were not available. After Lam *et al.* [9].

tunability observed in filters) can be improved by figuring out ways to reduce fringe capacitance in surface capacitors.

The simulated and measured results thus confirm the existence of a parasitic non-tunable capacitance that limits the capacitance tunability of the device as the gap length reduces (or total capacitance value required for tunable filter resonance reduces).

3.6 Conclusion

This chapter discussed details of the ferroelectric varactors that are part of the tunable resonators used in this dissertation. These tunable resonators are coupled in various topologies to create microwave filters that are used in this research work. The chapter began with a discussion of ferroelectricity and discussed the different topologies of ferroelectric capacitors. Reasons behind choosing planar IDC or gap capacitors over MIM capacitors for the current work were highlighted. C-V and loss tangent-voltage plot for gap and IDC capacitors that are used in this work are discussed. The field-distribution of a gap capacitor indicates poor field confinement. EM modeling of the gap capacitors suggest the existence of a non-zero capacitance value as the gap length is reduced to a theoretical limit of 0 μm. The results obtained from simulations are compared with measured results. They confirm the existence of a parallel non-tunable fringe-capacitance. Computing % capacitance tunability using the measured data supports the hypothesis based on EM modeling that the capacitance tunability in surface capacitors reduces as the total capacitance value is reduced due to the pronounced effect of fringe capacitance. The reduced capacitance tunability translates to reduced frequency tunability in microwave filters at high frequencies (X-band and above).

Based on the analysis of simulation and measured results, one of the potential ways to increase tunability would be to find alternate capacitor structures and topologies that would reduce the fringe-capacitance. High insertion loss of ferroelectric filters is one of the biggest challenge faced by tunable ferroelectric filter designers. Novel designs that reduce fringe-capacitance can be used to alleviate some of this problem because of an underlying inverse relation between

frequency tunability and unloaded Q-factor of the resonators (details on this inverse-relation is discussed in Chapter 4). The increased tunability achieved by reducing fringe capacitance could be traded off to increase unloaded Q-factor of the resonators and correspondingly lower filter insertion loss, thereby enhancing overall system performance.

Chapter 4

System-Aware Tunable Ferroelectric Microwave Bandpass Filter Design

4.1 Introduction

While a system-aware design of a sub-module, such as a filter, is fundamentally limited by system-constraints, certain system architectures can also relax some filter-specifications. In other words, the performance of a stand-alone filter that would not be at par when compared with other stand-alone filters could be well-suited for a particular system architecture and(or) design. From this standpoint, using a system-aware (as opposed to the traditional stand-alone) figure of merit and design guideline optimizes the filter for the specific application.

Tunable bandpass filters are critical components in emerging radio frequency (RF) front-ends. In this chapter a system-aware design guideline and figure of merit are developed for optimum system-level performance of the tunable ferroelectric filter. A newer RF front-end architecture that can better support high-loss filters such as tunable ferroelectric filters is also discussed.

In emerging emergency and military radios it is often necessary to look at quite wide spectra, the instantaneous bandwidth being constrained by the available performance of high bit-count

ADCs. This type of system is the focus of the current work. Currently this architecture must be implemented using a large number of channels each with its own dedicated RF front-end and ADC. Tunable narrowband circuitry circumvents channelization and so reduces the size, weight and power consumption of emergency and military radios.

Microelectromechanical (MEMS) systems, varactor diodes, and tunable capacitors using ferroelectric films such as barium strontium titanate (BST) are technologies that can enable tunable RF front-end circuits. The adoption of MEMS is hampered by its slow response time and long term reliability concerns however. Varactor diodes have low quality factor (Q) values at microwave frequencies resulting in poor filter performance [45]. BST-based filter designs typically have higher insertion loss (IL) than MEMS-based designs. However, being solid-state devices, they have predictable reliability, have no special packaging requirements, and exhibit a reasonably high Q at RF and microwave frequencies [45].

In RF systems, the network blocks before the ADC significantly influence the system performance as much of the signal processing is performed by filters in the analog domain. Traditionally a tunable bandpass filter is designed to maintain a constant bandwidth across the tuning range. Various design guidelines have been developed to support this [24, 25, 26]. However, this in fact is often not the system-level objective, particularly if this procedure increases insertion loss. A better system-aware objective is that the maximum bandwidth of the tunable filter not exceed the bandwidth of the ADC. In this chapter, a new guideline for the design of a tunable bandpass filter (BPF) is developed using this system-level objective. A system-aware figure of merit is developed that uses worst case filter design parameters and a tuning sensitivity term that captures the frequency tunability relative to material tunability. A 6.74 GHz to 8.23 GHz tunable barium strontium titanate-based filter is presented as an example to illustrate the design methodology.

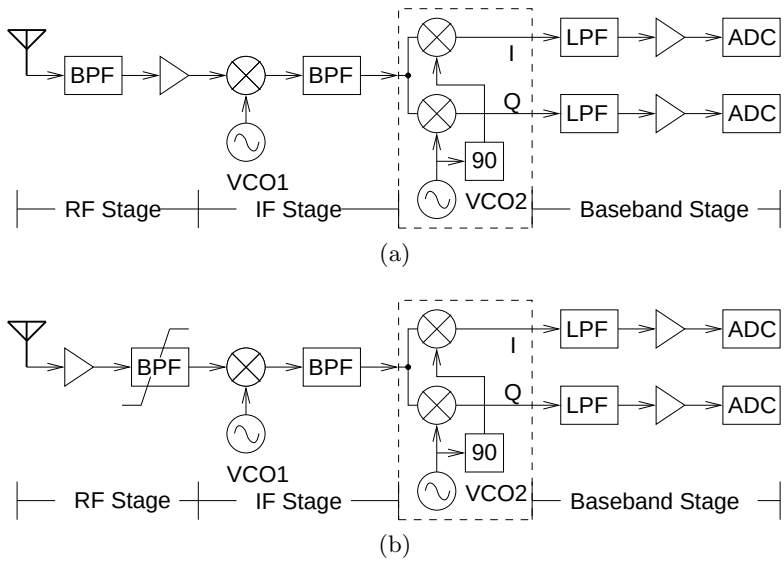

Figure 4.1: Architecture of superheterodyne receivers: (a) fixed bandpass filter is placed immediately after the antenna; and (b) LNA is placed immediately after the antenna followed by a tunable bandpass filter.

4.2 Bandpass Filters in RF Front-End Sub-systems

4.2.1 RF Front-End Architectures

A traditional RF front-end is a cascade of an antenna, a narrow bandpass filter, an amplifier, mixer and stages that implement in-phase/quadrature (I/Q) demodulation for a receiver, e.g. see Figure 4.1a, or modulation for a transmitter [57]. Multiple bands can be accommodated by switching among a number of filter/amplifier blocks. In such a cascaded configuration the noise from each stage contributes to the total RF front-end noise and is given by Friis's equation:

$$F_{\text{total}} = F_1 + \frac{(F_2 - 1)}{A_1} + \frac{(F_3 - 1)}{A_1 A_2} ... + \frac{(F_n - 1)}{A_1 A_2 ... A_{n-1}} \tag{4.1}$$

where F_{total} represents the total noise factor of the receiver. F_1, F_2, F_3 and F_n are the noise factors of the different front-end stages. A_1, A_2, A_3 and A_n represent the power-gain levels of the different front-end stages. Noise factor of each sub-block is defined as:

$$F = \frac{\mathrm{SNR_{out}}}{\mathrm{SNR_{in}}} \tag{4.2}$$

where F is the noise factor, and $\mathrm{SNR_{out}}$ and $\mathrm{SNR_{in}}$ are the signal to noise ratios at the output and input of the sub-block respectively [58].

A quick look at Equation (4.1) shows that noise factor of the first stage in the RF front-end has a dominant impact on the overall noise performance of the RF front-end. A bandpass filter is the first stage in the traditional receiver architecture, shown in Figure 4.1a, and insertion loss in a bandpass filter contributes to the noise factor. In order to tolerate the relatively high insertion loss of electronically tunable filters, an alternative receiver architecture has gained attention. The newer architecture shown in Figure 4.1b switches the locations of the amplifier and the bandpass filter. In such receivers the antenna is followed by a wideband high-dynamic range amplifier incorporating wide bandgap semiconductors followed by a tunable filter. The maximum bandwidth of the filter is then determined by the available bandwidth of analog-to-digital converters with sufficient dynamic range.

4.2.2 Need for Bandpass Filters in RF Front-Ends

Bandpass filters in receiver front-ends are used for frequency selectivity, managing the dynamic range of signals presented to the analog to digital converters (ADCs), and rejecting the image signal. In the architecture shown in Figure 4.1b, the first (tunable) bandpass filter is also used to ensure that the bandwidth of the filtered analog signal does not exceed the bandwidth of the ADC(s).

4.2.2.1 Frequency Selectivity

The primary purpose of the bandpass filter is to provide channel selectivity, i.e. a pre-determined band of signals that fall in the passband frequency range are allowed to be transmitted with

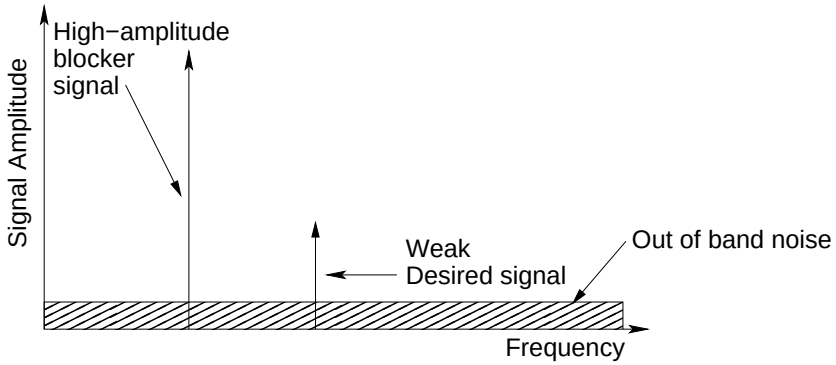

(a)

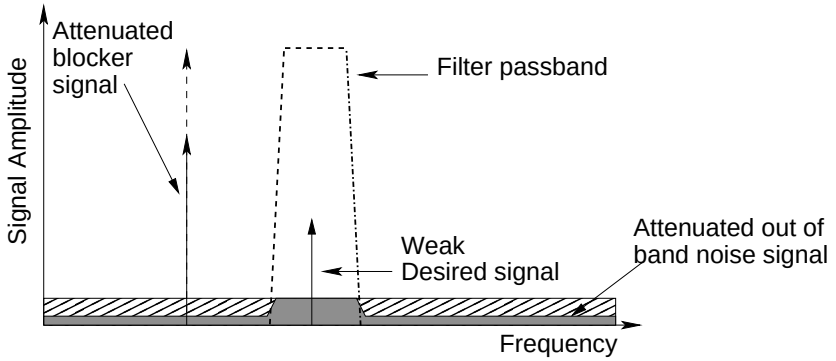

(b)

Figure 4.2: Adding a bandpass filter in front of the ADC attenuates the amplitude of the blocker signal without reducing the amplitude of the weak desired signal: (a) weak desired input signal in the presence of a high-amplitude blocker signal; and (b) adding a bandpass filter in front of the ADC reduces the amplitude of the blocker signal and the out-of-band noise while allowing the weak desired signal to pass-through with minimum attenuation.

minimum attenuation and distortion while the frequencies that fall out-of-band are heavily attenuated thereby blocking out-of-band interferers.

4.2.2.2 Increasing Effective Dynamic Range of ADCs

Dynamic range of an analog to digital converter (ADC) is defined as the range of input signals that can be reliably measured simultaneously, in particular, the ability to accurately measure small signals in the presence of large signals.

In the presence of a large blocker signal, the weak desired input signal to the receiver may

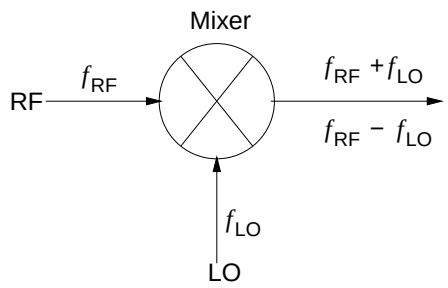

Figure 4.3: An ideal mixer with two input frequencies (f_{RF} and f_{LO}) generates sum and difference frequencies at the output.

get lost as noise. A variable gain amplifier (VGA) usually preceeds the ADC to scale the input signal. The large blocker signal can cause a reduction in the VGA gain to prevent the ADC from getting saturated. This might cause the weak desired signal to be dropped. Placing a narrowband bandpass filter before the ADC can help pull out the weak desired signal in the presence of a blocker signal thereby increasing the effective dynamic range of the ADC. Typically 40 dB of out of band rejection is required to meet system requirements.

Figure 4.2a shows a weak desired signal in the presence of the high-amplitude blocker signal. As shown in Figure 4.2b, the bandpass filter will reduce the strength of the undesired signal and the surrounding noise while allowing the desired input signal to pass-through with minimal attenuation and distortion. The ADC can thus differentiate the weak desired signal from noise when preceeded by a bandpass filter, i.e. the effective dynamic range of the ADC is increased by adding a bandpass filter before it.

4.2.2.3 Image Signal Suppression

Mixers are critical components in RF front-end systems. They down-convert the received RF input signal to an intermediate frequency (IF) for easier and inexpensive further processing. A local oscillator is mixed (i.e. multiplied) with the RF signal to create an IF signal. Figure 4.3 shows an ideal mixer. Assuming the inputs to the ideal mixer are two sinusoids, the sum and difference frequencies at the output are given by

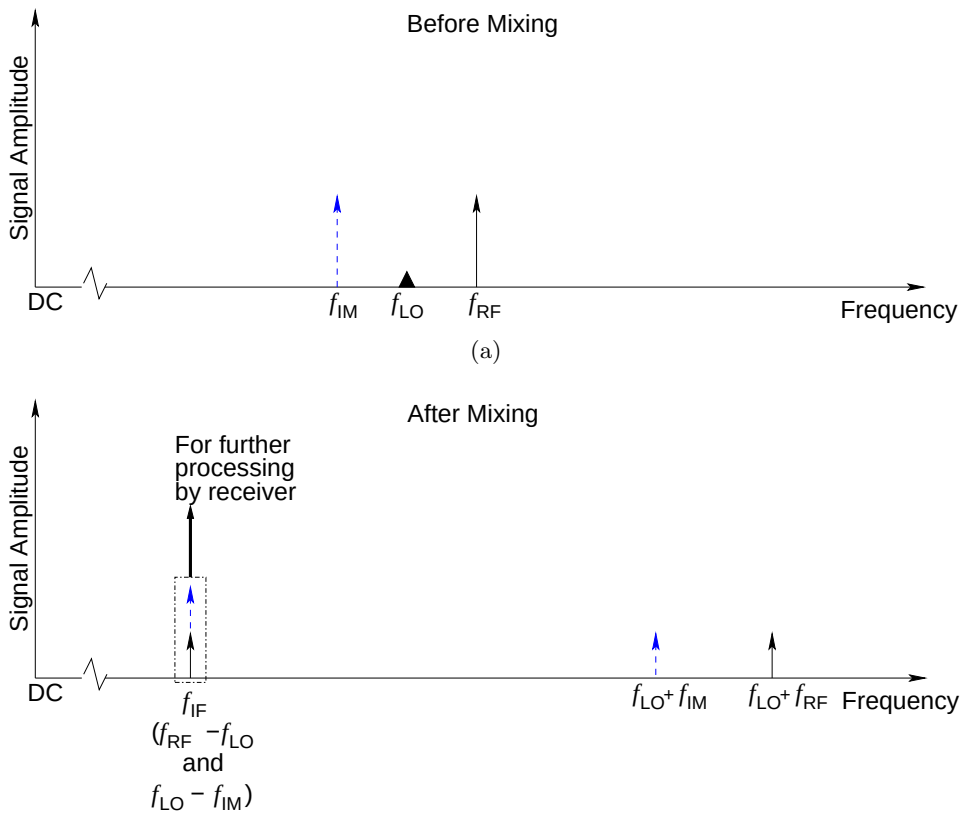

Figure 4.4: Input and output of a mixer without a preceding bandpass filter: (a) RF input signals to a mixer (desired and image signal) that are equally spaced in frequency from a local oscillator; and (b) sum and difference signals generated at the output of the ideal mixer. Further processing of the down-converted IF signal takes place in the succeeding stages of the receiver. Both desired signal (located at f_{RF}) and image signal (located at f_{IM}) down-convert to f_{IF} frequency.

$$[A_1 \cos(w_{\mathrm{RF}} t)]\,[A_2 \cos(w_{\mathrm{LO}} t)] = \frac{A_1 A_2}{2}\,[\cos(w_{\mathrm{RF}} - w_{\mathrm{LO}})t + \cos(w_{\mathrm{RF}} + w_{\mathrm{LO}})t] \tag{4.3}$$

where $w_{\mathrm{RF}} = 2\pi f_{\mathrm{RF}}$ and $w_{\mathrm{LO}} = 2\pi f_{\mathrm{LO}}$ are the frequencies in radians of the two inputs to the mixer. A_1 and A_2 are the amplitudes of the two inputs.

If the local oscillator frequency is f_{LO} and the RF signal frequency is f_{RF}, then IF frequency is given by

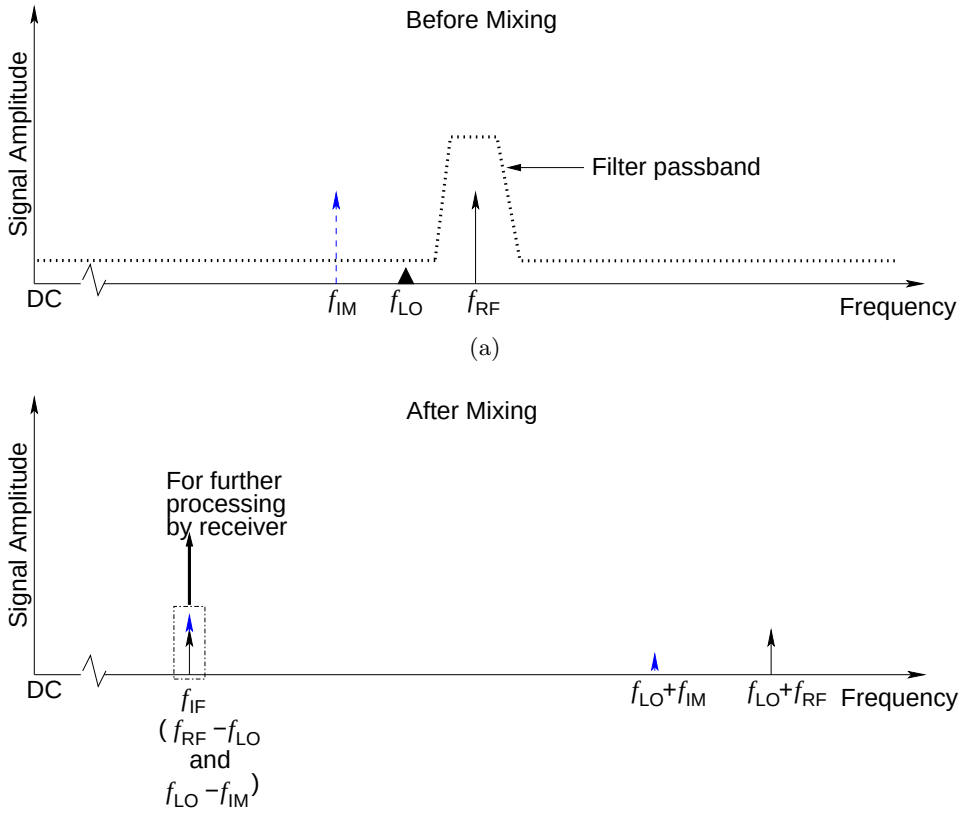

Figure 4.5: Preceding the mixer with a bandpass filter suppresses the image signal: (a) RF input signals to a mixer (desired and image signal) that are equally spaced in frequency from a local oscillator. The desired signal lies within the passband of the bandpass filter preceding the mixer while the image signal lies in the filter stopband; and (b) sum and difference signals generated at the output of the mixer. The amplitude of the down-converted image signal is reduced while the amplitude of the down-converted desired RF signal is unattenuated.

$$f_{\mathrm{IF}} = f_{\mathrm{RF}} - f_{\mathrm{LO}}. \tag{4.4}$$

The RF signal is downconverted by the mixer to the IF frequency. As shown in Figure 4.4, an interfering signal at the input of the receiving antenna that is spaced in frequency at f_{IF} from the local oscillator but at the mirror image location of f_{RF} will also down-convert to f_{IF} and cause distortion of the desired signal. The interfering signal is then defined as the unwanted image signal. To prevent down-converting the image signal to f_{IF}, the bandpass filter in the RF-front end must suppress the image signal i.e., the design should include appropriate out-of-band rejection at the image frequency. This is shown in Figure 4.5.

In the filter considered in this chapter, the image signal is above the passband and so the most rapid transition from passband to stopband is required on the high side of the filter. This characteristic is achieved through appropriate choice of filter topology.

4.3 Tunable Bandpass Filter Design

4.3.1 Tunable Distributed Resonator

Figure 4.6a shows a resonator structure used in tunable distributed microwave filters [29, 31]. Although the BST varactor is lossy, the varactor in this discussion in considered lossless to explain the basic concept of a tunable resonator. The varactor has a normalized impedance $z_c(V_B)$ where V_B is the tuning or varactor bias voltage. In Figure 4.6a, $\Gamma(x)$ is the reflection coefficient at position x looking from the left towards the right. At position B ($x = x_B$), $\Gamma(x_B)$ is determined by $z_c(V_B)$. The locus of Γ rotates clockwise as we move to the left until at position A ($x = x_A$), $\Gamma(x_A) = -1$ (a short-circuit) for resonance. The electrical length of the line at resonance is θ degrees. The resonant frequency of the resonator establishes the center frequency of the bandpass filter. Thus, as illustrated on the Smith^{TM} chart in Figure 4.6b, an increase in bias voltage causes a reduction of the varactor capacitance and $z_c(V_B)$ moves from location

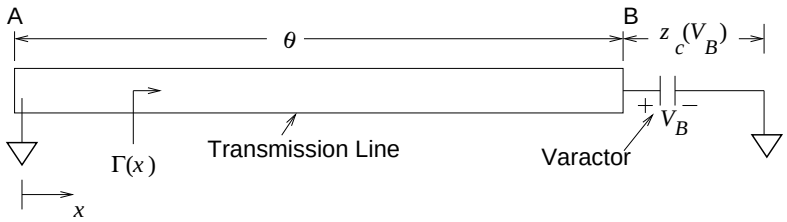

(a)

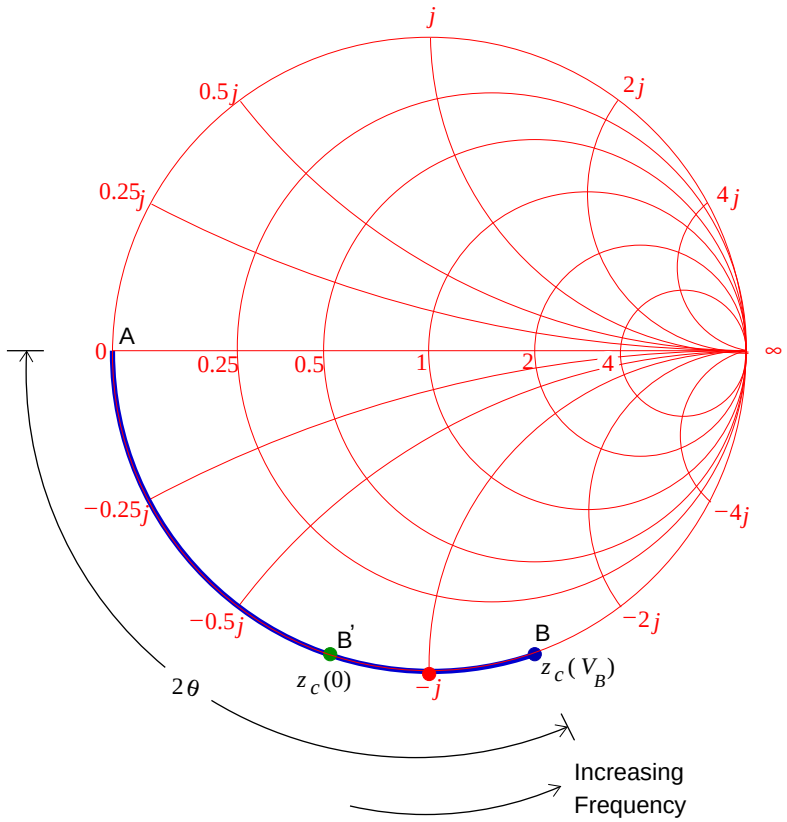

(b)

Figure 4.6: Tunable resonator: (a) cascade of a transmission line segment having an electrical length, θ, and a BST varactor with impedance $z_c(V_B)$ normalized to the characteristic impedance of the resonator's transmission line at bias voltage V_B; and (b) representation of a lossless tunable resonator on a Smith chart.

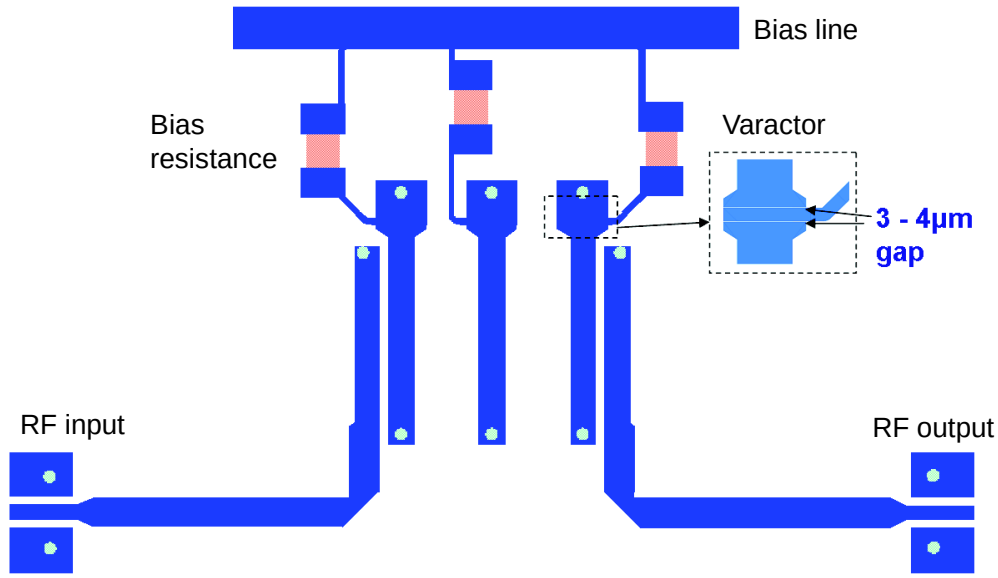

Figure 4.7: Layout representation of an integrated third-order tunable combline bandpass filter with BST gap capacitors covering 6.28 to 8.59 GHz. A zoomed in view of the capacitor is also shown. The outer two resonators of the combline filter are 305 μm wide and the center resonator is 330 μm wide by design so that all the BST capacitors have the same value.

B$'$ to B. This requires an increase in the electrical length, θ, of the transmission line for the resonator to remain at resonance. The electrical length (θ) is given by

$$\theta = \beta l = \frac{2\pi f}{v_p} l \tag{4.5}$$

where β is the phase constant, l is the physical length of the transmission line, f is the frequency and v_p is the phase velocity. Since the physical length of the line is fixed and v_p is determined by the substrate dielectric, the resonance frequency increases. Note that the angular difference between Γ_A and Γ_B is 2θ as the reflection coefficient is plotted on a Smith chart.

4.3.2 Circuit Design Using Tunable Distributed Resonators

Microstrip bandpass filters based on a Chebyshev lowpass filter prototype response are used to achieve high frequency selectivity and low-insertion loss. The topology of the microstrip filter used here is shown in Figure 4.7. This is a third-order combline filter where each of the three tunable resonators is shorted to ground on one end and connected to a variable BST capacitor on the other end. Each variable capacitor comprises two series BST gap capacitors. The two ferroelectric capacitors share a center bias line as shown in the inset in Figure 4.7. Nominally the transmission line is $\lambda/8$ long (i.e., has an electrical length of 45°) and the BST capacitor with one terminal shorted to ground provides another 45° electrical rotation, for a total resonator electrical length of 90°. Tuning the BST capacitor changes the electrical rotation contribution from the capacitor and thus the electrical length of the transmission line section required for resonance. Figure 4.6b shows the locus of the reflection coefficient of the resonator looking into the capacitor and then moving from the capacitor to the short end of the transmission line. The bandwidth of filter is determined by the coupling between the three resonators. A traditional combline filter design approach was followed with the requirement that the capacitors to be tuned were of equal value [57]. Final design optimization used electromagnetic (EM) modeling [59] to account for additional coupling from parasitics not incorporated in synthesis.

4.3.3 Fabrication

An alumina substrate with a thickness of 381 μm, dielectric permittivity (ϵ_r) of 9.9, and a loss tangent ($\tan\delta$) of 0.0002 was used. The filter was fabricated using an alumina substrate chosen for its low cost, the close match of its thermal coefficient of expansion to that of BST, and its low loss tangent [60, 61]. The thermal expansion match prevents the BST from cracking when subjected to high heat in the annealing step. The alumina substrates were polished on both sides. Via holes (150–300 μm in diameter) were laser drilled and then filled with a gold based frit. RF magnetron sputtering was used to deposit 0.5–0.6 μm thick BST film across the wafer and subsequently etched to leave BST only where required. The substrate with the patterned

BST was then annealed at 900°C for 20 hours to fully crystallize the BST film. A hysteresis test was used to confirm the paraelectric (non-hysteresis) phase of the thin film. The crystalline perovskite structure of BST was verified using a diffractometer with a CuK radiation source.

A two-step metallization process to reduce the insertion loss of the filter was used. The two-step lithography involved depositing 1.2 μm of silver for the transmission lines followed by a deposition of 0.42 μm of chromium-gold to define the BST gap capacitors. This was followed by 3 μm of copper (Cu) metallization up to 50 μm away from the capacitor gap region. The two step process enabled fine feature resolution in the vicinity of the gap capacitor while reducing metallic losses elsewhere.

4.4 Design Guidelines and Figures Of Merit Of Tunable Bandpass Filters

Most electronic system design proceeds by optimizing figures of merit. For a particular subsystem such as a filter, it is sometimes possible to develop a functional figure of merit (FOM) and a design guideline that ensures operation of the subsystem close to the optimum FOM.

Fixed frequency bandpass filter design requires that filter performance be met at a specific desired frequency. Tunable filter design, however, necessitates meeting filter performance across the entire tunable frequency range. Design guidelines and figures of merit are thus required, in addition to the synthesis procedures. A major challenge in tunable filter design is achieving high percentage tuning of the filter while managing loss, bandwidth, and out-of-band rejection.

4.4.1 Early Design Guidelines and FOM

Generally filter performance has been specified in terms of frequency tunability and the geometric mean of bandwidth and loss. However in reality it is the worst case characteristics that determine system performance.

Pleskachev and Vendik [22, 23] developed a figure of merit (FOM), FOM_1, for a tunable

BPF based on the tuning frequency range (from lower center frequency, f_1, to upper center frequency, f_2), the geometric means of the filter bandwidths (Δf_1 and Δf_2 are bandwidths corresponding to the lower and upper center frequencies respectively), and insertion losses (IL_1 and IL_2 in decibels corresponding to the lower and upper center frequencies respectively):

$$\mathrm{FOM}_1 = \frac{(f_2 - f_1)}{\sqrt{\Delta f_1 \Delta f_2}} \frac{1}{\sqrt{\mathrm{IL}_1 \mathrm{IL}_2}}. \tag{4.6}$$

Here FOM_1 has the units of dB^{-1}. Vendik and Kollberg [62] defined the commutation quality factor (CQF) for a tunable ferroelectric capacitor based on the material tunability (t) and loss factors:

$$\mathrm{CQF} = \frac{(t-1)^2}{t \tan\delta_1 \tan\delta_2} \tag{4.7}$$

where $t = C_1/C_2$, $\tan\delta_1 = \omega C_1 r_1$ and $\tan\delta_2 = \omega C_2 r_2$. Here C_1, r_1, $\tan\delta_1$, and C_2, r_2, $\tan\delta_2$ are the capacitances, equivalent series resistances, and the corresponding loss tangents at the lower and upper extremes of the tunable frequency range, respectively. CQF is independent of the device geometry and is invariant to lossless reciprocal impedance transformation. Vendik and Pleskachev defined a theoretical upper limit for FOM_1 limited by the CQF of the tunable BST capacitor [22, 20]:

$$\mathrm{FOM}_{1,\mathrm{limit}}\left(\mathrm{dB}^{-1}\right) = \frac{\sqrt{\mathrm{CQF}}}{8.68n} \tag{4.8}$$

where n is the filter order.

Design guidelines for tunable bandpass filter have previously been developed based on FOMs [22, 23] and focused on minimizing variation in bandwidth as the filter is tuned [24, 25, 26, 21]. These guidelines were based on the geometric means of the loss and bandwidth at the extremes of the filter tuning.

The design condition developed for combline filters (that have a basic resonator of the form

shown in Figure 4.6a) is that at the center (i.e. the geometric mean) of the tuning range, the electrical length of the line θ should be $53°$ to minimize the variation in bandwidth [24, 25]. The results were based on detailed analysis of combline filters and determining the stationary point in the expressions for filter bandwidth. This is an appropriate choice if the filter is to be used in many existing front-end architectures. However, with the increase in ADC performance (e.g. a 12-bit ADC with 1 GHz analog bandwidth is readily available), maintaining near constant bandwidth is not required. In an actual system, it is the worst case bandwidth that limits system performance.

In the next section an FOM and a design guideline are developed from consideration of the worst case (largest) insertion loss and bandwidth across the filter's tuning range.

4.4.2 System-Aware Design Guidelines and FOM

It is the worst case conditions that determine system performance. In particular, the maximum instantaneous bandwidth of a tunable filter is determined by the analog bandwidth of available ADCs. Three of the most important tunable filter design parameters (namely, insertion loss, bandwidth and tunability) will be discussed in this section leading to the development of the proposed FOM.

4.4.2.1 Insertion loss and Bandwidth

EM simulations of the filter with varying inter-resonator spacing is shown in Figure 4.8. As the spacings increase the coupling between the resonators decreases which reduces the bandwidth of the filter. The insertion loss correspondingly increases confirming the inverse relation between bandwidth and insertion loss [63]. As shown in Figure 4.8 increasing the inter-resonator spacing from 24.1 mils to 39.1 mils decreases the bandwidth from 0.95 GHz to 0.47 GHz while increasing the insertion loss from 5.4 dB to 9.7 dB.

The insertion loss (IL in dB), as expressed in Equation (4.9), is inversely proportional to the product of the unloaded Q of the filter resonators, Q_U, and fractional bandwidth (F_{BW}) [29,

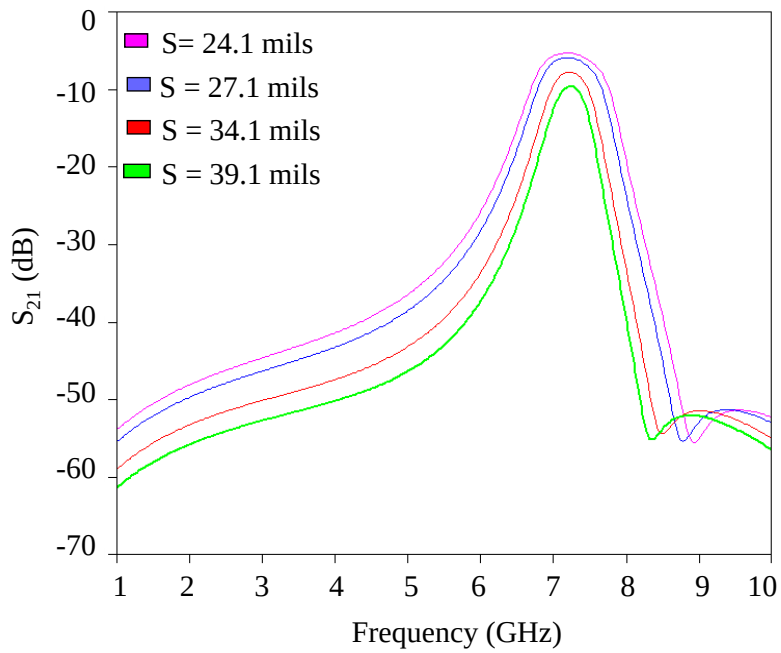

Figure 4.8: Sonnet EM simulation results of the combline filter with different inter-resonator spacings (S).

30, 31, 32]:

$$\mathrm{IL}|_{\mathrm{dB}} = \frac{4.34}{Q_U F_{\mathrm{BW}}} \sum_{i=1}^{n} g_i. \tag{4.9}$$

Here, $\sum_{i=1}^{n} g_i$ is the sum of the reactive g-values in the lowpass filter prototype and n is the order of the filter. The Equation (4.9) is derived using a low loss (high Q_U) approximation but ferroelectric filters typically have high loss. Hence, an investigation into the validity of the equation when loss is high is undertaken in the table below before considering this equation to derive the FOM.

The accurate and approximate loss equations given in [29] are used to calculate the accurate and approximate insertion loss in the table. Based on the measured results of one of the three-pole combline filters designed, a center frequency of 6.74 GHz and a bandwidth of 0.63 GHz are used in the calculations. The reactive g-values in the low-pass prototype for the three-pole

Table 4.1: Computing the percentage error between the approximate (Equation (4.9)) and accurate loss equations for different unloaded Q-factors

Q_u	accurate IL (dB)	approximate IL (dB)	% error
23	5.56	5.67	1.97
17	7.44	7.67	3.09
15	8.38	8.70	3.82
10	12.19	13.05	7.05
4	25.64	32.62	27.22

combline filter (i.e., $g_1 = 0.852 = g_3, g_2 = 1.104$) are used in the computations along with a range of low Q_U values.

Based on Table 4.1 a maximum of 4% error is observed for typical unloaded Q values (15 to 23) in the fabricated ferroelectric filters. Q_U is extracted by curve-fitting the simulations with the measured filter response for a number of filters designed in the 6 to 18 GHz range. The approximate insertion loss equation thus holds well even in the presence of high-loss (low Q_u) for ferroelectric filters.

Q_U is the overall unloaded Q of a resonator, i.e., the Q of the transmission line terminated by the varactor [3, 64]. Thus

$$\mathrm{IL}|_{\mathrm{dB}} \approx \frac{k}{Q_U F_{\mathrm{BW}}} \tag{4.10}$$

where k is a filter implementation factor. For example, a third-order Chebyshev filter with a ripple factor $\epsilon = 0.1$ (a 0.043 dB ripple), has $g_1 = 0.852 = g_3, g_2 = 1.104$ and so $k = 12.2$. In general, k, and thus insertion loss, increases for higher order filters and higher ripple. Also low-ripple Chebyshev designs are preferred over Butterworth filter designs. The trade-off in using lower-order Chebyshev design is that the filter skirts will not be as steep.

It is convenient to introduce a worst case effective filter Q defined as:

$$Q_{R,w} = \min(Q_{R,1}, Q_{R,2}) \tag{4.11}$$

where $Q_{R,1} = 1/(\mathrm{IL}_1 F_{\mathrm{BW},1})$ and $Q_{R,2} = 1/(\mathrm{IL}_2 F_{\mathrm{BW},2})$. Here, IL_1, $F_{\mathrm{BW},1}$, and IL_2, $F_{\mathrm{BW},2}$ are insertion losses and fractional bandwidths at the lower and upper extremes of the tunable frequency range, respectively. From examination of Equations (4.10) and (4.11) it is seen that $Q_{R,w}$ represents a term proportional to the worst case unloaded resonator Q ($Q_{U,w}$):

$$Q_{R,w} = Q_{U,w}/k. \tag{4.12}$$

4.4.2.2 Tunability

Filter tunability can be defined as

$$T_f = 2\left(\frac{f_2 - f_1}{f_2 + f_1}\right), \tag{4.13}$$

where f_1 and f_2 are the lower and upper center frequencies of the tuning range; and A capacitance tunability parameter can be defined as [28]

$$T_{\sqrt{C}} = 2\left(\frac{\sqrt{C_1} - \sqrt{C_2}}{\sqrt{C_1} + \sqrt{C_2}}\right) = 2\left(\frac{\sqrt{C_1/C_2} - 1}{\sqrt{C_1/C_2} + 1}\right), \tag{4.14}$$

where C_1 and C_2 are capacitor values at zero bias (corresponding to f_1) and at a maximum bias voltage (corresponding to f_2) below the breakdown voltage respectively. C_1/C_2 is the capacitance tuning ratio. This leads to the tuning sensitivity

$$T_s = \frac{T_f}{T_{\sqrt{C}}} \tag{4.15}$$

which is the ratio of the filter tunability for a given capacitance tunability. $T_{\sqrt{C}}$ is based on tuning of the center frequency of a lumped element bandpass filter being proportional to $1/\sqrt{C}$.

Thus T_s of a lumped element filter with parallel LC resonators (fixed inductor and tunable capacitor) is 1. T_s of a distributed filter is generally between 0 and 1 depending on the proportion of resonant energy stored on the variable capacitors relative to the energy stored on the distributed elements. Maximizing resonant energy storage on the variable capacitor results in high tuning sensitivity but also high loss as the variable capacitor is almost always the lowest Q element in a resonator. With the RF receiver architecture shown in Figure 4.1b, filter loss is compensated by the leading amplifier. Then maximizing T_s subject to the maximum bandwidth constraint is a key objective in tunable filter design.

Tuning sensitivity (T_s), insertion loss (IL), and fractional bandwidth ($F_{\mathrm{BW}} = \Delta f / f_0$ where Δf is the bandwidth and f_0 is the center frequency), are used in developing an FOM that is used to optimize filter performance.The relation between T_s and unloaded resonator Q for a tunable distributed resonator is discussed before defining the system-based FOM.

When an LC resonator is in resonance the resonant energy is at one time stored entirely on the capacitor and then half a cycle later all of the energy is stored on the inductor. With the transmission line resonator of Figure 4.6a the proportion of energy stored on the varactor at resonance can be changed. The transmission line stores energy in both electric and magnetic forms and when the varactor-loaded transmission line is in resonance, the proportion of energy stored on the varactor is less than in the lumped element resonator case. The greater the fraction of resonant energy stored on the varactor, the greater the impact that varying the varactor capacitance has on the resonant frequency of the resonator.

The unloaded Q of the resonator shown in Figure 4.6a, Q_U, is a function of the unloaded Q of the transmission line, $Q_{U,\mathrm{tline}}$, and the unloaded Q of the BST varactor, $Q_{U,\mathrm{cap}}$ [3]. That is, Q_U is a measure of loss and is dependent on the reactive energy stored on the line and the reactive energy stored on the capacitor. Q_U is greater when the proportion of the resonant energy stored on the capacitor is lower. However as the proportion of the energy stored on the capacitor reduces, the tuning sensitivity reduces. The relationship is approximately captured

as follows:

$$\frac{1}{Q_U} = \frac{(1-T_s)}{Q_{U,\text{tline}}} + \frac{T_s}{Q_{U,\text{cap}}}. \tag{4.16}$$

Noting that $Q_{U,\text{tline}} \gg Q_{U,\text{cap}}$ at microwave frequencies, the tuning sensitivity, T_s, is a surrogate for the proportion of the energy stored on the capacitor. When varactor impedance is chosen so that T_s is close to 1, the maximum resonant energy is stored on the capacitor and the unloaded Q of the resonator, Q_U, is equal to the unloaded Q of the capacitor, thus loss will be high. When the capacitor impedance is high, so that T_s is small, the unloaded Q of the resonator, Q_U, will be much higher than the Q of the varactor and losses will be low. For reasonable tuning sensitivity of $0.3 < T_s < 1$, $Q_U \approx Q_{U,\text{cap}}$ since $Q_{U,\text{tline}} \gg Q_{U,\text{cap}}$. This leads to a new figure of merit, FOM_2 with units of dB^{-1}, that represents a trade-off between loss and the tuning sensitivity, T_s:

$$\text{FOM}_2 = T_s Q_{R,w}. \tag{4.17}$$

Here, $Q_{R,w}$ represents a term proportional to the worst case unloaded resonator Q ($Q_{U,w}$), see (4.12). FOM_1 and FOM_2 are compared in Section 6.

A convenient metric for identifying a design is the lossless zero-bias normalized impedance of the tunable capacitor:

$$|\text{Im}\{z_c(0)\}| = \frac{1}{\omega_r C_1 Z_0} \tag{4.18}$$

where C_1 is the initial unbiased value of the BST capacitor, ω_r is the resonant frequency, and Z_0 is the characteristic impedance of the transmission line. $Q_{R,w}$, T_s, FOM_2 and optimum design range are all plotted with respect to $|\text{Im}\{z_c(0)\}|$ (which is lossless and independent of bias voltage) because it is fundamental in determining the initial design location for the tunable filter design. For each unique $|\text{Im}\{z_c(0)\}|$ value a zero-bias capacitance value (C_1) and

the corresponding physical length of the resonator is determined. The capacitance value is then varied by changing the bias voltage which changes the resonance frequency of the resonator and the center frequency of the filter. The performance of the tunable filter for the entire tuning range is defined by Equation (4.17) for each discrete $|\mathrm{Im}\{z_c(0)\}|$ value. Note that the losses due to the BST varactors and the transmission lines are accounted for in the insertion loss values used in computing FOM_2.

A higher value of FOM_2 indicates a higher performance filter resulting from a better design or better varactor. That is the tunable bandpass filter design is optimized by selecting the $|\mathrm{Im}\{z_c(0)\}|$ value that maximizes FOM_2 (subject to the maximum bandwidth and minimum rejection constraints).

4.5 Simulation and Experimental Results

Several filters operating in bands from 6 to 18 GHz were designed using the procedure described in Section 4.2 yielding filters with up to half-octave tunable bandwidths.

Figure 4.9a is a picture of the fabricated filter with crossbars between the resonators. This is an earlier version of the three-pole combline filter shown in Figure 4.7. The bandwidth of the filter was measured to be 1.5 GHz which violated the bandwidth requirement of the system-based design guideline ($<$ than the 1 GHz bandwidth constraint was not met). The topology of the three-pole combline filter is such that the bandwidth is minimum at zero-bias DC voltage and increases as the DC bias voltage is increased. This would mean that the bandwidth of the filter would be greater than the bandwidth of the downstream system ADC across the tuning range and the RF communications system would not function well. Crossbars shown in Figure 4.9a increased the coupling between the resonators. Reducing this coupling would thus reduce the bandwidth of the filter. EM simulations were performed on the filter layouts with (Figure 4.9a) and without crossbar (Figure 4.9b) to study its effect on the bandwidth. The simulated results shown in Figure 4.10 indicate that the bandwidth of the filter is reduced and the insertion loss is increased by cutting the crossbar. Based on these simulation results, an experiment was

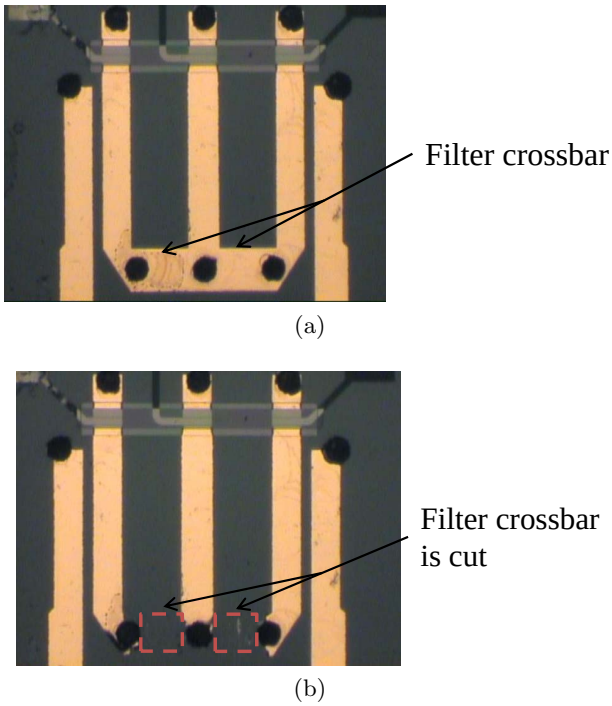

Figure 4.9: (a) filter with crossbar between the resonators; and (b) filter with crossbars cut.

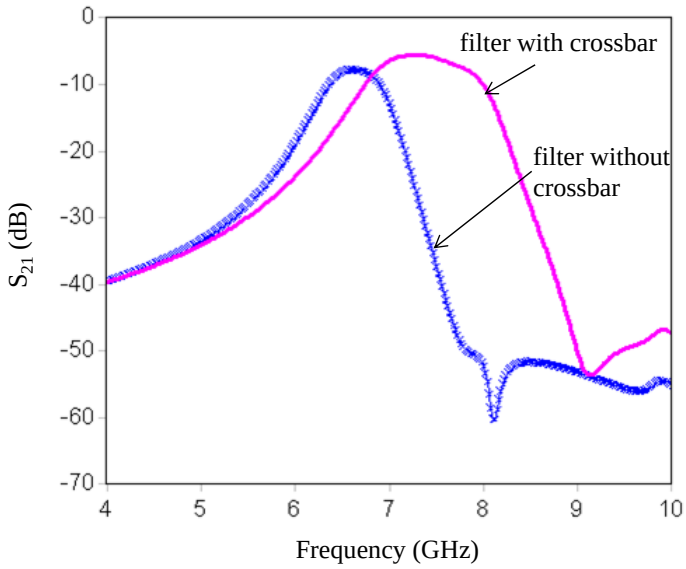

Figure 4.10: Simulated S-parameters of a filter with and without the crossbar. The cutting of the crossbar reduces the bandwidth while increasing the insertion loss of the filter confirming the inverse relationship between filter bandwidth and insertion loss.

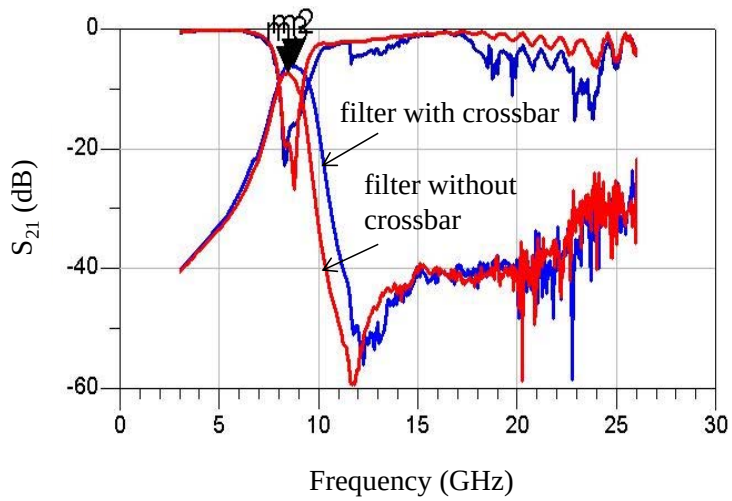

Figure 4.11: Measured S-parameters of a filter with and without the crossbar. The cutting of the crossbar reduces the bandwidth while increasing the insertion loss of the filter confirming the inverse relationship between filter bandwidth and insertion loss.

performed on a fabricated filter. The S-parameters of the filter was first measured with the crossbars between the resonators. The crossbar was later cut and the S-parameter results were measured again. Figure 4.11 shows the measured results which conforms with the simulated result.

System-aware design guidelines and FOM are used to design the two BST capacitor based tunable bandpass combline filters without cross-bars as shown in Figure 4.12.

A plot of tuning sensitivity, T_s, and $Q_{R,w}$ as a function of $|\mathrm{Im}\{z_c(0)\}|$ is shown in Figure 4.13. $Q_{R,w}$ is proportional to the overall unloaded Q of the resonator and thus inversely proportional to insertion loss. Figure 4.14 indicates that to optimize the system performance it is best to operate the filter such that $|\mathrm{Im}\{z_c(0)\}| = 1.55$ which corresponds to $\theta = 57°$ at 0 V DC bias at the bottom end of the tuning range. Note that $|\mathrm{Im}\{z_c(0)\}|$ does not vary with bias voltage.

The optimum initial (corresponding to lowest center frequency) transmission line length of $\theta = 57°$ is dependent on the capacitance tuning ratio of 2 (i.e., $C_1/C_2 = 2$), and optimizes FOM_2 subject to the maximum bandwidth constraint. For other values the optimum transmission line length needs to be re-derived. The design guideline of $\theta = 57°$ can be contrasted to the earlier

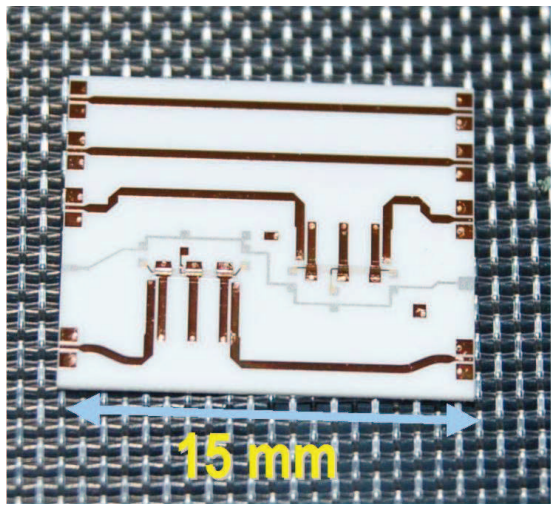

Figure 4.12: A photograph of two fabricated third-order tunable combline bandpass filters with BST gap capacitors on an alumina substrate along with two through lengths that can be used for calibration.

guideline developed using minimum variation of bandwidth across the tuning range [25]. The earlier guideline was for a transmission line length of 53° at the center of the tuning range derived for minimum bandwidth variation. For the same capacitance ratio as used here (i.e., $C_1/C_2 = 2$), this implies an initial transmission line length, $\theta = 46°$. That is, from Equation (4.10), the insertion loss (in decibels) would be multiplied by 1.27 for the same fractional bandwidth. The FOM_2 computed from measured results for two fabricated filters are also included in Figure 4.14. One of the measured results is slightly higher than the results obtained from simulations. This is because the particular filter measured had a BST capacitor with a higher Q ($Q_{U,\text{cap}}$) compared to the average value used in the simulations. A design location lower than $|\text{Im}\{z_c(0)\}| = 1.55$ was chosen to fabricate the filters as the tuning specification required higher tunability than that indicated by the optimum figure of merit.

A typical filter transmission response is shown in the simulated response in Figure 4.15a and measured response in Figure 4.16a for a filter designed at $|\text{Im}\{z_c(0)\}| = 1.07$. A tunable transmission zero due to the cross coupling between the first and the last resonator is responsible for a higher upper out-of-band rejection compared to the rejection on the lower side of the band-

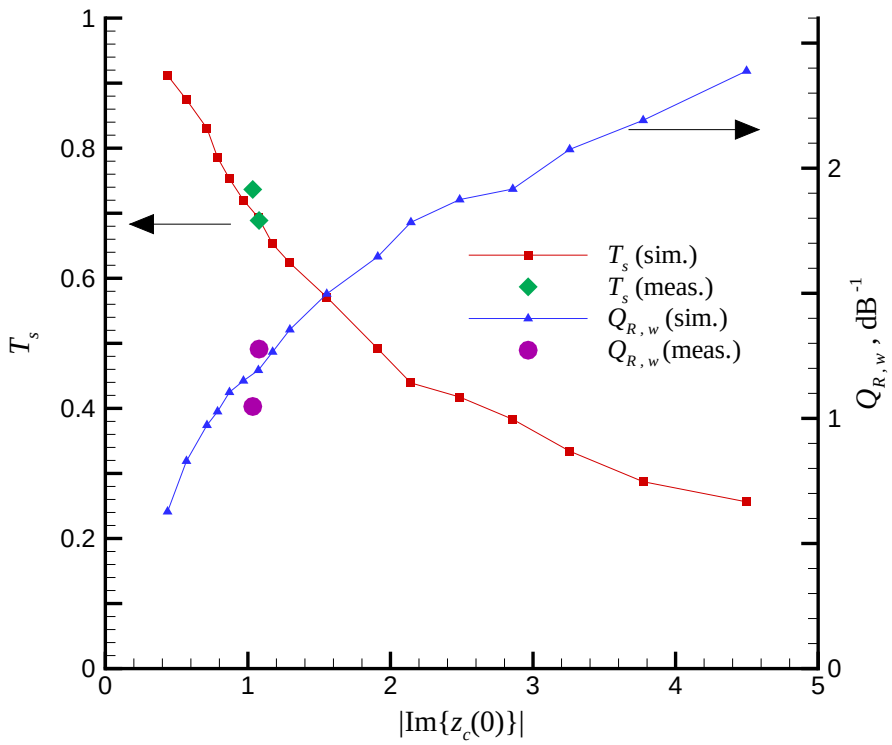

Figure 4.13: Inverse relation between tuning sensitivity (T_s) and the $Q_{R,w}$ as a function of $|\mathrm{Im}\{z_c(0)\}|$.

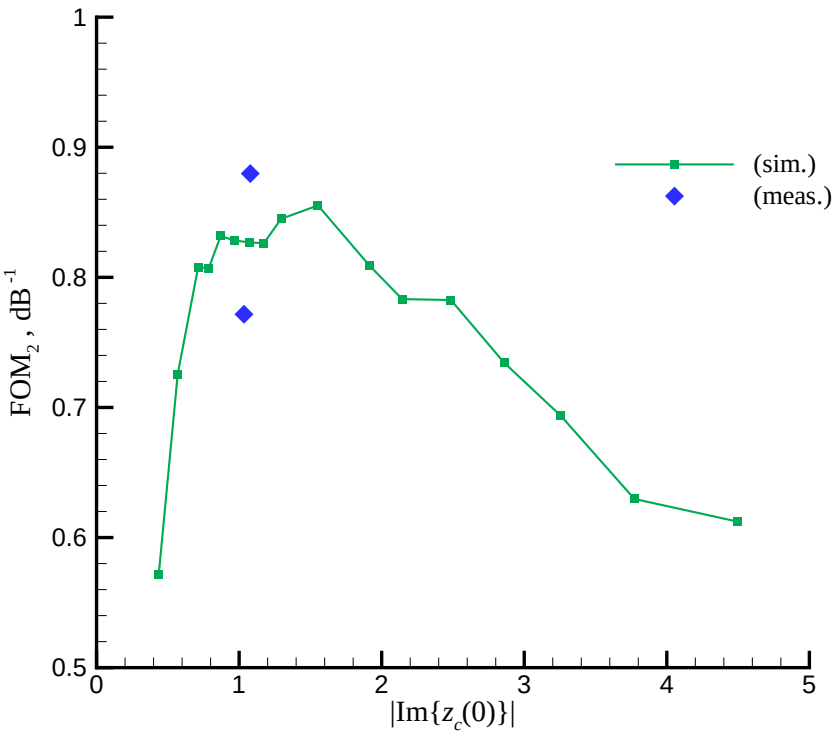

Figure 4.14: Simulated and measured FOM_2 as a function of $|\mathrm{Im}\{z_c(0)\}|$.

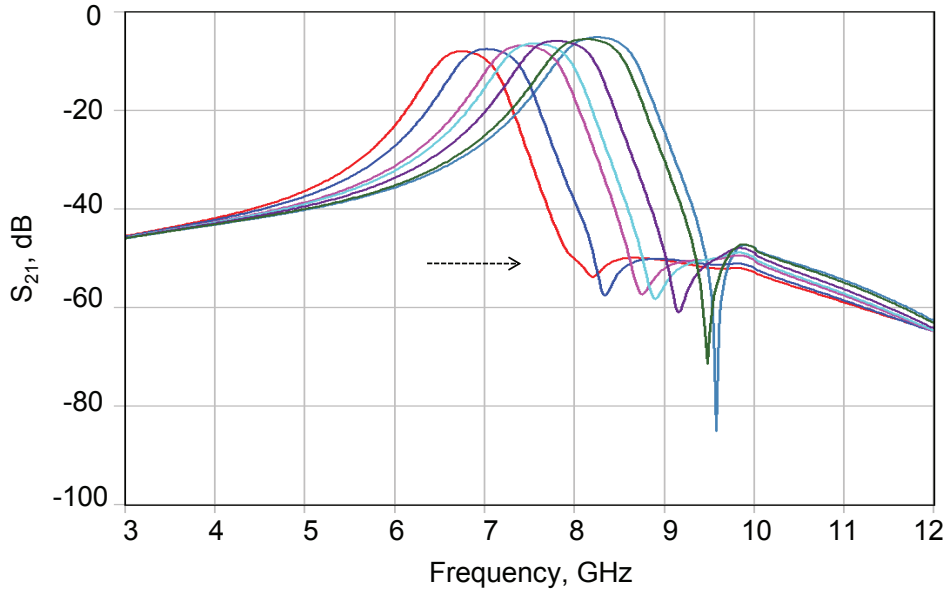

(a)

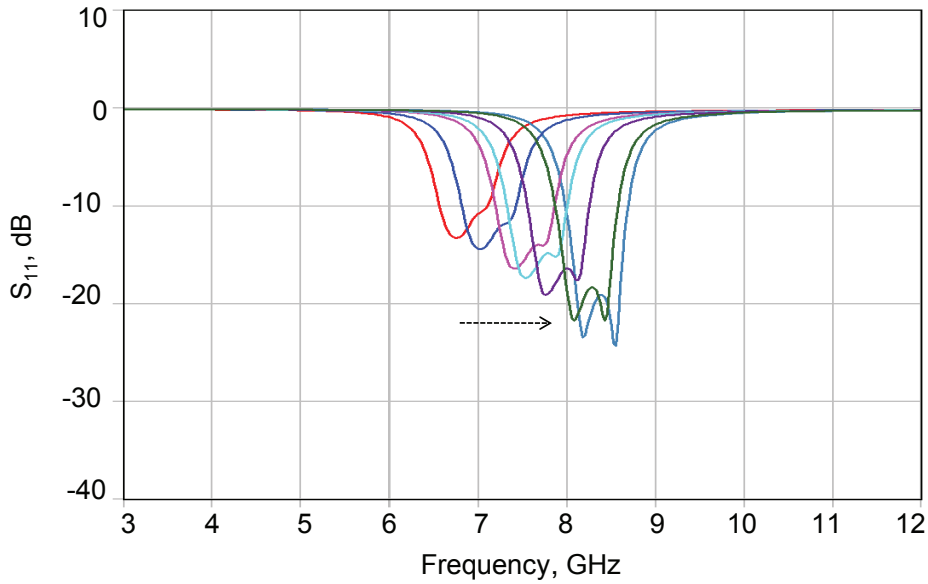

(b)

Figure 4.15: Simulated S-parameter results: (a) simulated S_{21} of a tunable BST filter covering 6.45 GHz to 8.61 GHz. The simulated response indicates a center frequency that can be tuned from 6.78 GHz to 8.28 GHz. An insertion loss of 7.95 dB and a bandwidth of 0.63 GHz corresponds to the center frequency of 6.78 GHz. An insertion loss of 5.08 dB and a bandwidth of 0.71 GHz corresponds to the center frequency of 8.28 GHz; and (b) simulated S_{11} of a tunable BST filter covering 6.45 GHz to 8.61 GHz.

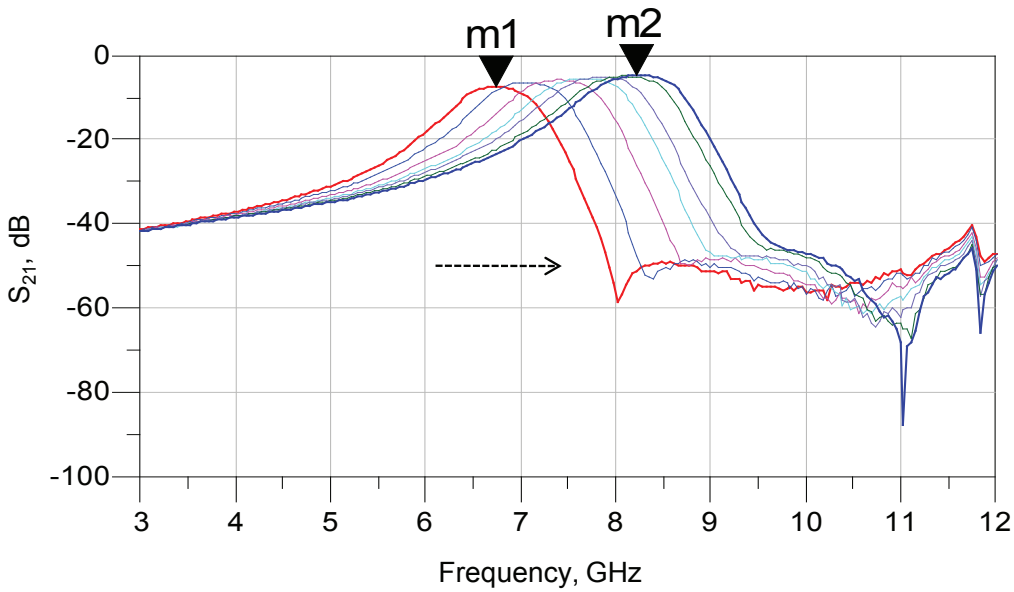

(a)

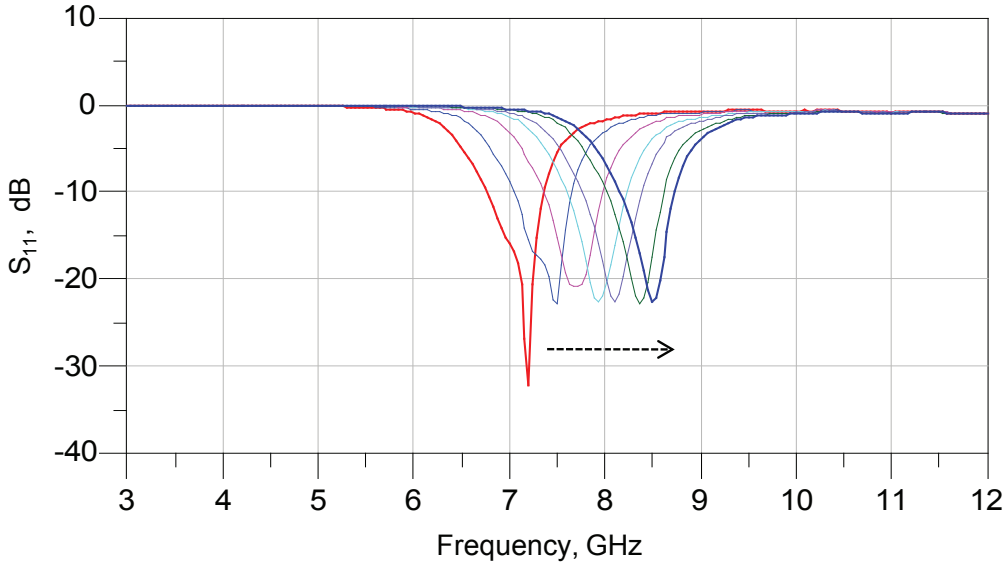

(b)

Figure 4.16: Measured S-parameter results: (a) measured S_{21} of a tunable BST filter covering 6.28 GHz to 8.59 GHz at bias voltages of 0 V, 10 V, 20 V, 30 V, 40 V, 60 V and 65 V. Marker m1 indicates a center frequency of 6.74 GHz, an insertion loss of 7.43 dB and a bandwidth of 0.71 GHz. Marker m2 indicates a center frequency of 8.23 GHz, an insertion loss of 4.82 dB and a bandwidth of 0.93 GHz; and (b) measured S_{11} of a tunable BST filter covering 6.28 GHz to 8.59 GHz at bias voltages of 0 V, 10 V, 20 V, 30 V, 40 V, 60 V and 65 V.

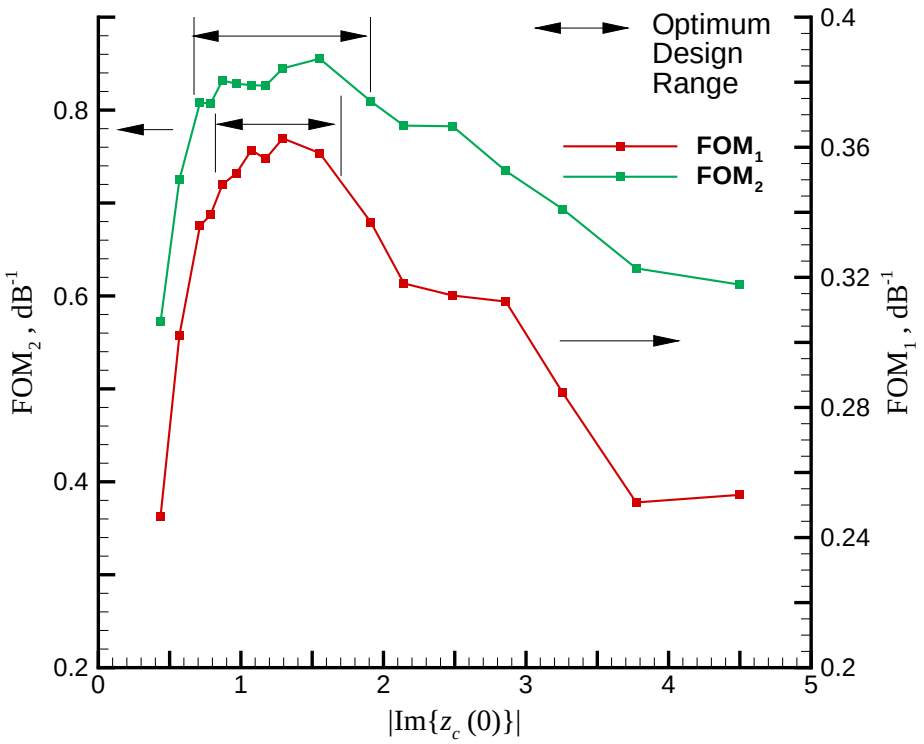

Figure 4.17: Simulated FOM_1 and FOM_2 as a function of $|\mathrm{Im}\{z_c(0)\}|$.

pass response. The measured filter response indicates a center frequency that can be tuned from 6.74 GHz to 8.23 GHz and a maximum 3-dB bandwidth of 930 MHz, within the ADC-derived limitation of 1 GHz. Thus the bandpass filter provides a variable passband from 6.28 GHz to 8.59 GHz. As expected, the insertion loss (IL $= 1/|S_{21}|$, or in decibels $\mathrm{IL}|_{\mathrm{dB}} = -\mathrm{S}_{21}|_{\mathrm{dB}}$) reduces and the bandwidth increases as the bias voltage sweeps from 0 V to 65 V. The worst case insertion loss (or transmission loss) and bandwidth, used to compute the worst case Q, are derived from the filter insertion loss and bandwidth at different bias voltages within the required tuning range. Worst case Q is used in computing FOM_2 and it thereby also influences the optimum design range derived from it as indicated in Figure 4.17. The return loss (RL) of the filter, shown in the simulated response in Figure 4.15b and measured response in Figure 4.16b, indicates that the RL is consistently higher than 10 dB in this tuning range. Figs. 4.13, 4.14 and 4.17 appear jagged due to the finite resolution in extracting the 3 dB bandwidth of the filter from simulations.

4.6 System-Aware Vis-À-Vis Early Design Guidelines and FOM

The traditional tunable filter design methodology involves maintaining a constant absolute pass bandwidth across the entire tuning frequency range. The system-aware approach discussed in this paper does not maintain constant filter bandwidth across the tuning range and instead the maximum bandwidth, which is determined by the downstream system ADC, is constrained. An earlier metric, FOM_1, is a figure of merit of a filter based on the geometric mean of bandwidth and insertion loss. It does not capture the quality of a varactor-based design given the material (or capacitance) tunabilty, and does not facilitate the tradeoff between design and material parameters. The metric introduced in this paper, FOM_2, incorporates material tunability as well as worst case bandwidth and loss. Maximizing FOM_2 optimizes the system-level performance of a tunable filter and enables the trade-off of loss and filter tunability for given material properties. It also supports material design by allowing varactor tunability and Q trade-offs, thereby enabling their impact on system performance to be determined. Ideally a figure of merit

has a constant region at its maximum value and this is observed for both FOM_1 and FOM_2 in Figure 4.17 but the optimum design range is greater for FOM_2. It is this larger optimum design space which enables the tradeoffs described above to be readily examined. So while the peak FOM_1 and FOM_2 are comparable, FOM_2 is more suited to design bandpass filters that are part of a bigger system. In short, system-aware FOM_2 ensures that filter optimization does not constrain the sub-system design parameters unless it affects the system performance, uses worst case filter design parameters, and relates frequency tunability with an associated material tunability term.

4.7 Conclusion

In this chapter, a newer RF front-end receiver architecture that can tolerate the higher loss of electronically tunable filters was discussed. In this receiver, the antenna is followed by a wide-band high-dynamic range amplifier which then feeds into a tunable bandpass filter. A system-aware design concept for tunable bandpass filters was developed. The insertion loss equation used to derive the system-aware figure of merit was based on a low loss approximation. The validity of this equation for higher loss filters was investigated. It was found that the insertion loss equation worked well even for typical low unloaded Q values (15-23) found in ferroelectric-based filters within a 4% error range. A figure of merit for a tunable microwave bandpass filter based on tuning sensitivity, and worst case insertion loss and fractional bandwidth was developed to optimize filter design for system-level integration. The system-based methodology to design tunable ferroelectric filters was compared and contrasted with the earlier methodology used. Reasons as to why the system based guideline and FOM developed here are more suited to design tunable bandpass filters that are part of a bigger system were highlighted. Simulation and measurement results for a filter designed based on the proposed design methodology were presented. While the discussion in this chapter was focused on BST-based frequency agile bandpass filter design, the design concepts can be extended to other tunable BPF designs.

Chapter 5

Two-Pole Tunable Ferroelectric Bandpass Filter

5.1 Introduction

In this chapter the design and fabrication of a frequency-agile two-pole thin-film barium strontium titanate-based filter with transmission zeroes including one zero which is tunable is discussed.

Tunable and non-tunable transmission zeroes introduced in the design increase the selectivity of the filter skirt and extend the frequency range of the stopband. The measurement details of a fabricated filter based on the design is provided. The tunable filter operates at a zero-bias center frequency of 4.25 GHz. It has center frequency tuning of 36.5%, insertion loss variation between 10.29 and 7.95 dB, and a maximum 3-dB bandwidth of 700 MHz. The bandwidth variation across the entire tuning range is 75 MHz. The filter passband shape is maintained while tuning. To the best of our knowledge, this is the first reported tunable ferroelectric bandpass filter with such a wide tuning range and a constant bandwidth.

Three-pole combline filters were designed by our research group in the past [61, 63, 14], while a two-pole modified combline filter is discussed here. The advantage of designing a two-

pole filter over a three-pole filter is that the loss is lower. Assuming the same tunability, the loss is primarily associated with, and largely proportional to, the number of resonators, i.e. the number of poles in the bandpass filter. However, the skirts of the filter response of a two-pole filter will be less steep. To compensate and recover the steepness of the filter skirt and stopband rejection level, it is necessary to introduce an out-of-band transmission zero. For a tunable filter this zero must be tunable.

5.2 Tunable Filter Design Considerations

Ferroelectric filter design is a relatively new area of research and has the potential to provide an alternative to fixed-frequency filters as they enable filter tunability. Achieving high frequency tunability and reducing the number of tunable filters in a filter bank is thus an important design consideration. Insertion loss in a filter increases the noise figure of the transceiver system and so it is preferable that the filter have a low insertion loss. Newer transceiver topologies however can tolerate a higher filter insertion loss by placing a wide-band, high dynamic range, low noise amplifier before the tunable bandpass filter [14, 65]. In newer broadband receiver front-ends the bandwidth constraint can be relaxed as high analog bandwidth ADCs (of around 1 GHz) are used. Some tunable filter implementations with higher tunability, however, can have wide bandwidth variations in the tuning range [5]. Such designs require tight bandwidth control to ensure that the higher tunability does not push the maximum bandwidth of the filter above the bandwidth of the system ADC. Filter bandwidth control is thus a useful option for a tunable filter.

The insertion loss in decibels of a bandpass filter is inversely proportional to the product of the unloaded Q of the filter resonators, Q_U, and the fractional bandwidth (F_{BW}). It is approximately expressed as [32, 29, 31, 30]

$$\mathrm{IL}|_{\mathrm{dB}} \approx \frac{4.34}{Q_U F_{\mathrm{BW}}} \sum_{i=1}^{n} g_i. \tag{5.1}$$

Here, $\sum_{i=1}^{n} g_i$ is the sum of g-values of the reactances in the lowpass filter prototype and n is the order of the filter.

Higher bandwidth corresponds to lower insertion loss but the filter skirts must still be steep and a minimum out-of-band rejection maintained. The traditional solution to achieving steep filter skirts is to use as many in-band resonators (transmission poles) as required. Increasing the number of in-band resonators increases loss roughly in proportion to the summation in Equation (5.1). One of the biggest challenges faced by ferroelectric filter designers is the high insertion loss associated with the resonators which is especially pronounced when the tunability is also high. This is because in device design there is nearly always a trade-off between loss and tunability. It is thus preferred to keep the number of ferroelectric tunable resonators as low as possible. Based on loss criteria, three poles is usually the maximum that is practical for ferroelectric filters.

In general a tunable bandpass filter will be followed by a mixer and so image rejection by the filter is especially important. Thus a tunable transmission zero on the image side of the filter passband will be designed. Further, two fixed-frequency transmission zeroes will be introduced in the stopband to provide a wide-stopband, a constant passband bandwidth while tuning, and a better impedance match at the input and output ports.

5.2.1 Design Specifications

Following are the specifications used to design the two-pole tunable ferroelectric bandpass filter considered here:

Zero-bias filter center frequency: 4.35 GHz

3-dB bandwidth: 0.55 GHz – 1 GHz

Frequency tunability: $\geq 35\%$

Passband return loss: ≥ 15 dB (or mismatch loss ≤ 0.14 dB)

Passband insertion-loss: ≤ 12 dB *see note below

Number of tunable resonators: 2

Filter response: steep filter skirt on image side of the passband

Location of tunable transmission zero: right side of passband

Stop-band rejection in immediate vicinity of upper-passband: ≥ 40 dB

The filter will provide a constant bandwidth across the entire tuning range with a tolerance of ± 75 MHz.

*One of the biggest challenges faced by ferroelectric filters with high tunability is their associated high insertion loss. A two-pole filter that would provide a lower loss than a three-pole filter with similar tunability is used as a reasonable target for the first-pass (i.e., insertion loss target is < 12 dB based on simulations of a three-pole filter with 35% tunability) while the source of this mystery loss is being explored. An attempt at finding the source of loss in ferroelectric filters is discussed in detail in Chapter 6.

5.3 Design Theory

Three pole combline filters were designed by our group in the past [61, 63, 14]. These filters have a high tunability of 22–29%. Four such filter banks are required to provide broadband coverage from 6 GHz to 18 GHz. To reduce the size and increase portability of the filter module, a newer filter design that would reduce the number of filter banks and provide the same coverage is being sought. Thus, tunability of the filter has to be greater than the existing 22–29% range while loss must be kept low. This section discusses a new two-pole filter design that has a higher tunability. The loss is designed to be lower than the existing three-pole filter with similar tunability.

A tunable distributed resonator similar to that discussed in Section 4.3 is used here with the difference being that the gap capacitor is now replaced by an IDC capacitor. By increasing

the value of the capacitance and correspondingly reducing the length of the transmission line associated with the tunable resonator, a higher proportion of energy is stored in the varactor at resonance. This increases the tunability of the resonator.

The three-pole combline filter discussed in Chapter 4 was designed using the traditional low-pass prototype with a chebyshev response. The design specifications necessitated a reject band very close to the passband which also meant that a steep transition was required from passband to stopband. A chebyshev response provided the steep roll-off required.

A low-pass prototype with a chebyshev response is thus considered a logical way to start the design for a two-pole ferroelectric filter. A transmission zero can compensate for the reduction in filter-skirt steepness observed in two-pole filters when compared with three-pole filters. This zero is required on the image side of the passband. The zero will be tunable to maintain the steepness of the filter skirt throughout the tuning range. Details about the image signal were discussed in Chapter 4.

Following the traditional filter design approach requires using a passband ripple based on design specifications (0.14 dB passband ripple corresponds to 15 dB minimum return loss in specifications) and starting the design using the low-pass prototype g-values (assuming a cutoff frequency $\Omega_c = 1$ rad/s and $g_0 = 1.0$) obtained either through calculations [31, 66] or from tables [31, 67]. The filter can then be designed following the traditional prototype-based synthesis procedure. A two-pole filter design with a low-pass prototype chebyshev filter response, however, has different source and load terminations [31, 66, 67]. In this research work, the same source and load terminations must be used. In order to design a two-pole filter having the same source and load terminations, a new design approach using electromagnetic (EM) simulations will be considered.

The filter design procedure discussed here is based on a classical filter design technique that dates as far back as 1951 [68], but is newly enabled by powerful and sophisticated EM simulation software tools backed by the enormous computing power of current day computers. The design technique requires fabricating prototypes of certain resonator structures and collecting measured

data to create design curves. The procedure is tedious as it involves fabricating the structures, measuring, modifying the design and re-measuring the hardware until the required design curves are generated. Although the complete design cycle is very long, this technique has the advantage that filters with any topology can be designed using this method. This general procedure can be used with today's EM simulator tools to fabricate virtual prototypes of resonator structures for any topology thereby creating shorter development cycles.

The classical filter design procedure discussed by Dishal [68] is based on three fundamental principles — a resonator with a synchronous tuning frequency of f_0 must exist, the coupling between the resonators are defined by a variable $K_{r,r+1}$ (where r and $r+1$ are the resonator numbers), and the coupling of the first and the last resonators to the input and output ports respectively are defined by a variable Q_{ex}. In recent years, these design curves can be generated using data from EM field solvers. Hong and Lancaster [46] have provided several filter design examples for different filter topologies using these concepts. Swanson [69], Rhea [70]and Hagenson [33] have provided practical examples of using EM simulator tools to calculate the variables such as f_0, $K_{r,r+1}$ and Q_{ex} to design filters. As there are only two resonators in this topology $K_{1,2} = K_{2,1}$ will be denoted as K in the following sections.

To support an equal source and load impedance, $K_{r,r+1}$ and Q_{ex} are defined by Dishal as follows [68]:

$$Q_{\text{ex}} = \frac{f_0}{\Delta f_{3\text{dB}}} \cdot 2 \cdot \sin(90^\circ/n) \tag{5.2}$$

and

$$K = \frac{\Delta f_{3\text{dB}}}{f_0} \cdot \frac{0.5}{\{[\sin(2r-1)(90^\circ/n)][\sin(2r+1)(90^\circ/n)]\}^{1/2}}. \tag{5.3}$$

Here, f_0 is the center frequency of the unbiased (untuned) filter, $\Delta f_{3\text{dB}}$ is the 3-dB filter

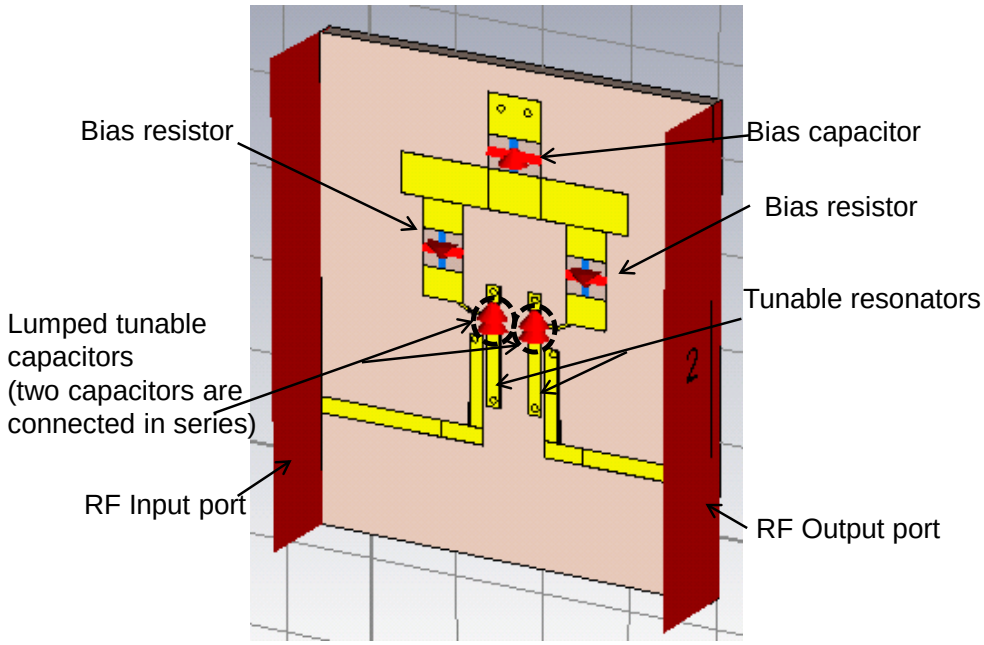

Figure 5.1: Two-pole combline layout with source and load port terminations of 50 Ω (not shown).

bandwidth, n is the order of the filter and r varies from 1 to $(n-1)$.

For the filter designed here,

$$Q_{\text{ex}} = \frac{4.35}{0.55} \cdot 2 \cdot \sin(90^\circ/2) = 11.18 \tag{5.4}$$

and

$$K = \frac{0.55}{4.35} \cdot \frac{0.5}{\{[\sin(2 \cdot 1 - 1)(90^\circ/2)][\sin(2 \cdot 1 + 1)(90^\circ/2)]\}^{1/2}} = 0.09 \tag{5.5}$$

considering $n = 2$, $r = 1$, and using the zero-bias filter center frequency and the minimum filter design bandwidth from the specifications.

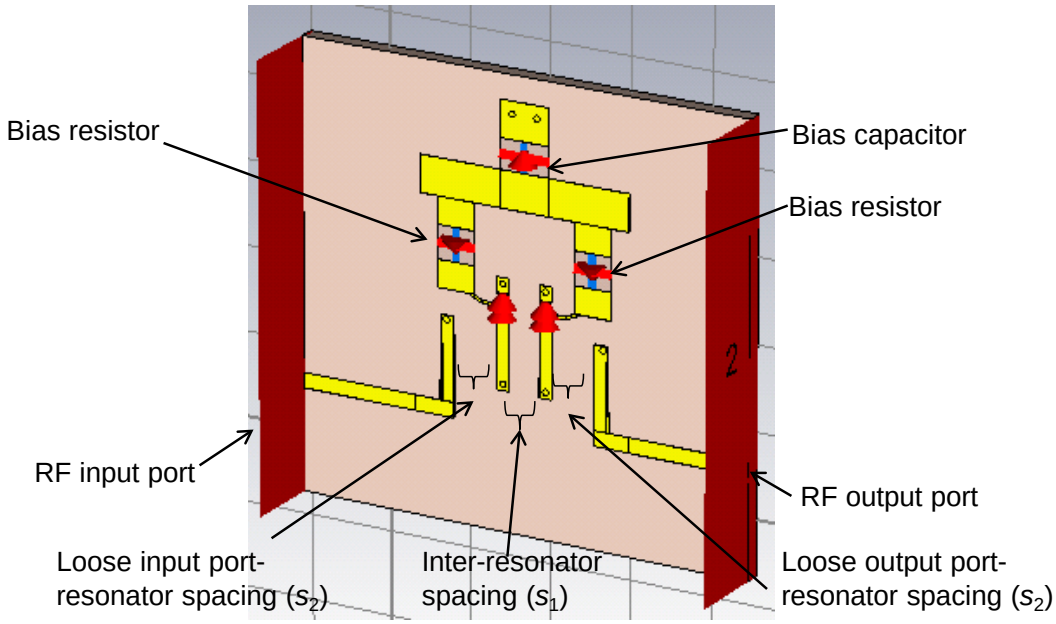

Figure 5.2: Layout in an EM simulator to compute coupling coefficient (K) for a particular inter-resonator spacing.

Figure 5.1 shows a two-pole combline layout with 50 Ω input and output port terminations (not shown) in Computer Simulation Technology's Microwave Studio (CST MWS) [56]. As a first step, the coupling coefficient, K, and external Q-factor, Q_{ex}, are calculated for different inter-resonator spacings and input/output port-resonator spacings respectively.

5.3.1 Coupling Coefficient (K)

Figure 5.2 shows the layout setup in an EM simulator to measure the coupling coefficient for a specific inter-resonator spacing (s_1). The two-resonators are loosely coupled to the input and output ports so that the influence of the ports on the measured result can be neglected. The two resonators are synchronously tuned at a frequency f_0. The coupling between the two resonators causes a displacement of their resonant frequencies by Δf. The frequency domain S_{21} plot indicates a double peaked response as shown in Figure 5.3. The nulls between the peaks should be below -30 dB to guarantee loose coupling [70, 33]. The lumped capacitors in the combline

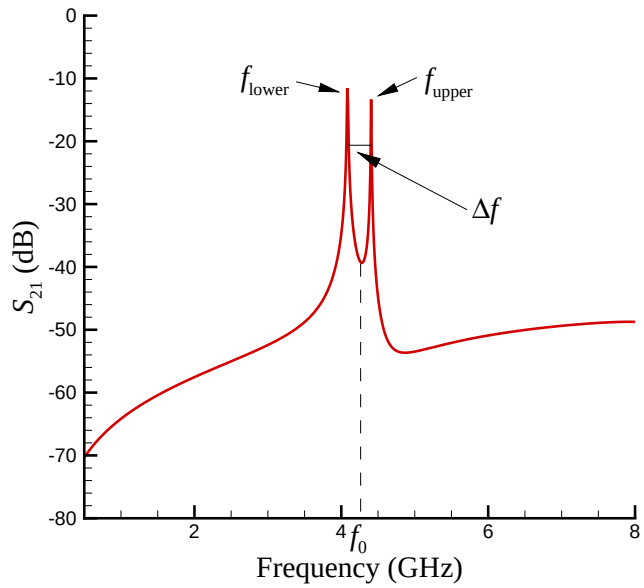

Figure 5.3: Frequency domain S_{21} plot of the layout in Figure 5.2 indicates a double-peaked response. This plot is used to compute K for a particular inter-resonator spacing (s_1).

filter are tuned to center the response at the desired center frequency. The coupling coefficient K is given by [69, 70, 33]

$$K = \frac{f_{\text{upper}} - f_{\text{lower}}}{f_0}. \tag{5.6}$$

As shown in Figure 5.3, f_{lower} is the frequency corresponding to the first peak, f_{upper} is the frequency corresponding to the second peak, and f_0 is the center frequency of the filter.

EM simulations are run for different inter-resonator spacings and the coupling coefficient is computed for each spacing. Figure 5.4 is a plot of coupling coefficient, K, as a function of the inter-resonator spacing. A value of $s_1 = 654.4$ μm corresponding to $K = 0.09$ is chosen for the design.

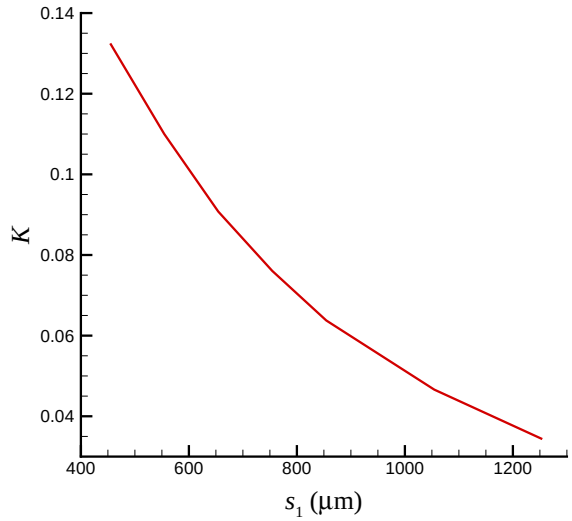

Figure 5.4: A plot of coupling coefficient (K) as a function of inter-resonator spacing (s_1) using the layout in Figure 5.2.

5.3.2 External Q-factor (Q_{ex})

Figure 5.5 shows the layout setup in an EM simulator to measure the coupling between the first (or last) resonator, and the input (or output) ports. A single tunable resonator is coupled to the input and output ports. The spacings between the resonator and the input/output port controls the loaded Q at each end resonator in the filter. A frequency domain S_{21} response of the layout in Figure 5.5 is shown in Figure 5.6 for a particular resonator-port spacing (s_2). The lumped model of BST capacitor in the resonator is tuned to center the response at the desired center frequency. The external Q (Q_{ex}) is given by

$$Q_{\text{ex}} = \frac{2f_0}{f_{3-\text{dBup}} - f_{3-\text{dBdown}}}. \tag{5.7}$$

EM simulations are run for different resonator-port spacings and the external Q-factor is computed for each spacing. Figure 5.7 is a plot of external Q-factor, Q_{ex}, as a function of the resonator-port spacing. It can be seen that a value of $Q_{\text{ex}} = 11.18$ would require a very small

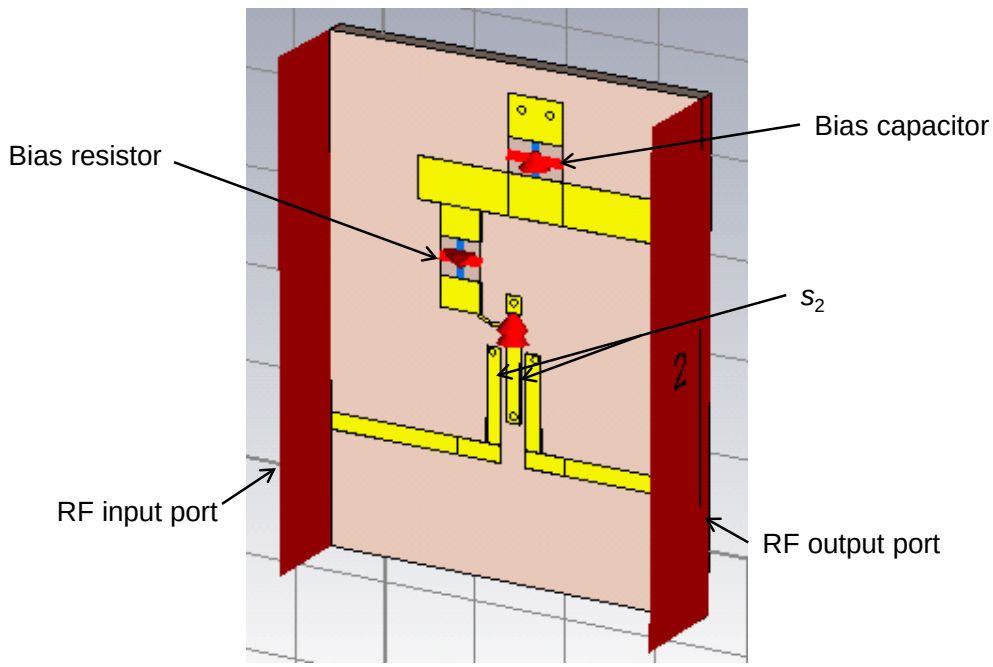

Figure 5.5: Layout in an EM simulator to compute external Q (Q_{ex}) for a particular resonator-port spacing (s_2).

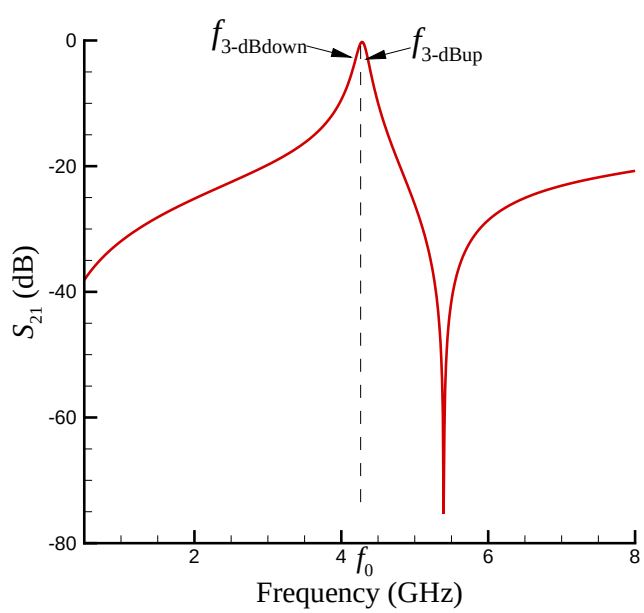

Figure 5.6: Frequency domain S_{21} plot of the layout in Figure 5.5 used to compute Q_{ex} for a particular resonator-port spacing (s_2).

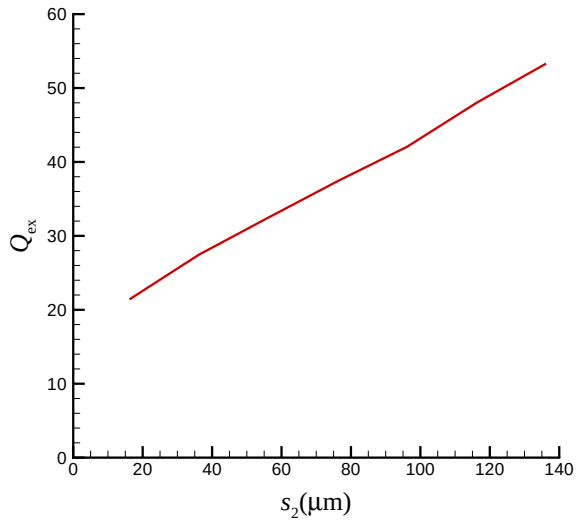

Figure 5.7: A plot of coupling coefficient (Q_{ex}) as a function of resonator-port spacing (s_2) using the layout in Figure 5.5.

value of $s_2 < 16$ μm. Fabrication inter-metal trace spacing requires $s_2 \geq 70$ μm. Hence a value of $s_2 = 76.2$ μm with a corresponding Q_{ex} value of 37.41 is chosen for the first pass. A design step that lowers the value of Q_{ex} bringing it close to the required value for equal source and load terminations will be discussed in the Section 5.3.4.

5.3.3 Filter Design

A two-pole combline filter as shown in Figure 5.1 with the inter-resonator spacing, $s_1 = 654.4$ μm and port-resonator spacing, $s_2 = 76.2$ μm is simulated. The transmission response (S_{21}) in dB of the filter is shown in Figure 5.8. The S_{21} of the layout indicates a mismatch loss of 5.2 dB (as expected due to a higher value of Q_{ex} chosen) and will be improved in the following steps.

To increase the steepness of the filter skirt, a tunable zero is added by providing multiple paths between the source and load as shown in Figure 5.9. The transmission zero also tunes as one of the paths (Path I) include resonators that are tunable. A frequency response plot (Figure 5.10) of the two-pole modified combline filter with a source-load (S-L) cross-coupling path

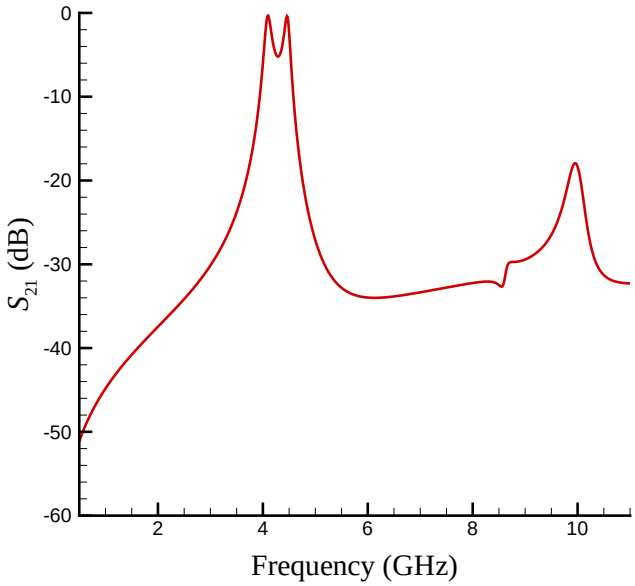

Figure 5.8: Transmission response (S_{21} in dB) of the two-pole combline layout shown in Figure 5.1.

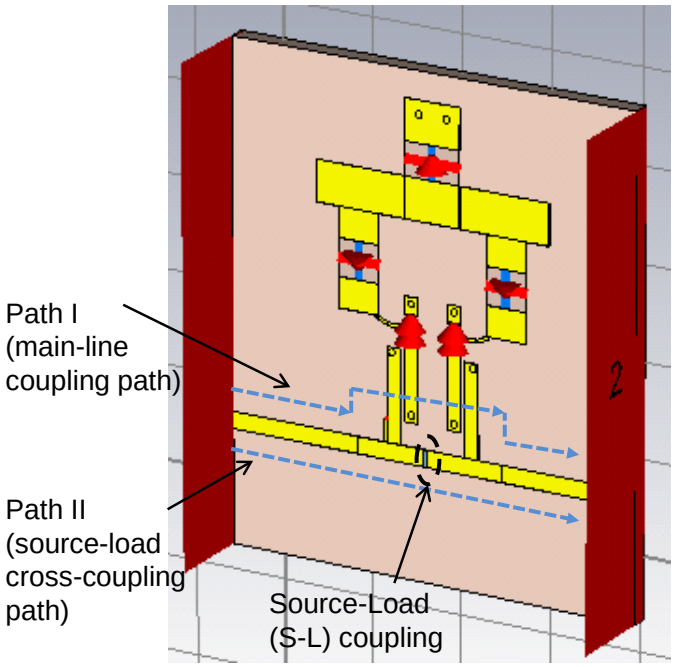

Figure 5.9: Modified two-pole combline layout with a cross-coupling path in addition to a main-line coupling path.

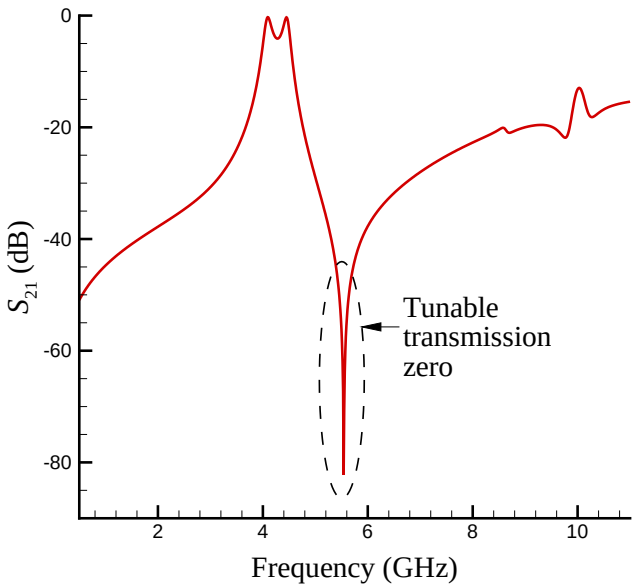

Figure 5.10: Transmission response (S_{21}) plot of the modified two-pole combline layout with a cross-coupling path in addition to a main-line coupling path as shown in Figure 5.9.

shows a transmission zero. It can be observed that the out-of band response beyond the transmission zero shows a poor stop-band rejection. A non-tunable transmission zero is introduced that serves three purposes — it will create an extended stop-band rejection of $\geq$ 40 dB close to the upper passband, it will reduce Q_{ex} and thus improve the return loss without violating the fabrication inter-metal trace spacing constraint, and it will also create a constant bandwidth filter. Transmission zero design details will be discussed in Section 5.3.4.

Figure 5.11 is the layout of the filter including open stubs that realize the non-tunable transmission zero. An EM simulation of this filter indicates a response as shown in Figure 5.12. A mismatch loss of 0.46 dB (which corresponds to a return loss of 10.01 dB) is observed. It should be noted that the return loss of the filter was improved due to the addition of the two open stubs that also serves to provide a better impedance match. The return loss of the filter however still does not meet the design specifications of $\geq$ 15 dB. The filter design until now used a lossless lumped capacitor model in place of the BST capacitor layout to reduce the

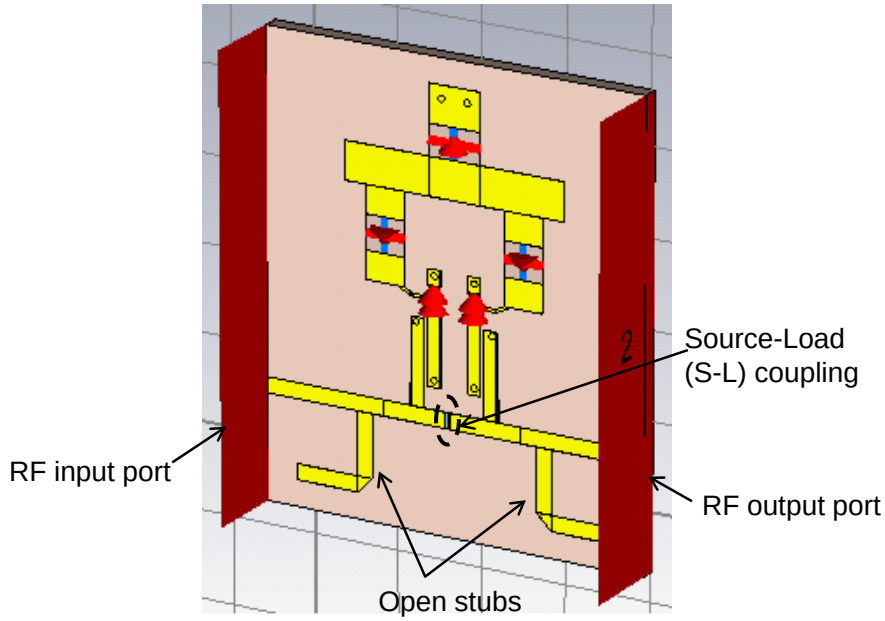

Figure 5.11: Modified two-pole combline layout with source-load coupling and open stubs.

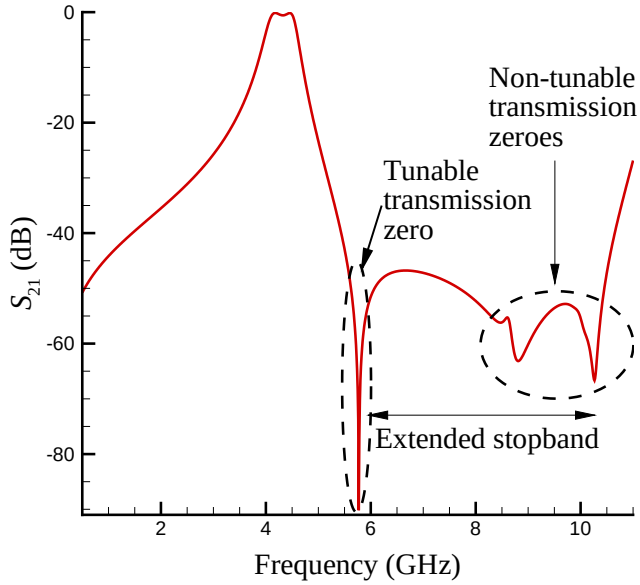

Figure 5.12: Transmission response (S_{21}) graph of the layout in Figure 5.11.

simulation and design time. A full-wave EM simulation of the complete filter that includes all the couplings and parasitics is thus undertaken before making any further modifications to the filter design.

Up to now, EM simulations were performed using CST MWS. However, the complete EM simulation of the filter including the capacitor layout will be performed in Sonnet EM software [59] due to memory requirements that prevented the use of CST. Sonnet EM software is based on the method of moments (MOM) technique and takes full advantage of the mathematically robust and reliable FFT formulation. Sonnet thus allows bigger and denser structures to be simulated with lower computational memory constraints while maintaining outstanding accuracy. This allows for simulation of two thin-film high dielectric constant BST capacitor layouts to be simulated side-by-side, a traditionally challenging problem to resolve.

The layout of the filter is broken into two parts — the low permittivity filter layout section and the mixed permittivity (thin-film of high-permittivity BST substrate over the low-permittivity substrate) BST capacitor part as shown in Figure 5.13. The filter response shown in Figure 5.14 indicates a return loss of 16.38 dB (or mismatch loss of 0.1 dB). Details of the BST capacitor and filter layout setup in EM simulations are discussed in Chapter 6.

The filter simulations performed until now are purely lossless. Simulation results that include loss are discussed in Section 5.6.1.

5.3.4 Tunable and Non-tunable Transmission Zero Design

Transmission zeroes (or attenuation poles) are created when $S_{21} = 0$ for the filter at specific frequencies. They can be implemented using (a) cross-coupled resonators [71], (b) asymmetric input/output feed-lines for the filter [72], (c) multi-resonator coupling using non-resonating components [73], and (d) an auxiliary inductively coupled ground plane [74].

Figure 5.15 is the coupling diagram [75, 76] of the filter. The modified two-pole combline filter introduces three out-of-band transmission zeroes — one tunable (tunes with the passband) and two non-tunable.

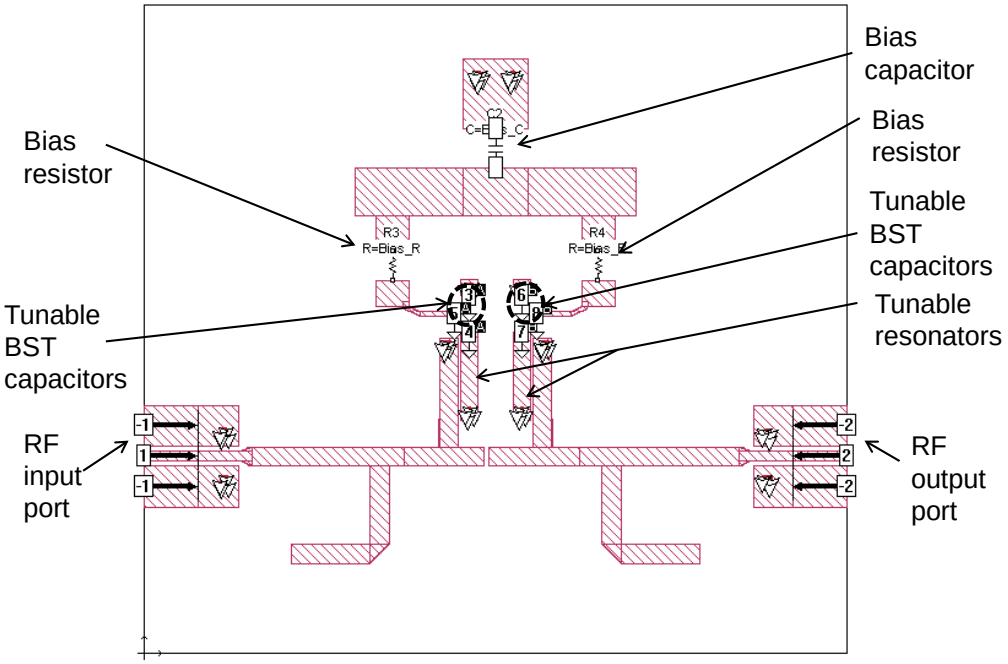

(a)

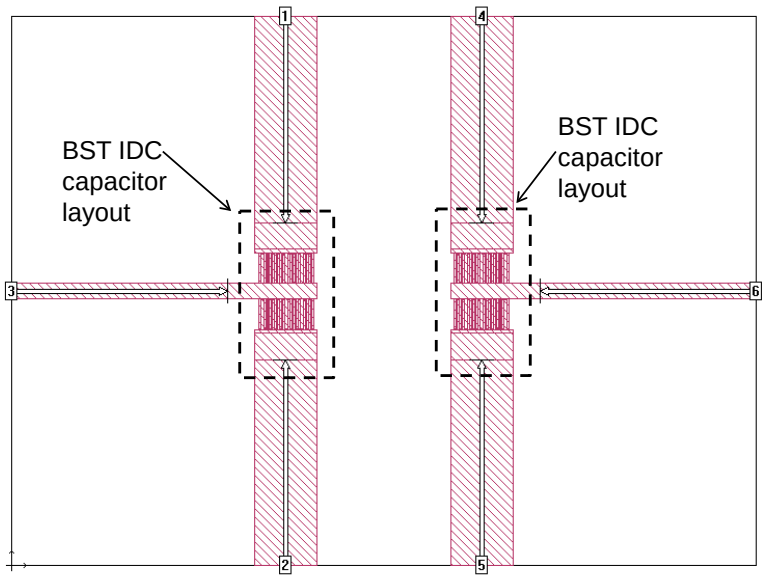

(b)

Figure 5.13: Simulation of the complete filter layout is partitioned into two sections based on the substrate permittivities in the layout. The two sections are combined together using a top-level netlist file in Sonnet EM software: (a) low substrate permittivity section of the layout; and (b) mixed substrate (thin-film of high-permittivity substrate over the low-permittivity substrate) section of the layout.

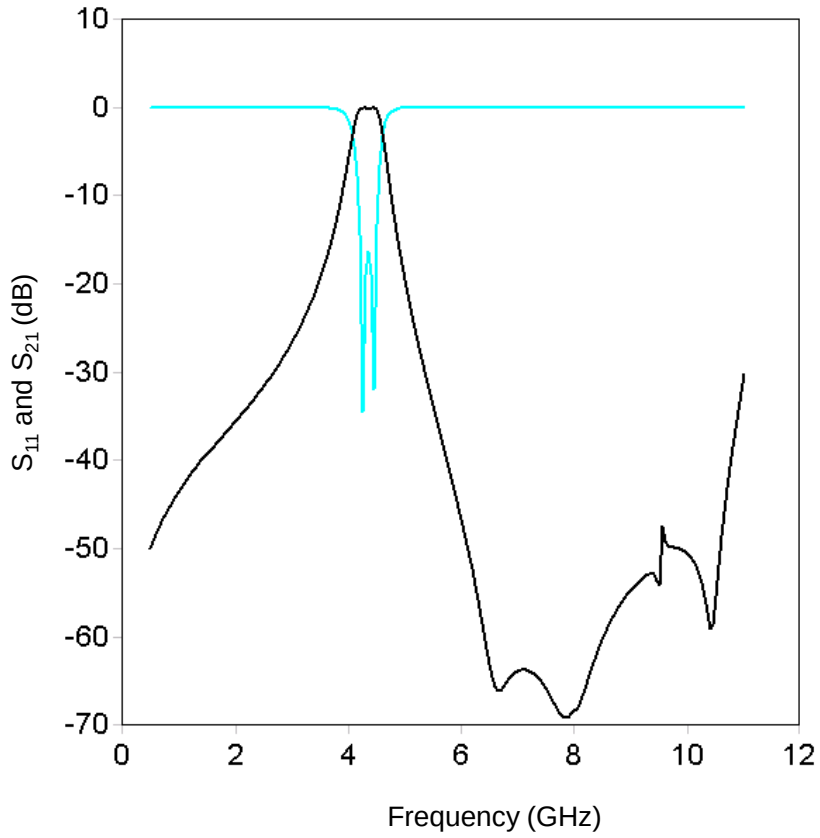

Figure 5.14: Lossless simulation of the complete filter layout shown in Figure 5.13.

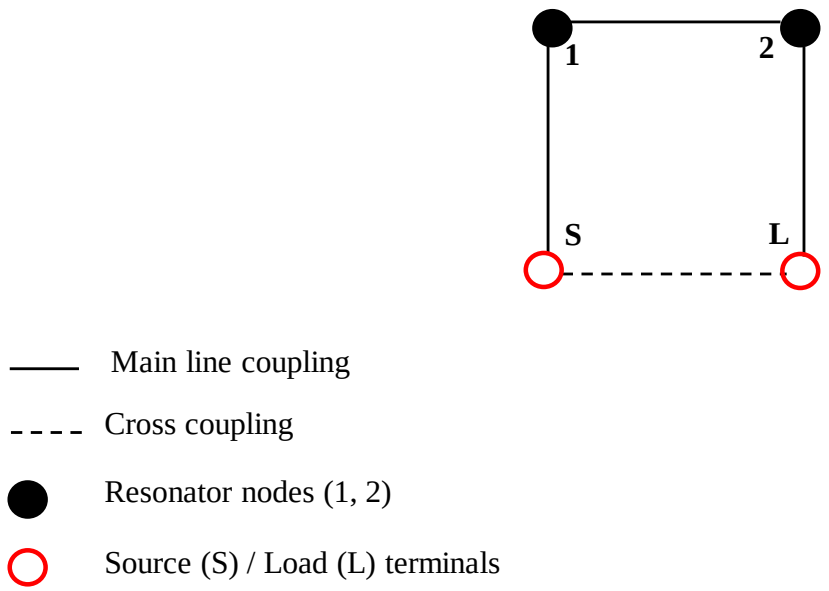

Figure 5.15: Coupling diagram of the two-pole modified combline filter.

5.3.4.1 Tunable Transmission Zero Design

A tunable transmission zero increases the steepness of the filter skirt for the entire tuning range as it can be tuned along with the filter passband. The tunable zero is created by a direct source-load cross-coupling path introduced (dashed straight line connection between source and load, [S-L]) in addition to the filter resonator coupling path (main line coupling [S-1-2-L]) as shown in the coupling diagram in Figure 5.15. As the main line coupling path has tunable resonators, the transmission zero is also tunable.

The Y-parameter method will be used to design transmission zeroes [74]. The overall Y_{21} (and S_{21}) [74, 77] goes to zero at a specific frequency. S_{21} and Y_{21} are related as follows:

$$S_{21} = \frac{-2Y_{21}Y_0}{(Y_{11}+Y_0)(Y_{22}+Y_0) - Y_{12}Y_{21}}. \tag{5.8}$$

Hence, a transmission zero will result if the magnitude of Y_{21} in the two-paths are equal and

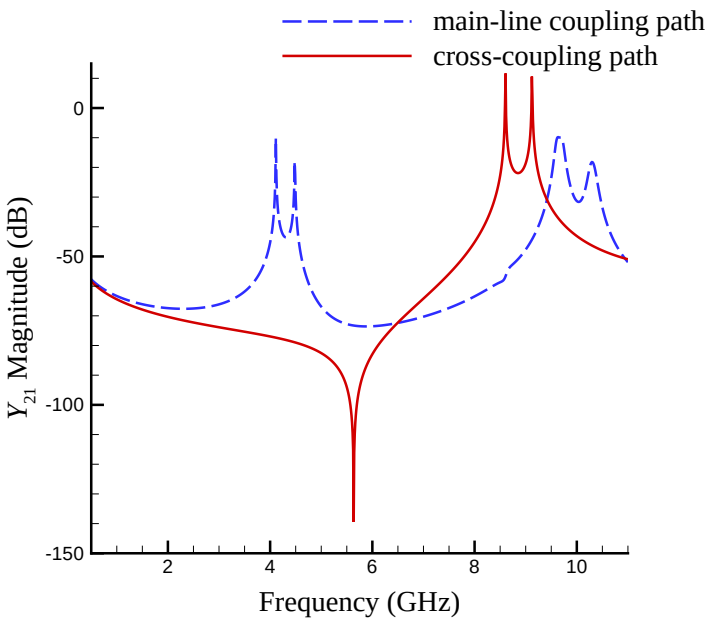

(a)

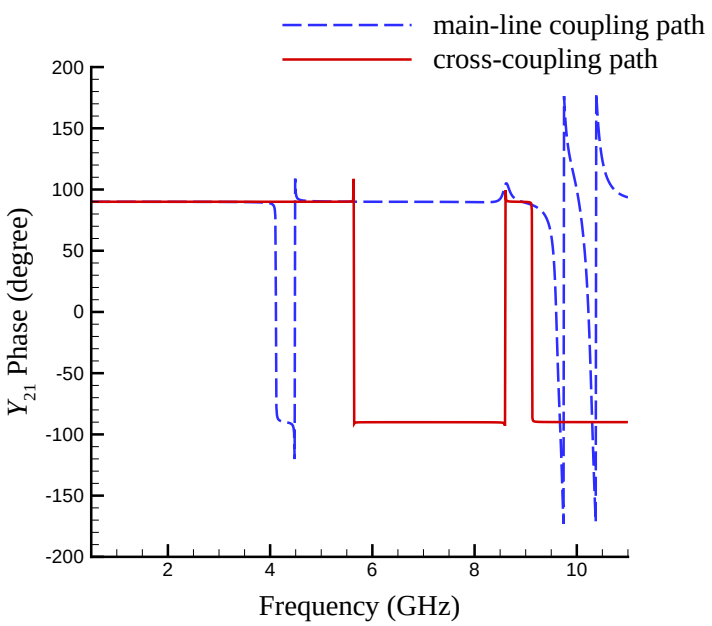

(b)

Figure 5.16: Magnitude and phase plots of Y_{21} for the two paths between the input and output ports — main-line coupling path and the cross-coupling path: (a) magnitude plot of Y_{21} for the main-line coupling and the cross-coupling paths; and (b) phase plot of Y_{21} for the main-line coupling and the cross-coupling paths.

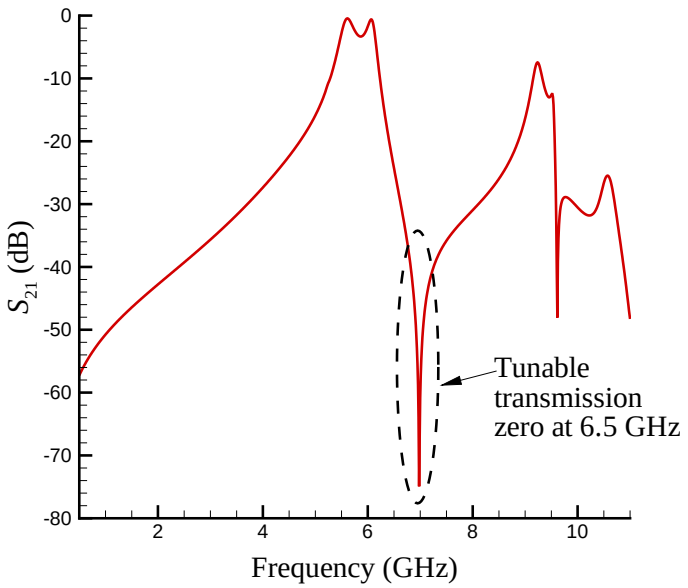

Figure 5.17: The parallel-combined S_{21} response of the separately simulated main-line coupling path and cross-coupling path indicates a transmission zero as expected at 6.5 GHz confirming the prediction of the transmission-zero based on the results in Figure 5.16.

the phase of Y_{21} in the two paths are 180° apart. The main-line coupling path and the cross-coupling path (as shown in Figure 5.15) are separately simulated and the resultant magnitude and phase of Y_{21} are plotted as a function of frequency. Figure 5.16 presents the magnitude and phase plot of Y_{21}. It can be seen that the magnitude of Y_{21} for the two-paths are equal and the phase between the paths is 180° at 6.5 GHz. The parallel-combined S_{21} response of the separately simulated main-line coupling path and cross-coupling path indicates a transmission zero as expected at 6.5 GHz (Figure 5.17) confirming the prediction of the transmission-zero based on the results in Figure 5.16.

An EM simulation of the layout comprising the two-blocks together however indicate a shift in the transmission zero frequency to the left as shown in Figure 5.10. This indicates that the coupling between the tunable resonators and the S-L coupling gap was unaccounted for when the sub-blocks were simulated separately. However a combined EM simulation captures this

additional coupling between the metal traces.

5.3.4.2 Non-tunable Transmission Zero Design

A technique discussed in [5] will be used to provide a constant bandwidth across the entire tuning range for the tunable filter. The method requires introducing a transmission zero that is appropriately placed above the tuning range of the passband such that the attenuation pole restricts the widening of the passband as the filter is tuned thereby limiting the bandwidth. The frequency location of the transmission zero is very important. If the transmission zero is placed far away from the tuning passband it will not create a constant passband width. On the other hand if the transmission zero is too close to the passband, the passband shape will not be maintained for the entire tuning range.

A non-tunable transmission zero location between 9.5 and 10.5 GHz is considered appropriate based on the simulations. The design begins with a quarter-wavelength long open stub designed based on the LineCalc tool in Advanced Design System (ADS). This tool uses the microstrip model to calculate the approximate physical length of the line based on other input parameters such as the height (381 μm) and permittivity (9.9) of the substrate, and frequency (10 GHz). A physical length of 2900 μm for the open-stub is calculated based on the inputs provided. A through-line between the ports 1 and 2 with two open stubs as shown in Figure 5.18a will create a transmission zero at 9.7 GHz (Figure 5.18b). To incorporate this open stub into the filter design shown in Figure 5.9, the cross-coupling path between the input and the output ports is considered. Figure 5.19a shows the cross-coupling path with the two-open stubs. It is obvious that the difference between Figure 5.19a and Figure 5.18a is the existence of a gap capacitance between the input and output ports. An EM simulation of Figure 5.19b indicates two degenerate transmission zeroes due to the additional series reactance provided by the capacitor. The value of the gap capacitor (i.e. the gap spacing) can be easily adjusted to move the locations of the two transmission zeroes generated. Computational experiments were carried out to finalize the location of the open stubs (2356.6 μm from the input and output

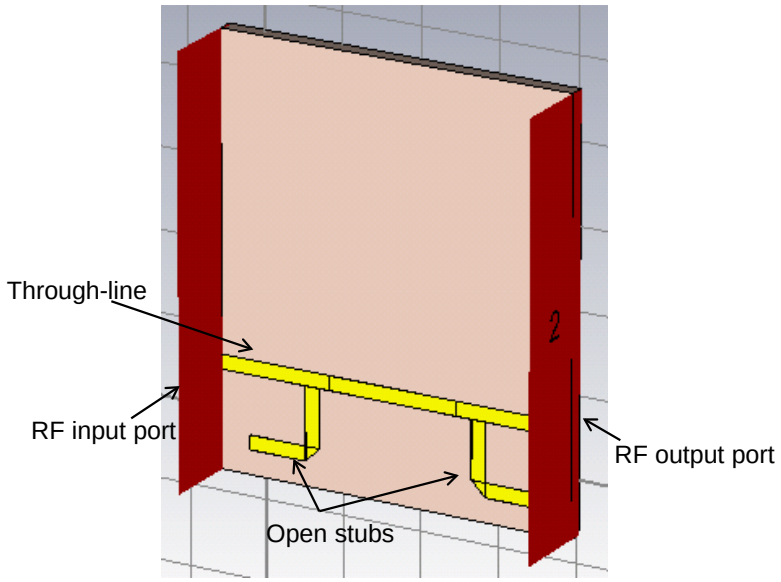

(a)

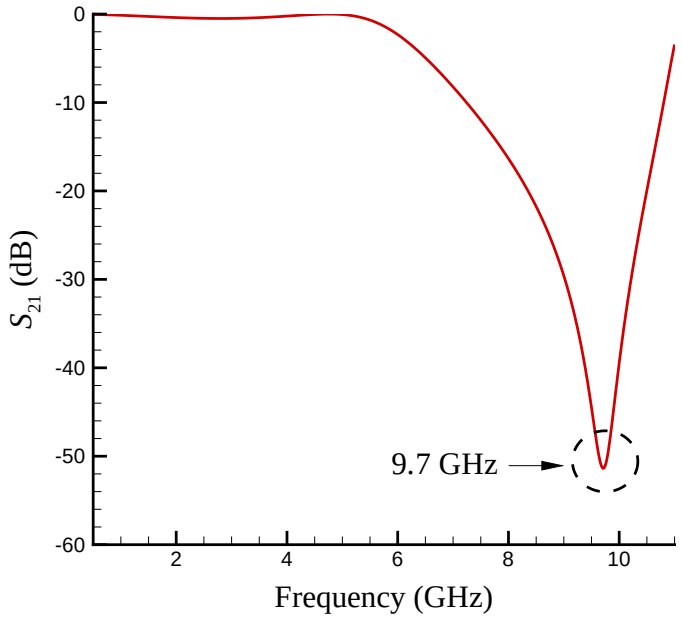

(b)

Figure 5.18: Layout and simulated result of a through-line between the input and output ports with two open stubs: (a) through-line with an input and output stub; and (b) simulated result.

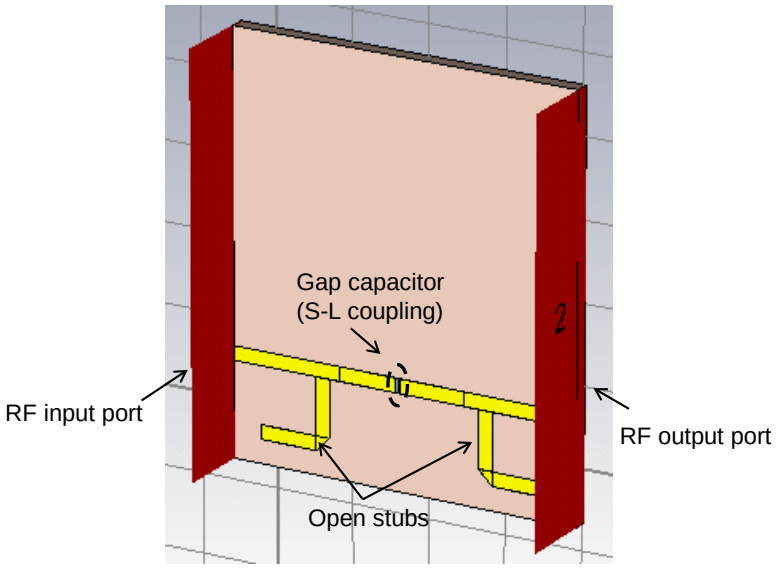

(a)

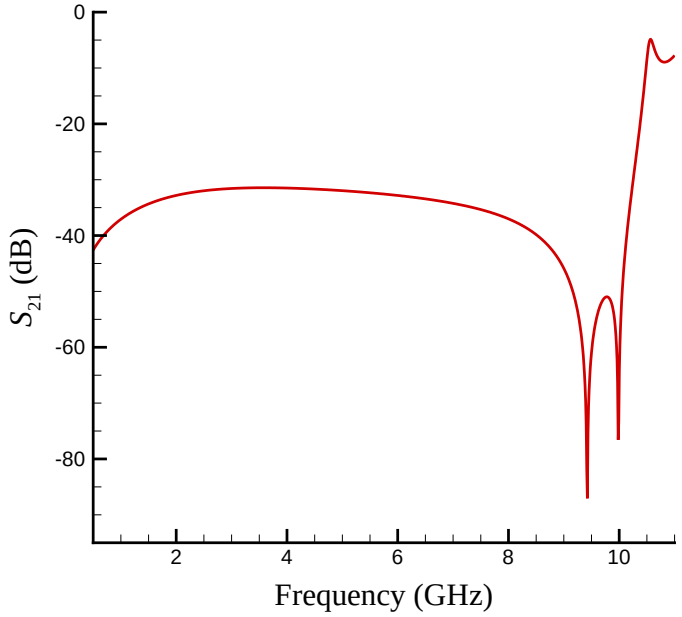

(b)

Figure 5.19: Layout and simulated result of the filter cross-coupling path between the input and output ports with two open stubs: (a) filter cross-coupling path with an input and output open stub; and (b) simulated result.

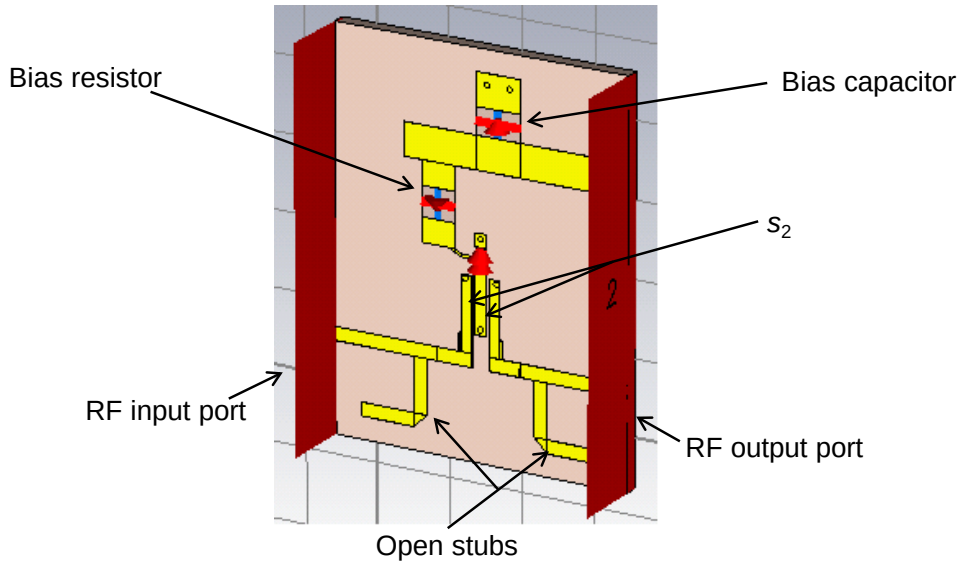

Figure 5.20: Layout in an EM simulator to compute the modified external Q (Q_{ex}) after introducing the open-stubs on the input and output port traces.

ports) and the gap spacing (100 μm). These zeroes could be tuned by introducing a tunable ferroelectric capacitor across the 100 μm source-load coupling gap. This option was not explored in this study. It must be noted that the non-tunable transmission zero stubs are created out-of band and hence do not affect the passband.

Figure 5.20 shows the modified layout (with the open stubs) in an EM simulator to compute the modified external Q, Q_{ex}. An external Q of 16.37 is computed from the S_{21} graph plotted in Figure 5.21. At this point although Q_{ex} is not reduced to the targeted value of 11.18, the mismatch loss at the ports met the specifications (0.1 dB is $\leq$ 0.14 dB). Hence, no further modifications to the design were made to further reduce Q_{ex}.

5.3.5 Tunable Filter Response

This section analyzes the filter response while tuning. Figure 5.22 shows the S_{21} response of the complete filter layout simulated in Sonnet as the center frequency of the filter is tuned. Tunable filter passband, tunable and non-tunable transmission zeroes are highlighted. Two

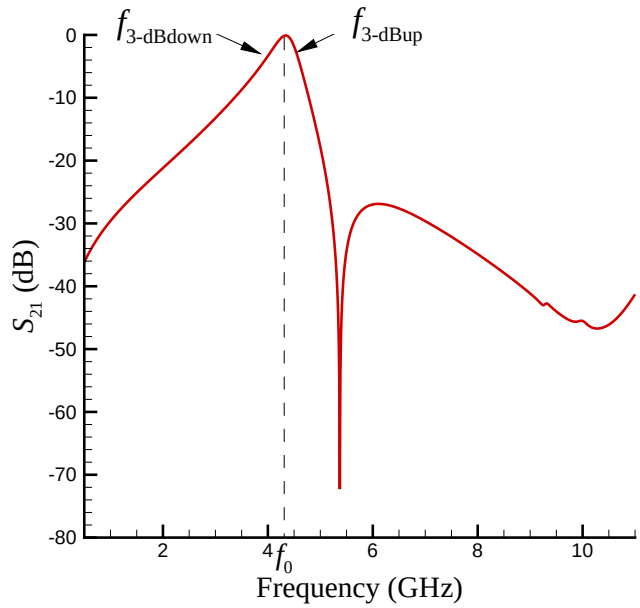

Figure 5.21: Frequency domain S_{21} plot of the layout in Figure 5.20 used to compute the modified external Q (Q_{ex}) after introducing the open-stubs on the input and output port traces.

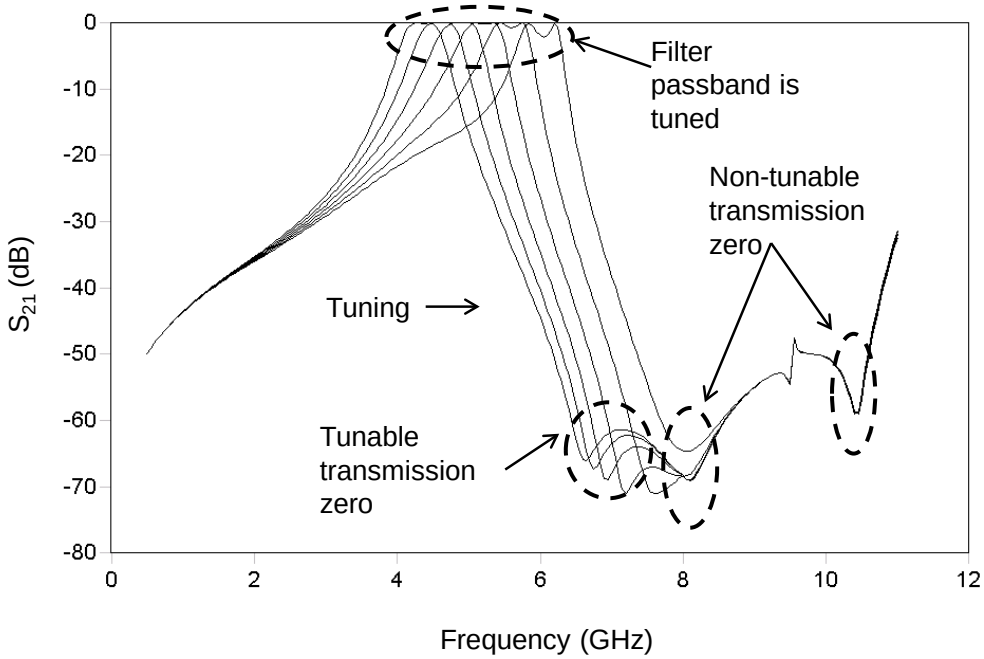

Figure 5.22: Lossless Sonnet simulation of the filter showing the filter response while tuning. A filter tunability of 38% is observed assuming a 2:1 change in capacitance value.

IDC capacitors of 2.625 pF are connected in series to form the tunable part of the resonator. The transmission line length of the resonator is 1740 um. A filter tunability of 38% is observed assuming a 2:1 change in capacitance value. Ferroelectric filters with high tunability have high insertion loss and efforts are underway to study the source of this "mysterious loss." Lossless simulations are presented in this section to get an idea of the filter performance before including the effect of loss on the filter response. The accuracy of EM results allows analyzing the response by separating lossless results from the ones including loss, in a way that can never be done with measured results where loss always accompanies the results. Filter response including loss are presented in Section 5.6.1.

5.4 Tunable Filter Response Analysis

Figure 5.22 indicates that the tunable passband and the tunable transmission zero moves to the right when the filter is tuned while the non-tunable zero does not tune. This sections analyzes the response of the filter when the BST capacitor (or filter varactor) is tuned.

5.4.1 Tunable Passband Response Analysis

Section 4.3 discusses the tunable distributed resonator that is also used in this design. Two such tunable distributed resonators are coupled together in a modified combline filter topology that includes the S-L coupling and open stubs at the input and output ports to provide a passband response as shown in Figure 5.14 at zero-bias. The tunable BST capacitor is biased by a DC voltage source during tuning. This reduces the tunable capacitance value. As explained in Chapter 4, a reduction in the varactor capacitance increases the resonant frequency of the tunable distributed resonators which causes the passband to shift to the right as shown in Figure 5.22.

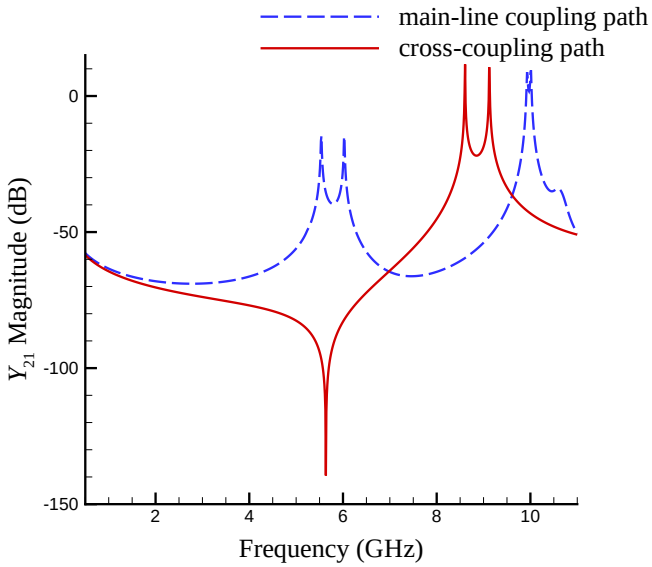

(a)

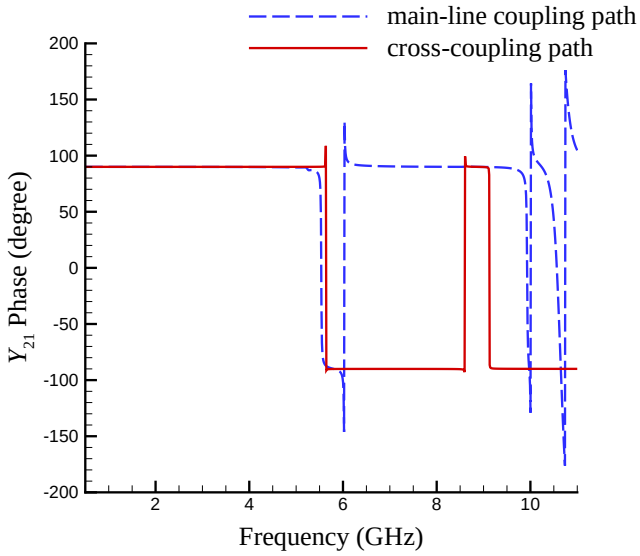

(b)

Figure 5.23: Magnitude and phase plots of Y_{21} for the two paths between input and output ports (main-line coupling path and the cross-coupling path) when the tunable capacitance is reduced to half its zero-bias value: (a) magnitude plot of Y_{21} for the main-line coupling and the cross-coupling paths when the tunable capacitance is reduced to half its zero-bias value; and (b) phase plot of Y_{21} for the main-line coupling and the cross-coupling paths when the tunable capacitance is reduced to half its zero-bias value.

5.4.2 Tunable Transmission Zero Analysis

As discussed in Section 5.3.4, a tunable transmission zero is designed using the Y-parameter method. In this section, the reason behind the tunability of these transmission zeroes as a function of frequency is explored. These zeroes are designed to be tunable so that the steepness of the filter skirt on the image side of the passband is maintained throughout the filter frequency tuning range. The tunability of the transmission zeroes can also be explained using the Y-parameter method.

The filter is tuned using ferroelectric (like BST) based capacitors. During filter tuning, the permittivity of the underlying ferroelectric material that is used as a dielectric is reduced due to an increase in the DC bias voltage. This reduces the capacitance of the tunable varactor. Figure 5.23 is the Y-parameter magnitude and phase plot of the main-line coupling path and the cross-coupling (S-L coupling) path with a tunable capacitance value that is half its value at zero-bias. A similar plot with zero-bias capacitance is plotted in Figure 5.16. Comparing Figures 5.16 and 5.23 it can be observed that the Y_{21} magnitude and phase-plot of the main-line path shifts to the right while no change is observed in the Y_{21} graphs for the cross-coupling path. As shown in Figure 5.23 at a frequency of 6.98 GHz, the magnitude of Y_{21} in the two-paths is zero while the phase of Y_{21} between the two-paths is 180° apart. This result can be compared with the result shown in Figure 5.16 where the transmission zero was located at 6.5 GHz. This indicates a shift in the tunable transmission zero to the right as the filter capacitor is tuned. The tunable capacitors that are part of the resonator structure in the main-line path are responsible for both shifting the passband response to the right as well as shifting the transmission zero to the right. This ensures the relative location of the transmission zero with respect to the upper-end of the passband is maintained throughout the tuning. In other words, the transmission zero tunes along with the passband as the filter varactor is tuned.

5.4.3 Constant Absolute Filter Bandwidth Analysis

Although the bandwidth constraint on tunable filters can be relaxed in newer broadband receiver architectures due to the advent of high analog bandwidth ADCs, some high-tunability filters can have wide variations in bandwidth that can exceed the ADC bandwidth at extremes of the tuning range. These designs benefit from maintaining a constant bandwidth to ensure that high tunability does not push the maximum bandwidth of the filter over the analog bandwidth of the system ADC. Constant absolute bandwidth is thus a useful feature for high-tunability ($\geq 30\%$) filters.

Hunter and Rhodes [25] designed a combline filter on suspended substrate stripline with tunable resonators having an electrical length of 53° as this was determined to be a length for constant absolute bandwidth. Kim and Yun [47] designed a constant bandwidth tunable microstrip based combline bandpass filter using stepped-impedance resonators. An attenuation pole near the passband, as discussed in [78, 5], creates a near constant bandwidth. Corrugated microstrip coupled lines were used to synthesize a coupling coefficient based on the corrugated finger capacitance and the length, width and gap between corrugations in a constant absolute bandwidth filter design proposed by El-Tanani and Rebeiz [79] .

In all these different methods, in order to ideally achieve zero-bandwidth change across the tuning range,

$$K \propto 1/f_0 \tag{5.9}$$

and

$$Q_{\text{ex}} \propto f_0 \tag{5.10}$$

where f_0 is the center frequency, K is the coupling coefficient, and Q_{ex} is the external Q.

The above proportionality can be proved as follows:

A relation between coupling coefficients and external Q, and low-pass prototype g-values can be represented in the form of the following equations [70].

$$K = \frac{\text{BW}}{(\sqrt{g_n \cdot g_{n+1}})f_0} \tag{5.11}$$

where $n = 1$ to $(N-1)$, N is the filter order, BW is the filter bandwidth, f_0 is the filter center frequency, and g_n, g_{n+1} are low-pass prototype g-values.

$$Q_1 = \frac{f_0(g_0 \cdot g_1)}{\text{BW}} \tag{5.12}$$

and

$$Q_N = \frac{f_0 \cdot q_N}{\text{BW}} \tag{5.13}$$

where $q_N = g_N/g_{N+1}$ for even N and $q_N = g_N \cdot g_{N+1}$ for odd N, Q_1 and Q_N are the external-Qs (i.e. Q_{ex}) at the input and output ports respectively, BW is the filter bandwidth and f_0 is the filter center frequency. Also, g_0, g_1, g_N and g_{N+1} are the low-pass prototype g-values.

From Equations (5.11), (5.12) and (5.13) it can be noted that to achieve a constant bandwidth filter, Equations (5.9) and (5.10) must both hold true. In reality, bandwidth control is typically designed within a certain tolerance factor (such as ±75 MHz). Hence, absolute bandwidth control is achieved if K decreases as the filter center frequency, f_0, increases while external coupling Q, Q_{ex}, increases as f_0 increases.

Figure 5.24 shows the plots of K and Q_{ex} as a function of center frequency before and after the open stub modifications are introduced. These plots are obtained by computing K and Q_{ex} from simulations. It can be observed that overall as the center frequency f_0 increases, K reduces. This is true both before and after the open stubs are introduced in the filter layout.

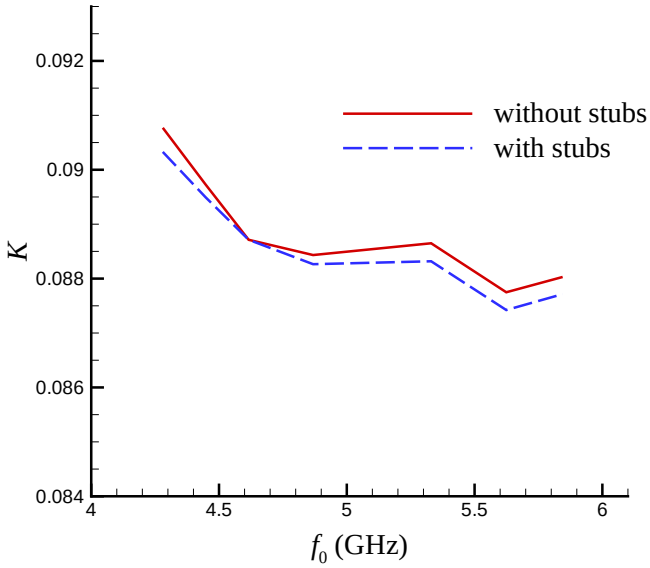

(a)

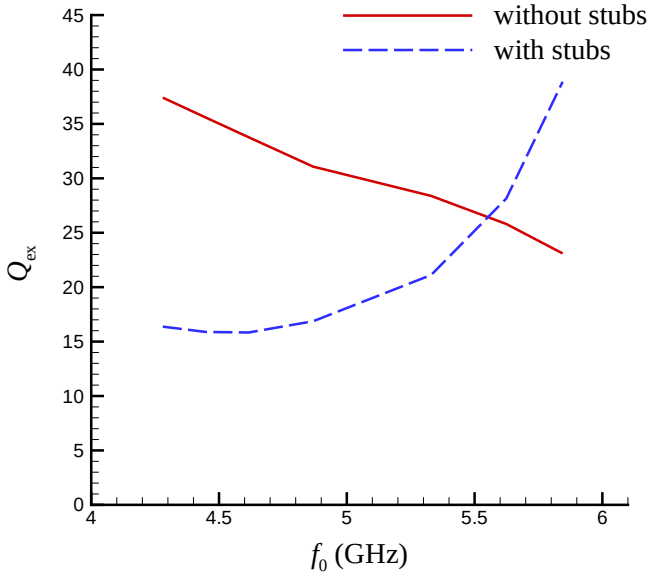

(b)

Figure 5.24: Coupling coefficient (K) and external Q (Q_{ex}) as a function of filter center frequency (f_0) before and after the introduction of the open stub to the design to achieve a constant absolute bandwidth filter: (a) K as a function of filter center frequency (f_0); (b) Q_{ex} as a function of filter center frequency (f_0).

Table 5.1: Measured filter 3-dB bandwidth as a function of center frequency.

f_0 (GHz)	3-dB bandwidth (MHz)
4.25	700
4.50	700
4.90	700
5.20	675
5.48	650
5.70	625
5.80	625

However, the variation of Q_{ex} as a function of center frequency, f_0, is altered by the introduction of the open stubs. As seen in the Figure 5.24b, Q_{ex} decreases as f_0 increases without the open stubs, while adding the stubs makes Q_{ex} increase as f_0 increases (as required for a constant filter bandwidth).

Table 5.1 shows the variation of the measured bandwidth as the center frequency of the filter is tuned. A bandwidth variation of 75 MHz is observed as the center frequency of the filter is tuned from 4.25 GHz to 5.8 GHz (36.5%).

5.5 Filter Fabrication

The filter was fabricated using an alumina substrate chosen for its low cost, the close match of its thermal coefficient of expansion to that of BST, and its low loss tangent [60, 61]. Here the alumina substrate has a thickness of 381 μm, dielectric permittivity (ϵ_r) of 9.9, and a loss tangent ($\tan\delta$) of 0.0002. The thermal expansion match prevents the BST from cracking when subjected to high heat in the annealing step. The alumina substrates were polished on both sides by Coorstek Inc, Colorado. Via holes (150 μm in diameter) were laser drilled by LPT Inc, Oregon. These vias were then filled with a gold/glass frit and cured at 900°C by Hybrid-Tek, New Jersey. Magnetron sputtering was used to deposit a 0.70 μm-thick BST film across the

wafer in a vacuum chamber for 2 hours with the following processing conditions: power density of 2.5 Watts/cm^2, deposition pressure of 10 mTorr, and deposition temperature of 300°C. After deposition, the dielectric is masked and patterned using a single layer photolithography step followed by etching using a 10% hydrofluoric solution for 2 minutes. This step was performed in order to remove BST from all areas of the substrate except where the varactors are located. The substrate was then annealed in air at 900°C for 20 hours which fully crystallized and densified the dielectric film.

Metallization of the device was performed in two steps. The initial metallization step consists of a sputtered chromium (Cr) layer followed by a layer of gold, 10 and 200 nm thick respectively. This metal stack was patterned and etched with a single layer photolithography step and ion beam etched. The patterns for this initial metallization consists of the interdigitated capacitors and the biasing lines. The bottom layer substrate metallization also consists of a Cr/Au metal stack providing a seed layer for the electroplating step. The second metallization step built up the rest of the circuit: the resonators; the input and output feed-line paths with open stubs; and the resistor pads. The metal stack from this step was patterned using single layer lithography which was then followed by a 450 nm thick silver film deposited by magnetron sputtering and patterned by liftoff. Finally the device was electroplated with copper up to a total thickness of 5 μm. The IDC fingers are masked with a photoresist layer before the electroplating step was performed to prevent shorting between the fingers. It should be noted that the entire device was plated except for the immediate region of the varactors [60].

A photograph of the fabricated two-pole modified combline bandpass filter is shown in Figure 5.25. Two back-to-back BST IDCs are connected in series with the transmission line which is shorted through a via to the ground plane (metallized bottom layer of the substrate) to form tunable resonators. A zoomed-in version of the tunable capacitor is shown in the inset in Figure 5.25. The IDC fingers are separated by a 3 μm gap.

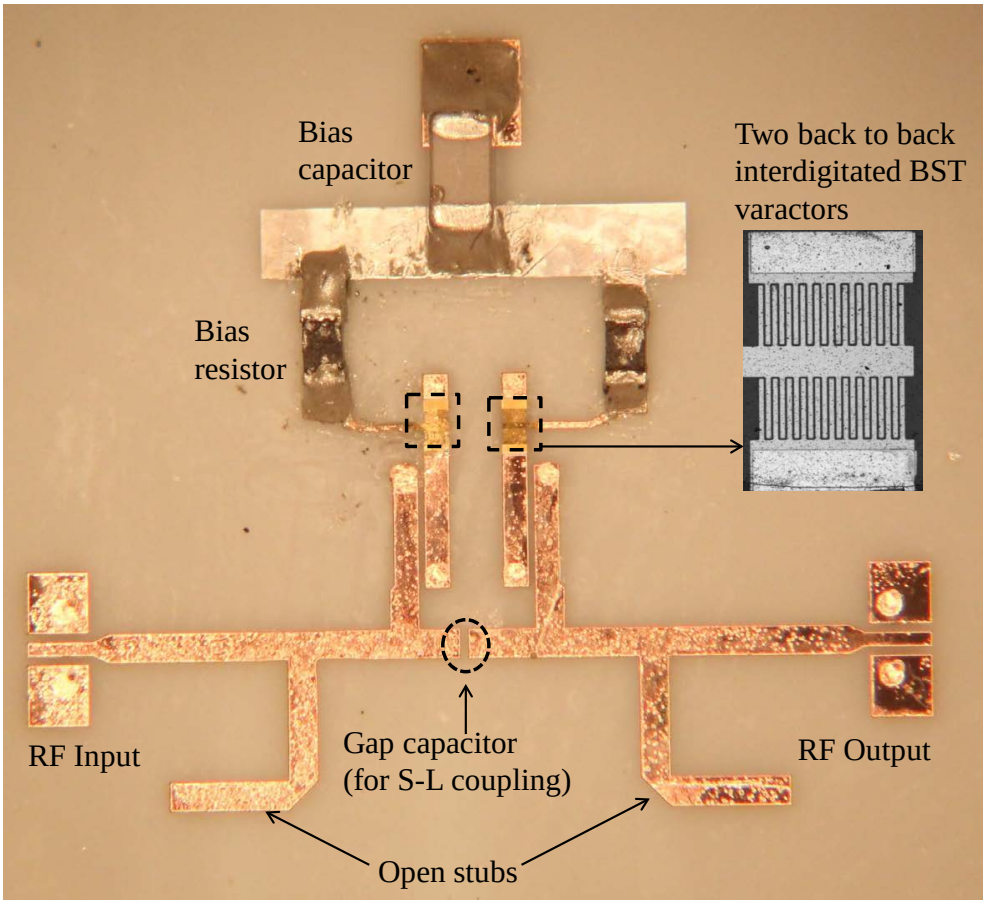

Figure 5.25: A photograph of the fabricated two-pole modified combline bandpass filter on an alumina substrate with a zoomed in view of the interdigitated BST capacitor.

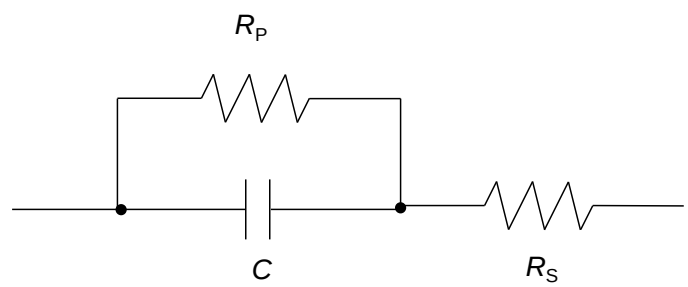

Figure 5.26: Equivalent circuit of the BST varactor. R_P can be ignored at higher frequencies as the dielectric loss is negligible and conductor loss significantly dominates at higher frequencies.

5.6 Results

5.6.1 Simulated Results

As discussed in Section 5.3, CST MWS and Sonnet EM simulators have been used to design the filter. All EM simulations so far are lossless. A final simulation result using Sonnet that includes losses will be discussed in this section.

Hybrid EM simulation (EM-circuit co-simulation) of the complete filter circuit was performed. An alumina substrate with a dielectric permittivity (ϵ_r) of 9.9, thickness of 381 μm, and a loss tangent ($\tan\delta$) of 0.0002 was considered in the simulation. The integrated BST capacitors were treated as lumped elements and were simulated together with the rest of the microstrip filter layout. This was done to reduce the simulation time without trading off the accuracy of the results.

The equivalent circuit of the BST varactor is shown in Figure 5.26 [80, 81]. The total varactor Q-factor can be approximately expressed as a parallel combination of dielectric Q-factor (Q_{BST}) and conductor Q-factor ($Q_{\mathrm{conductor}}$):

$$\frac{1}{Q_{\mathrm{total}}} = \frac{1}{Q_{\mathrm{BST}}} + \frac{1}{Q_{\mathrm{conductor}}} \tag{5.14}$$

where $Q_{\mathrm{BST}} = 1/\tan\delta = \omega R_P C$ and $Q_{\mathrm{conductor}} = 1/(\omega R_S C)$. Here ω is the frequency in

radians, and R_P and R_S are the parallel and series resistances in the equivalent model of the BST capacitor as shown in Figure 5.26.

A low frequency electrical characterization of the BST film for the fabricated filter yields a $\tan\delta = 0.0135$ (with a tolerance of +/-0.0005) and a capacitance of 2.625 pF (with a tolerance of +/-0.055 pF) for the four individual capacitors on the resonators (two of the capacitors are connected in series with each resonator). R_P can then be calculated using the equation for Q_{BST}. The data was recorded using an HP4192 impedance analyzer and a probe station. The data assumes a parallel G-C admittance model. Based on the results in [81], it can be concluded that at lower frequency both Q_{BST} and $Q_{\mathrm{conductor}}$ contribute to Q_{total}. The dielectric loss contribution to the total Q-factor is negligible beyond 300 MHz and the conductor loss significantly contributes to the total Q-factor at higher frequencies. R_P can thus be ignored in the simulations at the filter passband frequencies discussed here.

Several filters with the two-pole topology discussed were fabricated and measured at microwave frequencies. The loss of these filters can be approximately represented by a 2.0 Ω equivalent resistance in series with the lossless tunable resonator. Full-wave Sonnet EM simulations discussed in Chapter 6 suggest that the ferroelectric capacitor is the predominant source of loss in these filters. These results confirm the existence of an equivalent series resistance of 2.0 Ω associated with the lossless tunable resonator, 1.4 Ω of which is associated with the tunable capacitor. This series resistance of 1.4 Ω is used to represent conductive loss in the lumped model for the BST capacitor used in the simulations. The actual conductivity of the metals and the vias are included to account for losses in the rest of the filter layout.

The 3D EM simulation result for the filter including loss is presented in Figure 5.27 for a BST IDC capacitance tuning ratio of 2:1. The tunable and non-tunable zeroes are highlighted in Figure 5.27a. Loss accounts for higher insertion loss, lower return loss and rounding of the transmission zeroes. Parasitic coupling and interaction of the different filter sub-blocks is captured in the EM simulations.

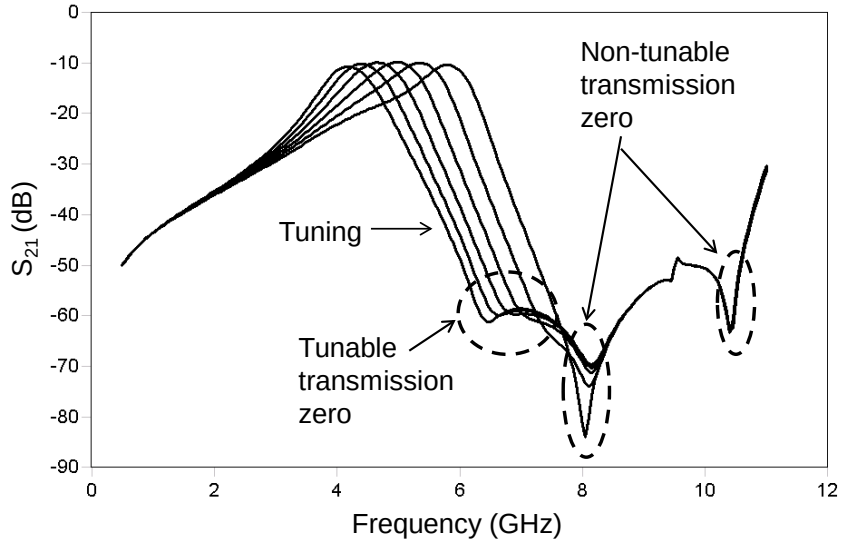

(a)

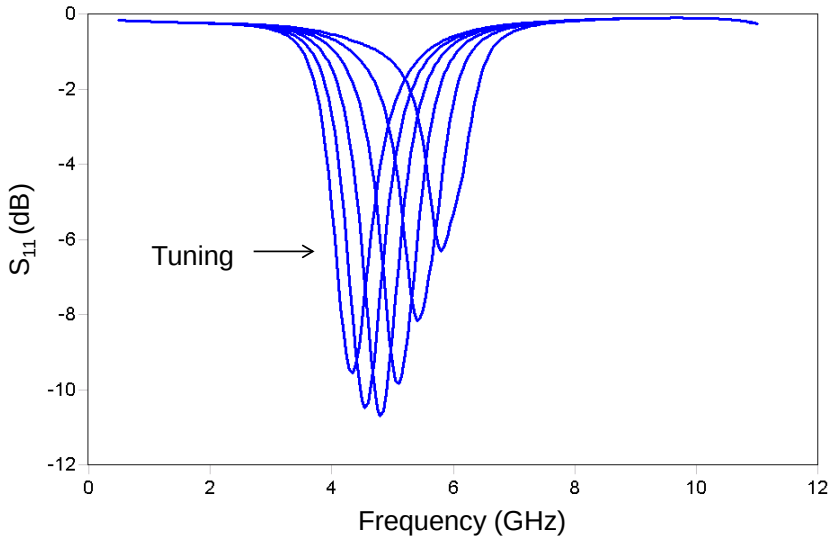

(b)

Figure 5.27: Simulated S-parameter results including loss: (a) simulated S_{21}; and (b) simulated S_{11} of the tunable BST filter covering 3.83 GHz to 6.10 GHz, and with center frequency tuning from 4.20 GHz to 5.80 GHz. An insertion loss of 10.70 dB and a 3-dB bandwidth of 0.73 GHz corresponds to the center frequency of 4.20 GHz. An insertion loss of 10.34 dB and a 3-dB bandwidth of 0.70 GHz corresponds to the center frequency of 5.80 GHz.

Table 5.2: Comparison of measured and simulated insertion loss (IL) results.

Measured			Simulated		
Frequency (GHz)	IL (dB)	3-dB Bandwidth (MHz)	Frequency (GHz)	IL (dB)	3-dB Bandwidth (MHz)
4.25	10.29	700	4.20	10.70	725
4.50	9.09	700	4.40	10.24	750
4.90	8.25	700	4.65	9.96	750
5.20	7.95	675	5.0	9.86	825
5.48	8.08	650	5.35	9.96	800
5.8	8.60	625	5.8	10.34	700

5.6.2 Measured Results

Microwave measurements used an Agilent microwave network analyzer (PNA N5230A), 250 μm pitch Ground-Signal-Ground (GSG) probes, short-open-load-thru (SOLT) calibration, and a DC bias voltage source (HP 4142B). The BST capacitors on the two resonators were tuned simultaneously by a single DC bias voltage. The S-parameters were measured over the DC bias voltage range of 0 V to 110 V as shown in the filter tuning graphs in Figures 5.28a and 5.28b. The measured filter response indicates a center frequency that can be tuned from 4.25 GHz to 5.80 GHz (36.5% tuning) with 3-dB bandwidth range of 625 MHz to 700 MHz. The insertion loss is the highest at 0 V (10.29 dB), it decreases to a minimum of 7.95 dB at a bias voltage of 60 V before increasing slightly to 8.60 dB at 110 V.

Fixed frequency and tunable transmission zeroes are identified in Figures 5.28. There is a close match between the simulated and measured results in terms of the performance parameters, the locations of transmission zeroes, and stopband and passband shape.

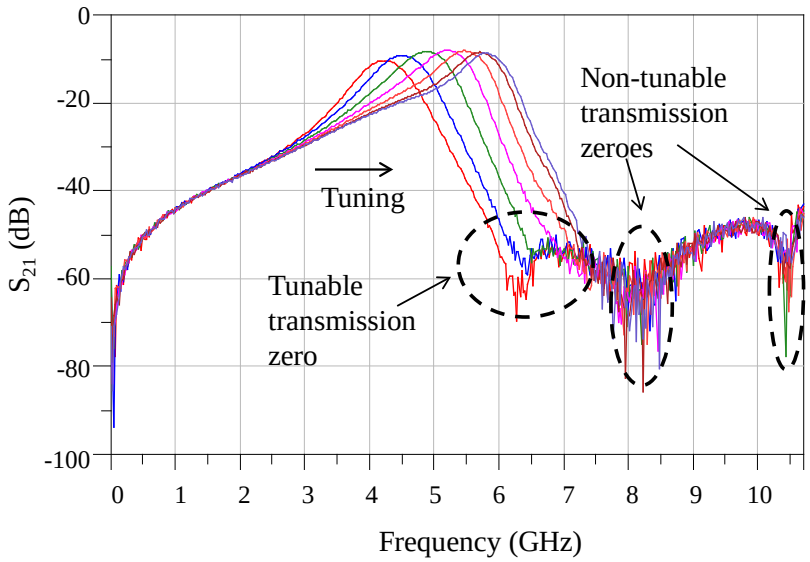

(a)

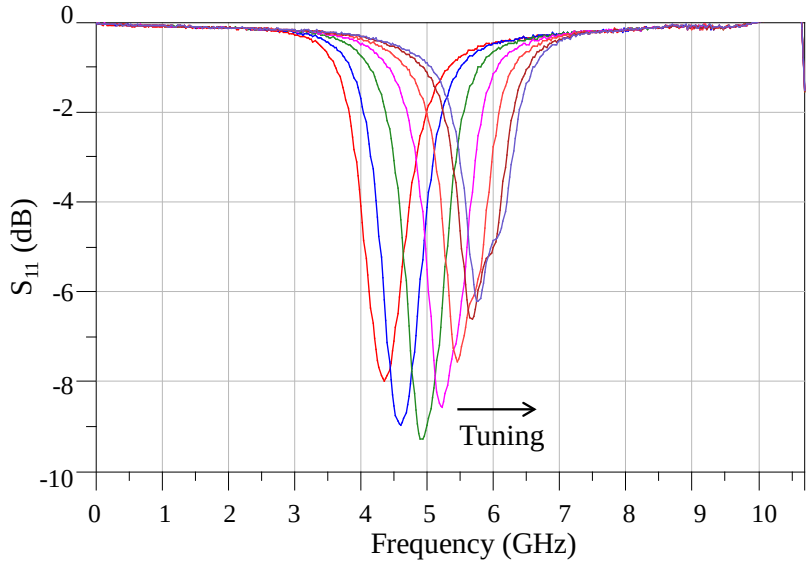

(b)

Figure 5.28: Measured S-parameter results: (a) measured S_{21} of a tunable BST filter covering 3.88 GHz to 6.10 GHz at bias voltages of 0 V, 20 V, 40 V, 60 V, 80 V, 100 V and 110 V. At 0 V dc bias voltage, the center frequency is 4.25 GHz, insertion loss is 10.29 dB, and the 3-dB bandwidth is 0.70 GHz. At 60 V dc bias voltage the center frequency is 5.20 GHz, insertion loss is 7.95 dB and the 3-dB bandwidth is 0.68 GHz. At 110 V dc bias voltage the center frequency is 5.80 GHz, insertion loss is 8.60 dB and the 3-dB bandwidth is 0.63 GHz; and (b) measured S_{11} of a tunable BST filter covering 3.88 GHz to 6.10 GHz at bias voltages of 0 V, 20 V, 40 V, 60 V, 80 V, 100 V, and 110 V.

Table 5.3: Comparison of measured and simulated return loss (RL) results.

Measured		Simulated	
Frequency (GHz)	RL (dB)	Frequency (GHz)	RL (dB)
4.35	7.98	4.35	9.56
4.60	8.96	4.55	10.48
4.93	9.30	4.8	10.7
5.23	8.56	5.1	9.85
5.45	7.55	5.4	8.16
5.75	6.21	5.8	6.31

5.7 Discussion

Tables 5.2 and 5.3 compare the measured and simulated filter tuning results. In measurements, the capacitance is tuned by varying the DC bias voltage to change the BST dielectric permittivity but similar simulations that vary the BST permittivity would be very time intensive. Hence in simulations, the equivalent lumped model of the capacitance is used and the capacitance value is tuned such that a typical 2:1 capacitance variation is considered. The results can be compared as both techniques essentially change the tunable capacitance value.

The high filter insertion loss can be attributed to the low overall unloaded Q of the tunable resonators. In order to achieve high tunability the filter resonators were designed with large tunable capacitor values. However, the filter insertion loss associated with such resonators is higher than when the resonator is designed with a lower capacitor value for the same frequency of operation and similar processing conditions [14, 3].

The measured response of the filter shows a maximum 3-dB bandwidth of 700 MHz which is appreciably lower than the maximum allowable specification of 1 GHz for the filter. The filter can be redesigned with a higher maximum bandwidth of 1 GHz to reduce the filter insertion loss.

This design provides an added advantage to tunable filters requiring near constant bandwidth. Usually bandwidth control in combline-based topologies is obtained by restricting the

transmission line in the tunable resonator such that its electrical length is 53° at the center of the tuning range [25]. In the design presented in this paper the topology of the circuit restricts the bandwidth, thereby removing the restriction on the electrical length of the transmission lines (or value of tunable capacitance). The initial design location of the tunable resonators can hence be designed for other electrical lengths [14] while still maintaining a constant bandwidth during tuning.

The number of analog-to-digital converter (ADC) bits currently available (12–13 bits for 1 GHz bandwidth) is not sufficient to achieve the high dynamic range required by newer wide-band receivers without the use of filters. Bandpass filters placed before the ADCs in these systems provide an additional increase in dynamic range through out-of-band rejection and steep filter skirt selectivity. The measured tunable filter response indicates a high out-of-band rejection level of greater than 35 dB throughout the wide stopband frequency range. An out-of-band rejection level of greater than 42 dB is observed in the close vicinity of the tunable transmission zero realizing a steep filter skirt on the upper side of the passband for image rejection.

5.8 Comparison With Published Filters

Table 5.4 compares the two-pole BST-based filter discussed in this chapter with other published ferroelectric-based bandpass filters. Key performance parameters along with a figure of merit, FOM, are tabulated. The FOM as discussed in Section 4.4.1 and defined in [20] is well suited for comparing stand alone tunable filters. In Table 5.4 the columns V_1 and V_2 represent the parameter values at zero and the maximum dc bias voltages used to tune the filters. The data for the table was obtained from graphs plotted in the published papers whenever specific data was unavailable in the text.

Comparing different ferroelectric tunable filters involves using the FOM numbers as a general quality indicator while also considering the relative priority (degree of importance) attributed to the performance parameters to best match a filter for a specific application. As an example,

if the application necessitates a wideband tunable filter, the tunability parameter must be given adequate weighting in addition to the calculated FOM.

Considering all the parameters tabulated, the filter's quality compares well with the other work reported in Table 5.4 while achieving higher tunability, constant bandwidth, steep filter-skirt selectivity on the image signal side of the passband and wide stopband frequency range.

Table 5.4: Comparison of Filter Discussed in this Chapter with Published Electronically Tunable Ferroelectric Microwave Bandpass Filters (res. = resonator, cap. = capacitor, RT = room temperature, FOM = figure of merit — high is good).

Reference	Tunable component, substrate, temp. of operation	Filter type	Top conductor of filter	Center freq. (GHz)		Bandwidth (GHz)		Insertion loss (dB)		Tuna-bility, (%, GHz)	Max. BW variation (GHz)	FOM (1/db) [20]
				at V_1	at V_2	at V_1	at V_2	at V_1	at V_2			
Haridasan this filter	IDC BST cap., Alumina, RT	2-pole	Cu	4.25	5.80	0.70	0.63	10.29	8.60	36.47%, 1.55	0.07	0.25
Su 2008 [17]	YBCO/BST cap., MgO, 77 K	3-pole	YBCO	3.50	3.68	0.20	0.25	6.00	1.40	5.14%, 0.18	0.05	0.28
Courrèges 2009 [21]	BST Gap cap., Sapphire, RT	2-pole	Cu	10.04	10.78	0.81	0.87	2.75	2.20	7.37%, 0.74	0.06	0.36
Subramanyam 2000 [4]	YBCO/STO res., LAO, 77 K	2-pole	YBCO	17.40	19.10	1.50	1.20	5.00	2.20	9.77%, 1.70	0.30	0.38
Subramanyam 2000 [4]	Au/STO res., LAO, 77 K	2-pole	Au	18.10	19.00	1.40	1.50	6.00	7.00	4.97%, 0.90	0.10	0.10
Pleskachev 2004 [20]	Gap STO cap., Alumina, 77 K	2-pole	Cu	5.11	5.48	0.35	0.36	7.00	5.20	7.24%, 0.37	0.01	0.17
Sigman 2008 [18]	IDC BST cap., Alumina, RT	3-pole	Cu	8.75	10.96	1.60	1.80	8.00	4.00	25.26%, 2.21	0.20	0.23
Sigman 2008 [18]	IDC BST cap., Alumina, RT	3-pole	Cu	11.70	14.30	1.60	1.70	10.0	6.00	22.22%, 2.60	0.10	0.20
Nath 2005 [19]	IDC BST cap., Sapphire, RT	3-pole	Cu	2.44	2.88	0.60	0.80	5.10	3.30	18.03%, 0.44	0.20	0.15
Tan 2006 [16]	Gap BST cap., LAO, 77 K	3-pole	YBCO	11.74	11.93	0.52	0.55	1.60	0.35	1.62%, 0.19	0.03	0.47

5.9 Conclusion

A pseudo-elliptic (or quasi-elliptic) asymmetric response filter was designed to meet the specifications of a tunable filter block that is part of a wideband transceiver system. This chapter focussed on the filter design, fabrication, simulated and measured results, and a discussion of the filter response observed. In-depth analysis of the tunable response such as center frequency tunability, transmission zero tunability and constant absolute bandwidth control during tuning were provided.

Although a filter using the traditional combline filter topology has excellent stop-band rejection, the bandwidth of the filter varies widely as the tuning range of the filter increases and additional resonators are required to achieve a steeper passband selectivity. In this design, the traditional combline filter topology was modified to realize tighter bandwidth control and to achieve steeper filter slopes without the use of additional in-band filter resonators that also increase loss.

If the resonator lines of the traditional combline filter were $\lambda/8$ long at the primary passband, the second passband would be centered around four times the midband frequency ($4f_0$) of the first passband. However, once the modifications to the combline filter are made, the stopband rejection is not good as is seen in the design discussed in this chapter. While source-load (S-L) cross-coupling modification to the combline filter added a transmission zero to the upper passband it worsened the stopband rejection above the passband. The open stubs introduced into the design improved the stop-band rejection by introducing non-tunable transmission zeroes, created a constant bandwidth filter, and increased the impedance matching at the input and output ports of the filter. The non-tunable transmission zeroes also pushed the center frequency of the first spurious passband to $2.6f_0$. The location of the non-tunable transmission zero can be varied by altering the spacing of the S-L coupling gap or adding BST under the S-L gap that could then be tuned. This option could further push the spurious response to the right and widen the stop-band rejection.

The 3-dB edge-to-edge operating bandwidth of the filter is 2.22 GHz (or 0.65 octaves). The

topology of the filter lends itself to maintaining a constant bandwidth in the tuning range. This contrasts with traditional tunable resonator based combline filter designs were the electrical length of the transmission line (and hence the tunability) is restricted. The filter presented exhibits high tunability, constant absolute bandwidth in the entire tuning range, steep filter skirt selectivity on the upper side of the passband and wide-stopband rejection.

The lossy simulations predicted the measured results within reasonable tolerance. The simulated filter tuning results assumed a constant value of series resistance in the lumped BST capacitor model. Based on several measured results for two-pole and three-pole designs, it can be concluded that the insertion loss changes as the filter tunes. This means that the series resistance should correspondingly vary as the filter tunes. A more enhanced but time intensive simulation that would vary the dielectric permittivity of the BST would provide a better match with the measured tuning result. This simulated result could then be compared with the lumped model to provide a different series resistance as the center frequency shifts.

The zero-bias center frequency of the filter was slightly off from the specified frequency due to the variation in the value of the fabricated tunable capacitors and the length of the resonator transmission lines. Compared with the lossless simulated results a significant reduction in the return loss is observed both in the measured results and the simulated results that incorporated loss. This suggests that the mismatch at the input and output ports is directly affected by resonator loss (usually only insertion loss is directly influenced by resonator losses). Both the return loss and insertion loss can be improved further by increasing the unloaded-Q of the resonators. In this design, introducing open stubs reduced the external Q (Q_{ex}) of the resonators from 37.41 to 16.37 without violating the inter-metal trace constraint (filter processing limitation). Design modifications that further reduce the external Q to the targeted value of 11.18 can be explored in the future to improve the return loss of the filter.

The overall performance of the filter designed compared well with other published tunable ferroelectric filter designs. Based on the performance data from several published ferroelectric filters tabulated in Table 5.4, it can be observed that in these filters a tunability of $\geq 20\%$ is

associated with higher insertion loss. The source of this loss is unknown at this time although some theories have been cited in published literature. Chapter 6 attempts to delve deeper into the origins of this high insertion loss associated with ferroelectric filters.

Chapter 6

Investigating The Loss Origins Of The Ferroelectric Filter

6.1 Introduction

The measured results of the two-pole modified combline filter discussed in Chapter 5 has a wide tuning range (36.5% tuning) and constant bandwidth (bandwidth variation across the tuning range is 75 MHz) but the insertion loss is around 3.5 dB higher than the value desired for practical applications in tunable transceivers. This chapter investigates the sources of loss in the ferroelectric filter in order to find ways to reduce the insertion loss in future designs, thereby improving the performance of the filter. Although this study investigates loss origins in the two-pole design, the results obtained could be leveraged to reduce loss in the three-pole filter design discussed in Chapter 4 as well.

High insertion loss in ferroelectric filters is currently hindering the widespread deployment of these filters in tunable RF/microwave applications. This chapter delves into modeling a BST capacitor and filter layout using electromagnetic simulators in an effort to seek the origins of the "mystery" loss that especially accompanies ferroelectric filters with high tunability.

6.2 Electromagnetic Simulation Of the Entire Two-Pole Modified Combline Ferroelectric Filter

Electromagnetic (EM) analysis of the filter was discussed in Section 5.3 where a lumped-BST capacitor model was used for the most part with a brief mention of the results using EM simulation of the entire filter (i.e. including the EM simulations of the BST capacitor layout). A more detailed discussion of the EM simulation of the filter is undertaken here to get a deeper insight into the possible causes for the high loss. For the reasons discussed in Chapter 5 (i.e. in short memory constraints using CST), Sonnet is used over CST MWS to perform EM simulation on the entire filter layout including the high-permittivity BST capacitor layout regions.

Simulating the entire filter layout with regions of high-permittivity dielectric like BST and a wide variation in layout dimensions and spacings is very memory intensive and cannot be handled by the current EM simulation software environment. EM analysis of the two-pole modified combline filter is thus undertaken in Sonnet by simulating the barium strontium titanate (BST) inter-digitated capacitors separately from the rest of the filter-layout and then integrating them together using a top-level netlist file. Figure 6.1 is a photograph of the entire filter. It demarcates (using the dashed elliptical shaped loop) the BST capacitor section of the filter that is simulated separately from the rest of the layout.

6.2.1 BST Capacitor EM Modeling

It has traditionally been a challenge to model the electromagnetic field distributions in a planar capacitor on a thin-film high-permittvity material like BST. The small-gap dimensions of the capacitor (2-4 μm), thin-film BST layer (0.5-0.9 μm) and large planar dimensions of the capacitor (500-700 μm) are difficult to mesh at the same time. In addition, the high contrast between the permittivity of the BST and of air make it challenging to mesh. The recent increase in availability and reduced cost of high-GB RAM ($\geq$ 12 GB), multi-core computers, along with tremendous enhancements in the newer versions of EM simulation software that take advantage

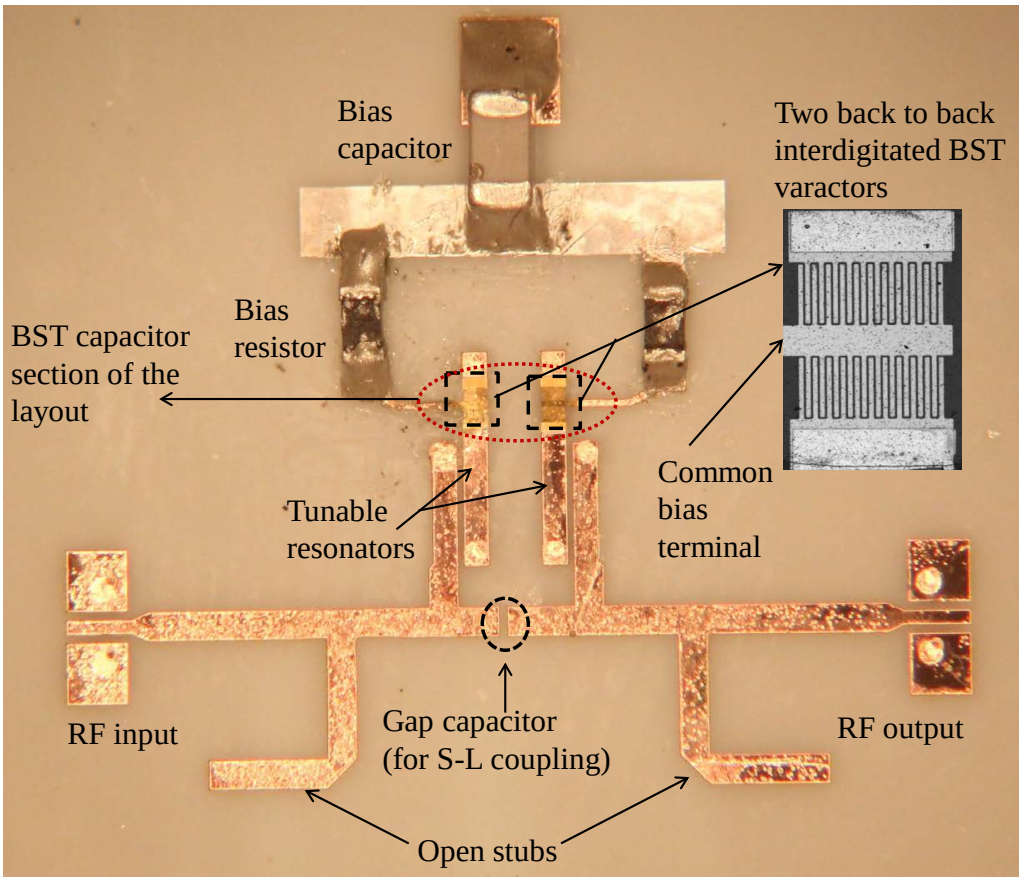

Figure 6.1: A photograph of the fabricated two-pole modified combline bandpass filter on an alumina substrate with a zoomed in view of the interdigitated BST capacitor. The BST capacitor section of the layout identified in the photograph is simulated separately from the rest of the filter layout.

Table 6.1: BST capacitor layout substrate details. A pictorial representation is shown in Figure 6.3.

Relative layer location	Dielectric material	Thickness μm	ϵ_r	$\tan\delta$
Top	BST	0.7	500	0.013
Bottom	Alumina	381	9.9	2.0e-4

Table 6.2: BST capacitor layout metallization details. A pictorial representation is shown in Figure 6.4.

Relative layer location	Metal type	Thickness μm	Conductivity S/m
Top	Gold	0.2	4.09e7
Bottom	Chromium	0.01	3.95e6

of the improved computer hardware have brought a resolution to this long-standing problem. In this section, BST capacitor EM modeling using a high-performance computer (4-core machine, 12 GB RAM) with Sonnet (version 13.52) will be discussed. The electric coupling between the two BST capacitors on each resonator will also be captured using these simulations, enabling a simulation closer to reality.

Layout of the two side-by-side BST capacitor sets is shown in Figure 6.2. Each capacitor set comprises two back-to-back series interdigitated capacitors as shown in the inset in Figure 6.1. The common bias terminal for the two-series capacitors makes the BST capacitor set a three-terminal device. Each set makes up the tunable part of a resonator depicted in Figure 6.1. The trace-lengths that are connected to the ports in Figure 6.2 are longer than the actual capacitor layout traces. Hence, reference planes are used to de-embed the lengths of traces that are not part of the layout.

Details of the mixed-dielectric substrate stack are provided in Table 6.1. A pictorial representation of the mixed-dielectric substrate stack can be seen in Figure 6.3 . A cell size of 3 μm x 3 μm is used with bi-layer metallization of chromium (Cr) and gold (Au) as it is the

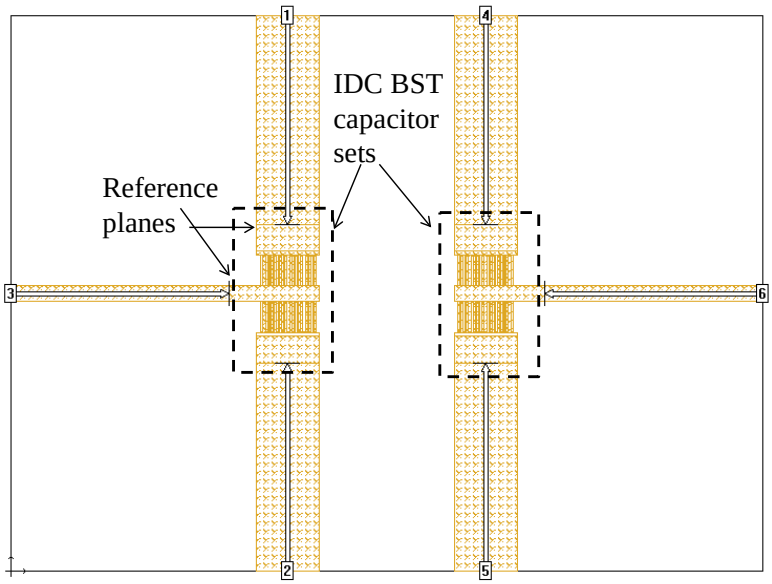

(a)

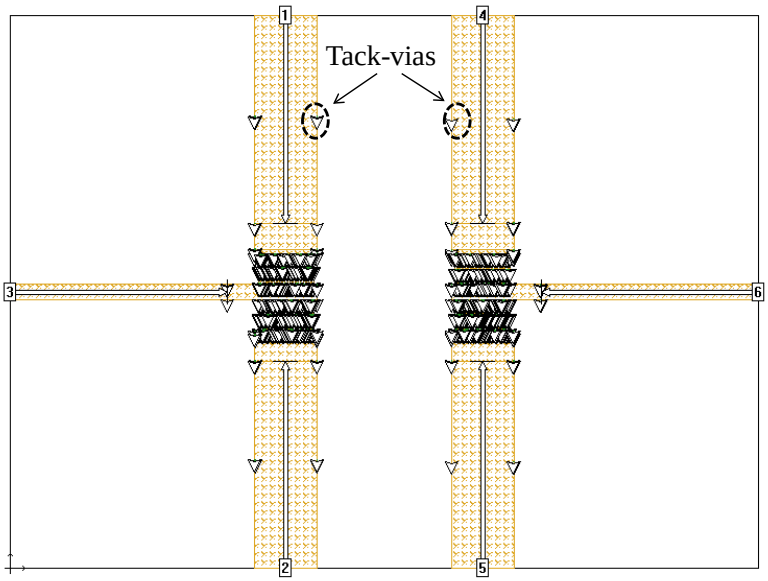

(b)

Figure 6.2: Layout of two side-by-side BST capacitor sets. Each capacitor set is part of a resonator in the two-pole filter: (a) layout of two side-by-side BST capacitor sets without the presence of tack-vias that hold the bi-layer metallizations together. The layout underneath the tack-vias is very difficult to visualize and hence the tack-vias have been removed to show the actual IDC finger layout underneath; and (b) layout of the two side-by-side BST capacitor sets with the tack-vias that connect the bi-layer metal stack together. There are many tack-vias in the interdigitated-capacitor section to ensure that loss is appropriately captured in this high-electric field strength region.

Figure 6.3: BST capacitor substrate stack.

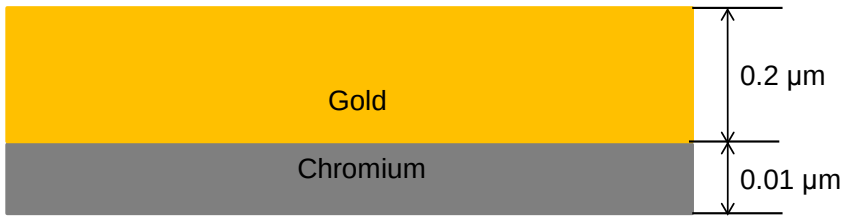

Figure 6.4: BST capacitor metal stack.

highest resolution that can model the BST capacitors with the current hardware setup. The metallization details are provided in Table 6.2. A pictorial representation of the bi-layer metal stack can be seen in Figure 6.4. Small tack-vias are placed between the two-metal layers (Cr and Au) to ensure electrical connectivity between the layers in the EM simulator. It must be noted that the tack-vias are required only by the EM simulator and are not physically present in a fabricated BST capacitor. The two metal layers connected with the tack-vias are used to emulate the bi-layer metal stack in the fabricated BST capacitor.

6.2.2 Filter Layout EM Modeling

Filter layout EM modeling includes the entire layout of the filter excluding the BST capacitor regions marked with a dashed elliptical loop in Figure 6.1. The filter layout thus includes the transmission line sections of the resonator, the RF input and output sections, vias and the DC bias sections of the BST capacitor. The coplanar waveguide (CPW) to microstrip transition sections are included in this simulation for completeness of the circuit although they do not introduce any significant difference (≤ 0.1 dB) in the simulated results. A 20 pF capacitor and

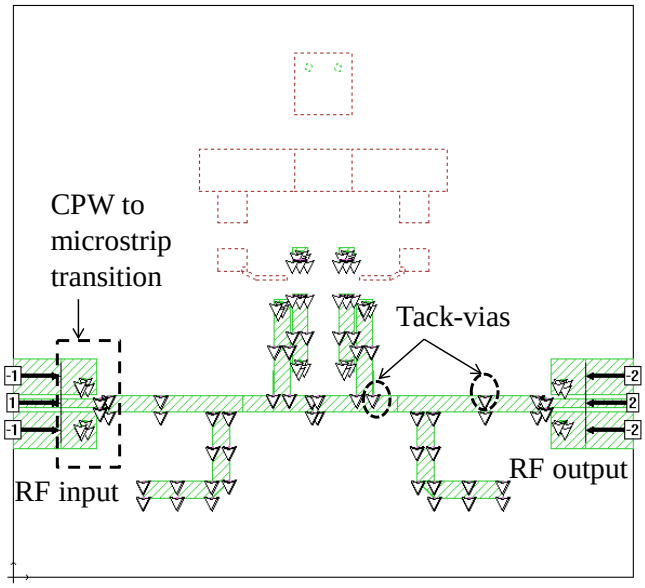

(a)

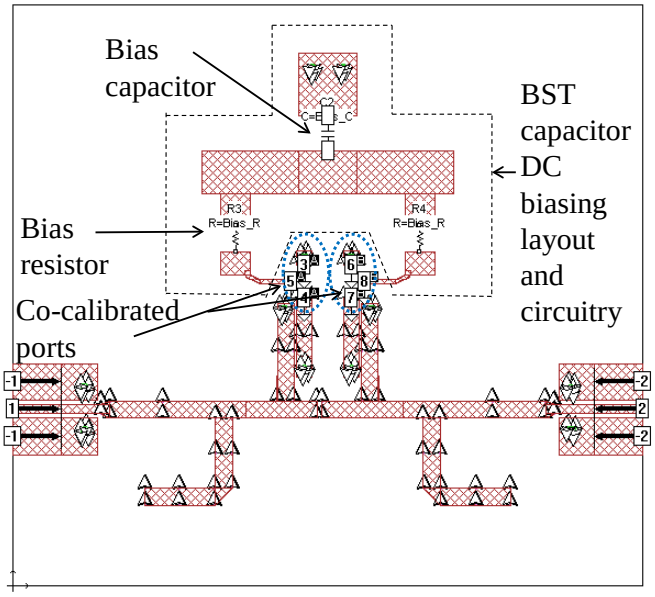

(b)

Figure 6.5: Layout of filter excluding the BST capacitor section. There are two metal layers with tack-vias between the two layers: (a) top metal-layer filter layout ; and (b) bottom metal-layer filter layout. Only the bottom-layer metallization is used for connecting the bias capacitor and resistor chips. This increases the resistance of these traces. A more resistive trace will increase the isolation between DC and RF circuitry.

Table 6.3: Filter layout substrate details.

Relative layer location	Dielectric material	Thickness μm	ϵ_r	$\tan\delta$
-	Alumina	381	9.9	2.0e-4

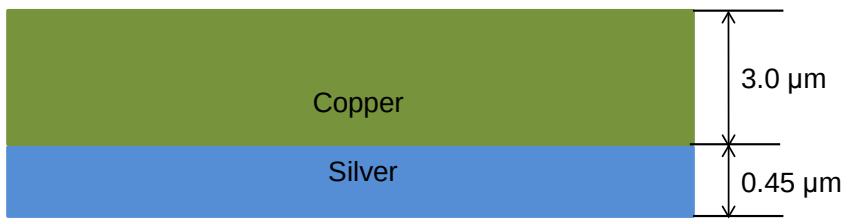

Figure 6.6: Filter metal stack.

two 15 kΩ resistors representing the bias circuitry chip capacitor and resistors respectively are included as lumped components in the model. Two groups of co-calibrated ports were added to the filter layout to include the BST capacitor model at a later time using a top-level netlist file. Co-calibrated ports are specific to the Sonnet EM simulator. They are ports used inside a circuit in Sonnet to connect another element external to the the circuit at a later time [59]. These ports are part of a calibration group with a common ground node connection. When EM analysis is performed using Sonnet each co-calibrated port within the same group is de-embedded.

Substrate details for the filter layout are provided in Table 6.3. Bi-layer silver (Ag)/ copper (Cu) metallization in the filter layout is incorporated into the model along with their

Table 6.4: Filter layout metallization details. A pictorial representation is shown in Figure 6.6.

Via/Metal	Relative layer location	Metal type	Thickness μm	Conductivity S/m
Metal	Top	Copper	3.0	2.9e7
Metal	Bottom	Silver	0.45	6.17e7
Via	-	Gold-Glass Frit	-	1.868e5

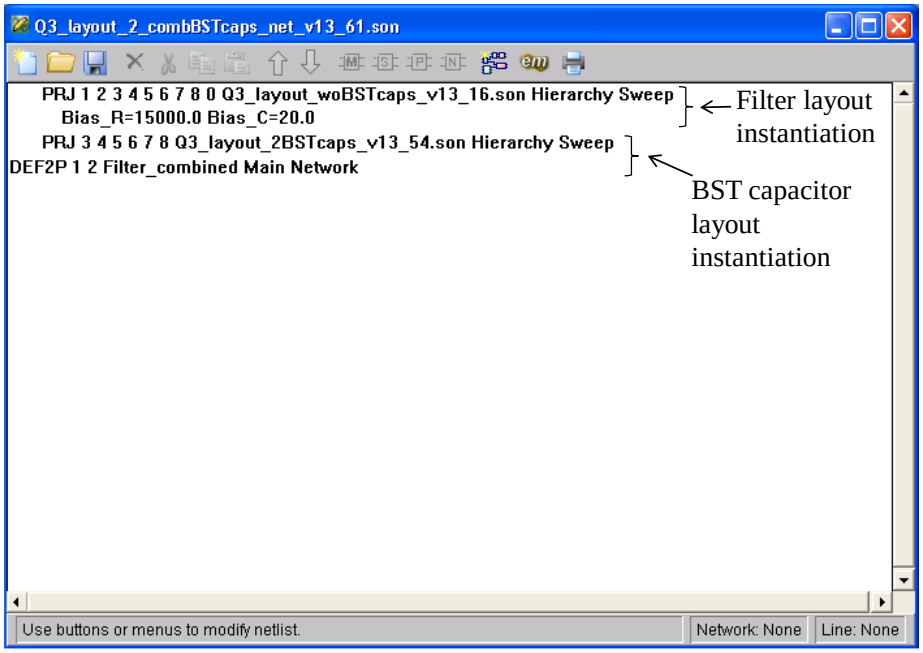

Figure 6.7: A top-level netlist file that instantiates the filter and the BST capacitor EM models to realize the complete EM simulation of a two-pole modified combline tunable filter.

measured conductivities. Sonnet version 13.52 enables via conductivity to be entered in addition to the metal conductivities. The via is filled by Hybrid-tek and the conductivity values obtained based on their data sheet is used. Table 6.4 lists the conductivities of all the metallizations (including via) used. A pictorial representation of the bi-layer metal stack can be seen in Figure 6.6. Filter cell size resolution of 20 μm x 20 μm is chosen as it is the highest resolution that can model the filter layout with the current hardware setup. As in the BST capacitor layout, tack-vias were placed between the two metal traces (Ag and Cu) to ensure connectivity between them. Ag metal trace with a thickness of 0.45 μm without an overlaying Cu metal trace was used for connecting the bias capacitor and resistor chips as a higher resistance value of these traces increases decoupling between the DC and RF circuitry.

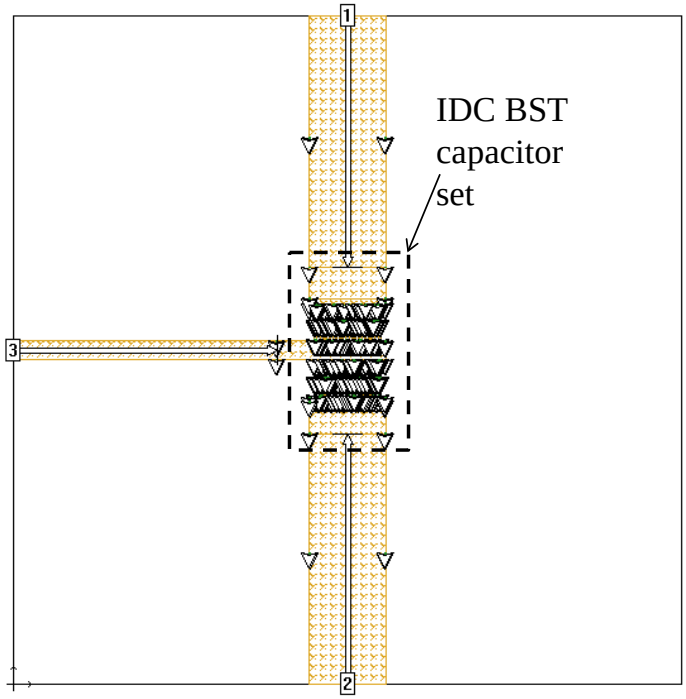

Figure 6.8: Layout of a single BST capacitor set is shown. Two instantiations of the single BST capacitor set (one for each resonator) are required in the netlist file for the two-pole modified combline filter. In other words, two instances for the BST capacitor layout are required in place of one shown in Figure 6.7.

6.2.3 Top Level Netlist

A top level netlist file shown in Figure 6.7 instantiates and seamlessly connects the EM models of both the BST capacitor and filter layout so that the results of the complete EM simulation of a two-pole modified combline tunable BST based bandpass filter can be realized and studied.

6.3 Simulation Results

Figure 6.9 compares two simulation results with the measured result. For one of the simulation results (Sim A) a single BST capacitor set as shown in Figure 6.8 is used while two BST capacitor sets on the two resonators are simulated together in the second simulation (as shown in Figure 6.2b). Figure 6.9 indicates that the simulation including two BST capacitor sets

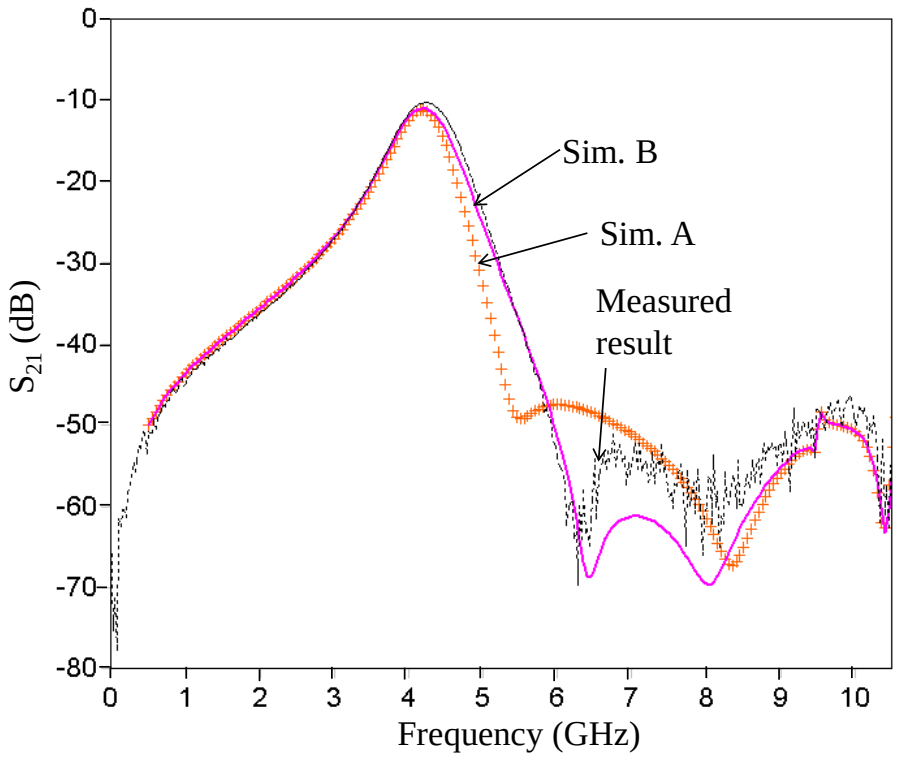

Figure 6.9: Two filter simulation results along with a measured result are plotted. For one of the simulations a single BST capacitor set as shown in Figure 6.8 is simulated (Sim. A) while two BST capacitor sets on the two resonators are simulated together (Sim. B) in the second simulation. It can be observed that the 3-dB filter bandwidth results of the two simulations (Sim. A and Sim. B) differ. This is because when the two BST capacitor sets are simulated together (as is the case in a fabricated device) the electric coupling between the capacitors is also taken into consideration which results in widening of the bandwidth. The simulation including two BST capacitor sets together is a closer match to the measured results.

Table 6.5: Comparison of measured and simulated insertion loss (IL) results. The simulation result using two BST capacitor sets simulated together is used for the comparison.

Measured			Simulated		
Frequency (GHz)	IL (dB)	3-dB Bandwidth (MHz)	Frequency (GHz)	IL (dB)	3-dB Bandwidth (MHz)
4.25	10.29	700	4.20	10.99	625

Table 6.6: Comparison of measured and simulated return loss (RL) results. The simulation result using two BST capacitor sets simulated together is used for the comparison.

Measured		Simulated	
Frequency (GHz)	RL (dB)	Frequency (GHz)	RL (dB)
4.35	7.98	4.35	8.92

together is a closer match to the measured results. This is because when the two BST capacitors sets are simulated together the electric coupling between the capacitor sets (which occurs in a fabricated device) is also taken into consideration. This results in widening of the bandwidth compared to when a single BST capacitor set is used.

Tables 6.5 and 6.6 compare the zero-bias measured and simulated results. The simulation result using two BST capacitor sets simulated together is used for the comparison. The results indicate a close match in terms of the insertion loss, return loss, passband and out-of-band wave shape, and filter bandwidth. The simulation results can be used to identify and isolate the sources of loss as will be discussed in the following section. Simulation results vary slightly from those tabulated in Chapter 5 as an EM model of the BST capacitor was used here while a lumped model of the BST capacitor is used in Chapter 5.

6.4 Sources of Filter Insertion Loss

A close match between the simulated (Sim. B in Figure 6.9) and measured results indicate that all the major sources of loss have been captured by the EM simulations. Hence, slight modifications to the existing simulation setup can be used to further isolate the potential sources of loss. Table 6.7 indicates the loss contributions from different sections of the filter by modifying the simulations to isolate the sources of loss. For example, to find the metal loss from the BST capacitor section, the BST capacitor EM model was modified wherein the metal is considered lossless. This modified BST capacitor EM model is run and the modified result of the filter simulation is compared with the earlier simulation results (that included all the losses)

Table 6.7: Sources of Filter Insertion Loss (cap. = capacitor).

Loss Source	Location on filter	Insertion Loss (dB)
Metal	BST cap.	6.950
BST dielectric	BST cap.	1.204
Alumina dielectric	BST cap.	0.002
Metal	Filter layout	0.574
Via	Filter layout	1.594
Alumina dielectric	Filter layout	0.006
Mismatch loss	-	0.143
Unaccounted losses	-	0.516

Table 6.8: Filter EM simulation results with different BST capacitor metallizations (IL = insertion loss, RL = return loss).

BST cap. metal	Metal thickness (μm)	IL dB	RL dB
Cr/Au	0.01/0.2	10.99	8.92
Al/Au	0.01/0.2	6.76	12.53
Ag	0.21	5.77	13.53

to determine the loss contribution from the BST capacitor metal section. Table 6.7 suggests that the major source of loss (6.95 dB) is coming from the metallization in the BST capacitor region. This loss can be represented as an equivalent lumped resistance of 1.4 Ω in series with an equivalent BST lumped capacitor.

6.5 BST Capacitor and Filter Loss

6.5.1 Effect of Different BST Capacitor Metallizations on Filter Loss

An EM simulation of the BST capacitor with different metallizations was undertaken. Figure 6.10 shows the S-parameter results for the filter with the different metallizations. The results tabulated in Table 6.8 indicate a variation in loss as different metals were used. A reduction in

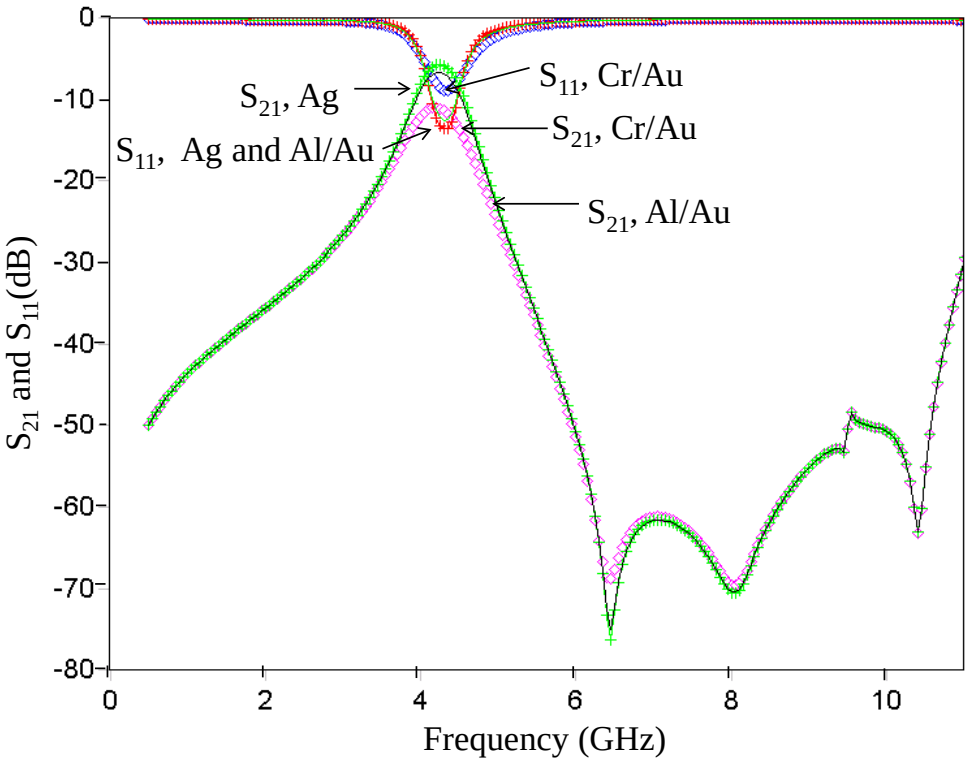

Figure 6.10: EM simulation of entire filter (including BST capacitor layout) with different metallizations for the BST capacitor regions.

the insertion loss is observed when the metallization is changed from chromium/gold (Cr/Au) to aluminum/gold (Al/Au) or silver (Ag) due to their higher conductivities.

6.5.2 Current Density Plots on Capacitor Metal Surfaces

The filter design discussed here has thin-film BST IDC capacitors. For simplicity, current densities on a simple gap capacitor using two different substrates were plotted. This helps study the effect that the underlying substrate has over the current flow on the metal surface of the gap capacitors. The two substrates under consideration are alumina substrate and alumina with a thin-film of BST over the top (mixed substrate).

Figure 6.11 is a current density plot using Sonnet EM simulator. It can be seen that the current density is enhanced at the edges of the metal electrodes around the gap region (circled in the figure) for the capacitor on an alumina/thin-film BST mixed substrate compared to that for the capacitor on an alumina substrate. This suggests that a high-permittivity substrate can influence the current flow on the metal surface. The scales on the current density plots have the same range to aid easier visual comparison.

The result can be extrapolated for capacitors with multiple finger electrodes that form multiple gaps like an IDC capacitor on an alumina/thin-film BST substrate. As the number of fingers and gaps increase, more regions of high current density will be observed. High current density observed on metal surfaces in thin regions close to the gap increases the equivalent resistance. This can cause an increase in the BST capacitor metal conductor loss which in turn can lead to a high filter insertion loss.

A similar relation between high-permittivity of thin-film ferroelectric-based coplanar waveguide (CPW) capacitors and increased conductor loss has been cited in literature based on purely analytical techniques. Current density is typically higher at the metal edges but Carlsson and Gevorgian [82] predicted that the current crowding is more pronounced at the edges of the conducting strips in thin-film ferroelectric CPW structures. They used conformal mapping and partial capacitance techniques to predict enhanced current crowding.

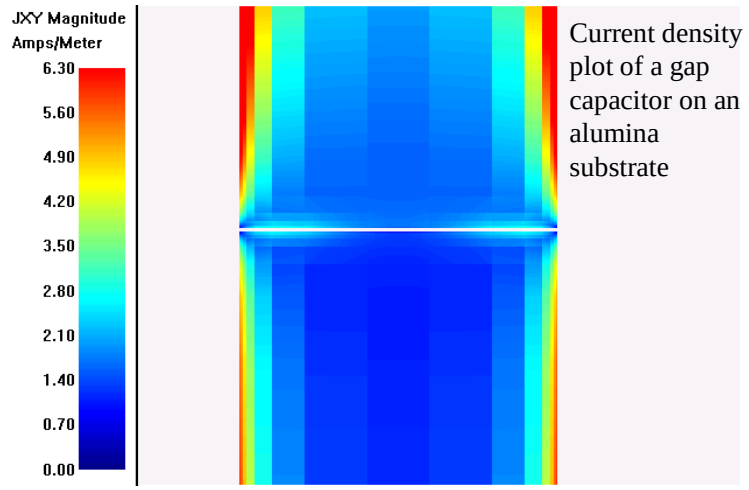

(a)

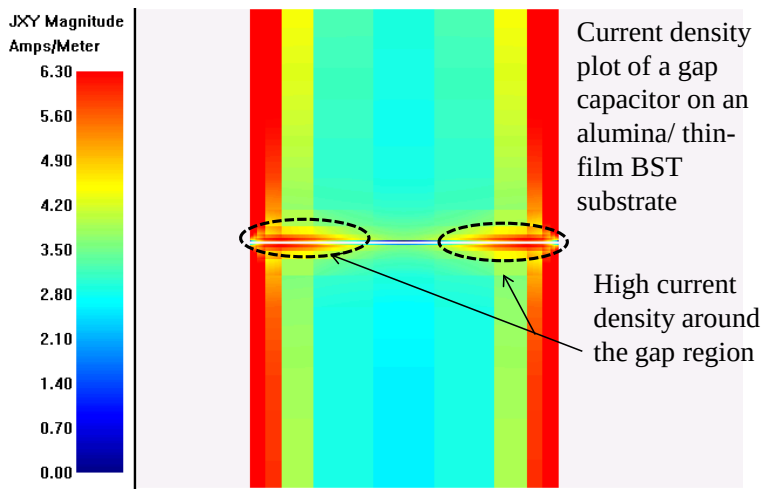

(b)

Figure 6.11: Comparison of current density plots using Sonnet for a simple gap capacitor fabricated on an alumina substrate and on an alumina substrate with a thin-film of BST over the top: (a) current density plot for a simple gap capacitor on an alumina substrate; and (b) current density plot for a simple gap capacitor on an alumina substrate with a thin-film of BST over the top.

Kim *et al.* [83] proposed a new integrated CPW-based phased array antenna design using a ferroelectric phase shifter wherein the metal conductor did not make direct contact with ferroelectric (dielectric) material. Instead, a thin layer (0.1 μm) of Silicon Dioxide (SiO_2) was placed between the conductor and the ferroelectric layer. A via was drilled through the center-conductor of the CPW configuration so that it selectively made direct contact with the ferroelectric layer while the thin-layer of oxide prevented the CPW ground side-conductors from making direct contact with the ferroelectric layer. This modified arrangement provided appropriate biasing required to tune the ferroelectric while at the same time circumventing the enhanced ferroelectric current-crowding problem. A nearly three-fold improvement in insertion loss was observed while maintaining almost the same tunability.

Carlsson *et al.* and Kim *et al.* [82, 83] referred to a CPW configuration while the design considered in this dissertation involves a microstrip configuration. Nevertheless, inferences drawn from both of them indicate that a thin ferroelectric film directly under the metallization has an influence on the pattern of current flow over the metal surface.

6.6 Conclusion

This chapter provided an in-depth detail of the EM simulation setup for a complete two-pole BST-based tunable bandpass filter. A close match between the simulation and measured result ensured that the EM simulator was appropriately setup to capture all the major sources of loss. Modified EM simulations were then run to identify and explore the loss contributions from different regions of the filter. It was observed that the metal loss associated with the BST capacitor was a significant contributor to the overall high filter insertion loss as it accounted for 63% of the total filter loss. An EM simulation experiment with different BST capacitor metallizations indicated that the filter loss could be reduced by changing the BST capacitor metallization from Cr/Au to Al/Au or Ag. A measurement experiment using filters fabricated with these three different metallizations would be an interesting future step to consider. It must be noted that the filters fabricated with Ag metallization in the BST capacitor regions must

not be biased using a DC voltage source (zero-bias measurements can be taken) as they have been known to exhibit electro-migration problems lowering the breakdown voltage of the BST capacitors. Ag was chosen as one of the metals in the loss experiment to study its influence on filter insertion loss as it is one of the few metals that adheres well to BST.

In this chapter only the zero-bias insertion loss result was considered. This is because zero-bias filter result in a tunable BST based filter design has the worst-case insertion loss compared to the insertion loss at higher tuning voltages.

A comparison of the current flow pattern on the surface of two different types of BST capacitors, one with an alumina substrate and the other with an alumina/thin-film BST mixed-substrate, was undertaken. The results confirmed a high current density on the metal surface adjacent to the capacitor gap-region when they were designed on an alumina/thin-film BST mixed-substrate. These results along with the enhanced current-crowding predictions and the ferroelectric-based phase-shifter design cited in literature for ferroelectric based CPW structures point to the high-permittivity of the BST as a possible cause for the high insertion loss in ferroelectric based filters. Future ferroelectric based filter designs and topologies should consider this inference drawn between high-permittivity and increased metal loss to build lower insertion loss and higher performance filters.

Chapter 7

Conclusion and Future Work

7.1 Summary of Research and Original Contributions

This dissertation provided design methodologies to improve the performance of a ferroelectric based tunable filter and explored the origins of loss in these filters. A new system-aware design method to optimize the performance of a tunable ferroelectric filter was developed. A design approach that aims to indirectly improve loss by reducing the fringe capacitance of a tunable capacitor was described. A new filter topology with high tunability, constant bandwidth, steep filter skirt selectivity on the image side of the passband and wide stop-band rejection was designed using ferroelectric-based tunable transmission-line resonators. The cause of high insertion loss in ferroelectric based filters was explored and the origins of this loss isolated after analyzing EM simulation and measured results.

A new system-based design guideline was outlined for tunable filters. It does not constrain the filter bandwidth as long it falls within the analog bandwidth range of the ADC. Earlier guidelines nearly always required maintaining a constant filter bandwidth during the entire tuning range (within a certain tolerance limit set by the design specifications). A new system-aware figure of merit (FOM) was presented that considered the worst case filter performance parameters and a newly defined tuning sensitivity term that captured the underlying relation

between frequency tunability and material tunability. A previously used FOM by tunable filter designers works well to compare the performance of stand-alone tunable filters in isolation from the rest of the system. However, filter design specifications can be relaxed in certain system architectures. Hence, the performance of a stand-alone filter that does not compare well with other stand-alone filters using the earlier FOM may still be preferred for a particular system application. The new system-based design guideline together with the system-aware FOM developed in this dissertation leads to a design concept that differs from the earlier-FOM in that it can be used to optimize a filter design for a specific system application.

The existence of a non-tunable parasitic fringe capacitance associated with planar gap ferroelectric capacitors used in the research work is confirmed by simulation and measured results. These ferroelectric capacitors are connected in series with transmission lines to form tunable resonators in filter designs. This fringe capacitance becomes an appreciable proportion of the tunable capacitance when the gap capacitor value is reduced to increase the resonant frequency of the filter to X-band and higher. Capacitor layout topologies designed to reduce the fringe-capacitance can increase the capacitance tunability and thus the filter tunability. The trade-off between filter tunability and unloaded Q described in Chapter 4 can be used to trade-off some of the increased filter tunability to obtain higher filter resonator unloaded Q (i.e. lower filter insertion loss).

A new two-pole tunable filter topology that provides high tunability ($> 30\%$) and introduces multiple transmission zeroes to provide steep filter-skirts on the image side of the passband, wide stop-band rejection, and constant bandwidth was designed, simulated, fabricated, and measured. The filter was fabricated using BST varactors to form tunable resonators. A constant bandwidth requirement in the design was necessary as the filter was designed for a very high tunability of $\geq 35\%$ and the topology of the filter chosen would otherwise increase the filter bandwidth during tuning. The constant bandwidth requirement ensured that the filter bandwidth would never be wider than the maximum bandwidth permitted by the typical system analog-to-digital converters (ADCs) available today. Experimental characterization of a tunable

filter designed indicated a high-loss of 10.3 dB which suggests that the increase in BST varactor value has a bigger effect on increasing the filter insertion loss than the number of resonators used in the tunable ferroelectric filter.

EM simulations of a tunable ferroelectric-based two-pole filter (including the BST capacitor layout) was performed by incorporating all of the fabrication details of a filter that was measured. A comparison of the simulated and measured results indicated that the EM simulator was appropriately setup to capture all of the major sources of loss. The simulations and measured results were then analyzed to isolate the loss contributions from different regions of the filter. The results indicated that the metallization for the varactor sections of the tunable resonator contributed to 63% of the filter insertion loss. A current flow pattern on the surface of a gap capacitor with and without the thin-film BST was simulated. The results revealed that a capacitor with a thin-film of high-permittivity BST had exceptionally high current densities adjacent to the gap. This suggests that the high-permittivity of the underlying BST layer influences the current pattern on the metallizations directly above it. Enhanced current-crowding along outer thin regions on the signal pads in a ferroelectric-based CPW capacitor have also been theoretically and experimentally predicted in literature for coplanar waveguide capacitors. These results together infer that the high permittivity of the BST that provides high tunability and compact devices could also be responsible for the high loss in ferroelectric-based tunable filters.

7.2 Future Research

Several insights were gained while undertaking this research. The inferences drawn from the results and conclusions derived in this dissertation can be used to build on future research initiatives.

Chapter 3 suggests that the frequency tunability can be enhanced (and the insertion loss can indirectly be reduced) by designing better capacitor topologies to reduce the fringe capacitance. The different capacitor topologies that could enhance filter performance is open to research.

While different ways to reduce insertion loss in ferroelectric based filters is being researched it might be useful to get an understanding on the best practically achievable insertion loss for a topology. For this study the filter designs discussed in Chapter 4 and Chapter 5 could be modified by removing the tunable capacitors and using non-tunable quarter wave-length resonators. It must be noted that in combline-based topologies constructed using pure TEM mode transmission-lines such as stripline, removing the tunable capacitor would result in a design with no filter passband. However, as the designs used in this research work use quasi-TEM microstrip transmission lines, the passband would still exist.

Chapter 5 discussed the lossy simulation results of the tunable filter within reasonable tolerance. A lumped BST capacitor model using a constant series resistance was used in the simulations. An EM simulation of the BST varactor that varies the dielectric permittivity of the BST material would provide a more accurate model. A comparison between the lumped BST capacitor loss model and the BST EM simulation model could provide a more accurate equivalent series resistance value for each center frequency.

The results in Chapter 5 indicate that the value of the BST varactor used on each tunable resonator has a bigger impact on the filter insertion loss than the number of resonators used in the filter design. A higher BST varactor value results in a higher insertion loss and vice-versa. This result must be considered while designing future transmission-line resonator based tunable filter designs.

The filters designed for this research work have a microstrip layout and hence the integrated planar ferroelectric varactors also have a bottom ground layer. The bottom ground layer could be selectively etched underneath the BST varactor areas to study the effect it has on the filter insertion loss.

Appendix A describes a prototype of a tunable quasi-elliptic response filter topology. While the measured insertion loss of 4.4 dB for this filter without applied bias voltage is promising, the tunability of the filter as well as methods to improve the out-of-band rejection have not been explored.

Designing RF/microwave filters without vias is advantageous both from the filter fabrication as well as the yield standpoints. Many of the microstrip-based filter topologies however include vias such as the ones used in this dissertation. One of the newer filter topologies discussed in Chapter 2, namely the zig-zag hairpin-comb filter topology, is very attractive for via-less, narrow-band, constant bandwidth, compact, quasi-elliptic response tunable filter applications. A tunable ferroelectric filter design based on this topology could be explored in the future.

An EM simulation experiment with different BST capacitor metallizations discussed in Chapter 6 suggests that the filter loss could be reduced by changing the BST capacitor metallization from Cr/Au to Al/Au or Ag. A measurement experiment using filters fabricated with these three different BST capacitor metallizations would be an interesting future step to consider. It must be noted that filters fabricated with Ag metallization in the BST capacitor regions must not be biased using a DC voltage source (zero-bias measurements can be taken) as they have been known to exhibit electro-migration problems lowering the breakdown voltage of the BST capacitors. Ag was chosen as one of the metals in the loss experiment to study its influence on filter insertion loss as it is one of the few metals that adheres well to BST.

An investigation into finding the loss origins of high insertion loss associated with ferroelectric filters in Chapter 6 suggests that the high insertion loss in these filters is associated with the high permittivity of the ferroelectric material. As ferroelectric varactors are part of the transmission-line based tunable resonators, the high conductive loss associated with the ferroelectric varactors translates into high insertion loss in these filters. Hence, a topology that will not place the ferroelectric material in the resonators would reduce the direct influence these materials have over the filter insertion loss. A relatively new switched-delay line tunable filter topology discussed in Chapter 2 with ferroelectric material based switches would be a very interesting topology to explore further.

REFERENCES

[1] T. Carey, Aeroflex Test Solutions. Meeting the challenge of multi-standard wireless communications testing. [Online]. Available: http://www.wirelessdesignmag.com

[2] X. Zhu, V. Lee, J. Phillips, and A. Mortazawi, "An intrinsically switchable FBAR filter based on barium titanate thin films," *IEEE Microw. and Wireless Components Letters*, vol. 19, no. 6, pp. 359–361, Jun. 2009.

[3] A. R. Brown and G. M. Rebeiz, "A varactor-tuned RF filter," *IEEE Trans. Microw. Theory Tech.*, vol. 48, no. 7, pp. 1157–1160, July 2000.

[4] G. Subramanyam, F. W. V. Keuls, and F. A. Miranda, "A K-band-frequency agile microstrip bandpass filter using a thin-film HTS/ferroelectric/dielectric multilayer configuration," *IEEE Trans. Microw. Theory Tech.*, vol. 48, no. 4, pp. 525–530, Apr. 2000.

[5] G. L. Matthaei, "Narrow-band, fixed-tuned, and tunable bandpass filters with zig-zag hairpin-comb resonators," *IEEE Trans. Microw. Theory Tech.*, vol. 51, no. 4, pp. 1214–1219, Apr. 2003.

[6] H. Joshi, H. H. Sigmarsson, D. Peroulis, and W. J. Chappel, "Highly loaded evanescent cavities for widely tunable high-Q filters," in *2007 IEEE MTT-S Int. Microwave Symposium*, Honolulu, HI, Jun. 2007, pp. 2133–2136.

[7] P. W. Wong and I. C. Hunter, "A new class of low-loss high-linearity electronically reconfigurable microwave filter," *IEEE Trans. Microw. Theory Tech.*, vol. 56, no. 8, pp. 1945–1953, Aug. 2008.

[8] J. Nath, *Design and Characterization of Frequency Agile RF and Microwave Devices using Ferroelectrics*. PhD Thesis, North Carolina State University, Raleigh, NC, 2006.

[9] P. G. Lam, V. Haridasan, Z. Feng, M. B. Steer, A. I. Kingon, and J.-P. Maria, "Scaling issues in ferroelectric barium strontium titanate tunable planar capacitors," *IEEE Trans. Ultrason., Ferroelectr., Freq. Control*, vol. 59, no. 2, pp. 198–204, Feb. 2012.

[10] Navy multiband terminal. [Online]. Available: http://www.raytheon.com/capabilities/products/nmt/

[11] (2011, Dec.) The tinker's toolbox - Raytheon's new naval multiband satellite system. [Online]. Available: http://www.ecnmag.com/podcasts/2011/12/tinkers-toolbox-raytheons-new-naval-multiband-satellite-system

[12] R. Whatley and D. Pilgrim. (2012, Mar.) Front-end tuning bolsters multi-band wireless performance. [Online]. Available: http://electronicdesign.com/article/communications/frontend-tuning-bolsters-multiband-wireless-performance-73671

[13] Agilent, Application Note. Agilent multi-mode handset manufacturing challenges and solutions. [Online]. Available: http://cp.literature.agilent.com/litweb/pdf/5989-4083EN.pdf

[14] V. Haridasan, P. G. Lam, Z. Feng, W. M. Fathelbab, J.-P. Maria, A. I. Kingon, and M. B. Steer, "Tunable ferroelectric microwave bandpass filters optimised for system-level integration," *IET Microwave, Antennas and Propagation*, vol. 5, no. 10, pp. 1234–1241, Jul. 2011.

[15] B. E. Carey-Smith, P. A. Warr, P. R. Rogers, M. A. Beach, and G. S. Hilton, "Flexible frequency discrimination subsystems for reconfigurable radio front ends," *EURASIP J. On Wireless Communications and Networking*, vol. 2005, pp. 354–363, Mar. 2005.

[16] C. Y. Tan and C. K. Ong, "Planar tuanble HTS microwave filter with patterned ferroelectric thin film," *Supercond. Sci. Technol.*, vol. 19, no. 2, pp. 212–216, Feb. 2006.

[17] H. T. Su, P. M. Suherman, T. J. Jackson, F. Huang, and M. J. Lancaster, "Novel tunable bandpass filter realized using barium-strontium-titanate thin films," *IEEE Trans. Microw. Theory Tech.*, vol. 56, no. 11, pp. 2468–2473, Nov. 2008.

[18] J. Sigman, C. D. Nordquist, P. G. Clem, G. M. Kraus, and P. S. Finnegan, "Voltage-controlled Ku-band and X-band tunable combline filters using barium-strontium-titanate," *IEEE Commun. Lett.*, vol. 18, no. 9, pp. 593–595, Sept. 2008.

[19] J. Nath, D. Ghosh, J.-P. Maria, A. I. Kingon, W. Fathelbab, P. D. Franzon, and M. B. Steer, "An electronically tunable microstrip bandpass filter using thin-film barium-strontium-titanate (BST) varactors," *IEEE Trans. Microw. Theory Tech.*, vol. 53, no. 9, pp. 2707–2712, Sept. 2005.

[20] V. Pleskachev and I. Vendik, "Tunable microwave filters based on ferroelectric capacitors," in *15th International Conference on Microwaves, Radar and Wireless Communications*, Warsaw, Poland, May 2004, pp. 1039–1043.

[21] S. Courrèges, Y. Li, Z. Zhao, K. Choi, A. T. Hunt, and J. Papapolymerou, "Two-pole X-band-tunable ferroelectric filters with tunable center frequency, fractional bandwidth and return loss," *IEEE Trans. Microw. Theory Tech.*, vol. 57, no. 12, pp. 2872–2881, Dec. 2009.

[22] V. Pleskachev and I. Vendik, "Figure of merit of tunable ferroelectric planar filters," *Proc. of 33rd European Microwave Conference*, pp. 191–194, Oct. 2003.

[23] I. Vendik, V. Pleskachev, and O. Vendik, "Figure of merit and limiting characteristics of tunable ferroelectric microwave devices," in *Progress in Electromagnetics Research Symposium*, Hangzhou, China, Aug. 2005, pp. 327–330.

[24] W. L. Jones, "Design of tunable combline filters of near-constant bandwidth," *Electronics Letters*, vol. 1, no. 6, pp. 156–158, Aug. 1965.

[25] I. C. Hunter and J. D. Rhodes, "Electronically tunable microwave bandpass filters," *IEEE Trans. Microw. Theory Tech.*, vol. 30, no. 9, pp. 1354–1360, Sep. 1982.

[26] I. Vendik, O. Vendik, V. Pleskachev, A. Svishchev, and R. Wordenweber, "Design of tunable ferroelectric filters with a constant fractional bandwidth," in *2001 IEEE MTT-S Int. Microwave Symposium*, Phoenix, AZ, May 2001, pp. 1461–1464.

[27] P. Jarry and J. Beneat, *Design and Realizations Of Miniaturized Fractal RF and Microwave Filters.* New Jersey: John Wiley and Sons, Inc., 2009.

[28] M. Norling, A. Vorobiev, H. Jacobsson, and S. Gevorgian, "A low-noise K-band VCO based on room-temperature ferroelectric varactors," *IEEE Trans. Microw. Theory Tech.*, vol. 55, no. 2, pp. 361–369, Feb. 2007.

[29] I. Hunter, *Theory and Design of Microwave Filters.* London, UK: The Institution of Electrical Engineers., 2001.

[30] S. B. Cohn, "Dissipation loss in multiple-coupled-resonator filters," *Proc. of the Institute of Radio Engineers*, vol. 47, no. 8, pp. 1342–1348, Aug. 1959.

[31] G. L. Matthaei, L. Young, and E. M. T. Jones, *Microwave Filters, Impedance-Matching Networks, and Coupling Structures.* New York: McGraw-Hill Book Co., Inc., 1964.

[32] S. Gevorgian, *Ferroelectrics in Microwave Devices, Circuits and Systems.* Springer., 2009.

[33] M. Hagensen, "Narrowband microwave bandpass filter design by coupling matrix synthesis," *Microwave J.*, vol. 53, no. 4, pp. 218–226, Apr. 2010.

[34] P. W. Wong and I. C. Hunter, "Electronically tunable filters," *IEEE Microwave Magazine*, vol. 10, no. 6, pp. 46–54, Oct. 2009.

[35] D. Packiaraj, V. S. Reddy, G. J. D'Mello, and A. T. Kalghatgi, "Electronically switchable suspended substrate stripline filters," in *RF and Microwave Conference*, Subang, Selangor, Malaysia, Oct. 2004, pp. 64–66.

[36] T. Pensala, *Thin-Film Bulk Acoustic Wave Devices.* PhD Dissertation, Aalto University, School of Science, Finland, 2011.

[37] X. Zhu, J. Phillips, and A. Mortazawi, "A DC voltage dependant switchable thin film bulk wave acoustic resonator using ferroelectric thin film," in *2007 IEEE MTT-S Int. Microwave Symposium*, Honolulu, HI, Jun. 2007, pp. 671–674.

[38] J. Uher and W. J. R. Hoefer, "Tunable microwave and millimeter-wave band-pass filters," *IEEE Trans. Microw. Theory Tech.*, vol. 39, no. 4, pp. 643–653, Apr. 1991.

[39] P. S. Carter, Jr., "Magnetically-tunable microwave filters using single-crystal yttrium-iron-garnet resonators," *IRE Transactions on Microwave Theory and Techniques*, vol. 9, no. 3, pp. 252–260, May 1961.

[40] C. L. Goldsmith, Z. Yao, S. Eshelman, and D. Denniston, "Performance of low-loss RF MEMS capacitive switches," *IEEE Microwave and Guided Wave Letters*, vol. 8, no. 8, pp. 269–271, Aug. 1998.

[41] C. Goldsmith, T.-H. Lin, B. Powers, W.-R. Wu, and B. Norvell, "Micromechanical membrane switches for microwave applications," in *1995 IEEE MTT-S Int. Microwave Symposium Digest*, May 1995, pp. 91–94.

[42] K. Entesari and G. M. Rebeiz, "A 12–18 GHz three-pole RF MEMS tunable filter," *IEEE Trans. Microw. Theory Tech.*, vol. 53, no. 8, pp. 2566–2571, Aug. 2005.

[43] M. Houssini, A. Pothier, A. Crunteanu, and P. Blondy, "A 2-pole digitally tunable filter using local one bit varactors," in *2008 IEEE MTT-S Int. Microwave Symposium*, Atlanta, GA, Jun. 2008, pp. 37–40.

[44] S. Courrèges, Y. Li, Z. Zhao, K. Choi, A. Hunt, and J. Papapolymerou, "A low loss X-band quasi-elliptic ferroelectric tunable filter," *IEEE Microwave and Wireless Components Letters*, vol. 19, no. 4, pp. 203–205, Apr. 2009.

[45] B. Noren, "Thin film barium strontium titanate (BST) for a new class of tunable RF components," *Microwave J.*, vol. 47, no. 5, pp. 210–220, May 2004.

[46] J.-S. Hong and M. J. Lancaster, *Microstrip Filters For RF/Microwave Applications.* New York: John Wiley and Sons, Inc., 2001.

[47] B-W. Kim, and S-W. Yun, "Varactor-tuned combline bandpass filter using step-impedance microstrip lines," *IEEE Trans. Microw. Theory Tech.*, vol. 52, no. 4, pp. 1279–1283, Apr. 2004.

[48] G. L. Matthaei, N. O. Fenzi, R. J. Forse, and S. M. Rohlfing, "Hairpin-comb filters for HTS and other narrow-band applications," *IEEE Trans. Microw. Theory Tech.*, vol. 45, no. 8, pp. 1226–1231, Aug. 1997.

[49] Q. Zhang and T. Itoh, "Computer-aided design of evanescent-mode waveguide filter with nontouching E-plane fins," *IEEE Trans. Microw. Theory Tech.*, vol. 36, no. 2, pp. 404–412, Feb. 1988.

[50] B. F. Nicholson and I. L. Powell, "Equivalence between evanescent mode and combline filters," *IET Electronic Letters*, vol. 3, no. 11, pp. 495–496, 1967.

[51] X. Gong, A. Margomenos, B. Liu, S. Hajela, L. P. B. Katehi, and W. J. Chappell, "Precision fabrication techniques and analysis on high-Q evanescent-mode resonators and filters of different geometries," *IEEE Trans. Microw. Theory Tech.*, vol. 52, no. 11, pp. 2557–2566, Nov. 2004.

[52] X. Liu, L. P. B. Katehi, W. J. Chappell, and D. Peroulis, "A 3.4–6.2 GHz continuously tunable electrostatic MEMS resonator with quality factor of 460-530," in *2009 IEEE MTT-S Int. Microwave Symposium*, Boston, MA, Jun. 2009, pp. 1149–1152.

[53] P. W. Wong and I. C. Hunter, "Electronically reconfigurable microwave bandpass filter," *IEEE Trans. Microw. Theory Tech.*, vol. 57, no. 12, pp. 3070–3079, Dec. 2009.

[54] C. D. Nordquist, C. L. Goldsmith, C. W. Dyck, G. M. Kraus, P. S. Finnegan, F. Austin IV, and C. T. Sullivan, "X-band RF MEMS tuned combline filter," *IET Electronic Letters*, vol. 41, no. 2, pp. 76–77, Jan. 2005.

[55] K. M. Rabe, C. H. Ahn, and J.-M. Triscone, *Physics of Ferroelectrics: A Modern Perspective*. Springer, 2007.

[56] Computer Simulation Technology, version 2010 and 2011. [Online]. Available: www.cst.com

[57] M. Steer, *Microwave and RF Design: A Systems Approach*. Raleigh, NC: SciTech Publishing, Inc., 2010.

[58] C. Bowick, J. Blyler, and C. Ajluni, *RF Circuit Design*. Burlington, MA: Elsevier Inc., 2008.

[59] Sonnet Software, version 11.52 and 13.52. [Online]. Available: www.sonnetsoftware.com

[60] P. G. Lam, Z. Feng, V. Haridasan, A. I. Kingon, M. B. Steer, and J.-P. Maria, "The impact of metallization thickness and geometry for X-band tunable microwave filters," *IEEE Trans. Ultrason., Ferroelectr., Freq. Control*, vol. 56, no. 5, pp. 906–911, May 2009.

[61] Z. Feng, W. M. Fathelbab, P. G. Lam, V. Haridasan, J.-P. Maria, A. I. Kingon, and M. B. Steer, "A 6.2–7.5 GHz tunable bandpass filter with integrated barium strontium titanate (BST) interdigitated varactors utilizing silver/copper metallization," in *2009 Radio and Wireless Symposium*, San Diego, CA, Jan. 2009, pp. 638–641.

[62] I. B. Vendik, O. G. Vendik, and E. L. Kollberg, "Commutation quality factor of two-state switching devices," *IEEE Trans. Microw. Theory Tech.*, vol. 48, no. 5, pp. 802–808, May 2000.

[63] Z. Feng, W. M. Fathelbab, P. G. Lam, V. Haridasan, J-P. Maria, A. I. Kingon and M. B. Steer, "Narrowband barium strontium titanate (BST) tunable bandpass filters at X-band," in *2009 IEEE MTT-S Int. Microwave Symposium*, Boston, MA, Jun. 2009, pp. 1061–1064.

[64] A. Kozyrev, O. Buslov, V. Keis, D. Dovgan, I. Kotelnikov, P. Kulik, L. Sengupta, L. Chiu, and X. Zhang, "14 GHz tunable filters base on ferroelectric films," *Integrated Ferroelectrics*, vol. 55, no. 1, pp. 905–913, Apr. 2003.

[65] A. C. Guyette, I. C. Hunter, and R. D. Pollard, "A new class of selective filters using low-Q components suitable for MMIC implementation," in *2004 IEEE MTT-S Int. Microwave Symposium Digest*, Jun. 2004, pp. 1959–1962.

[66] K. V. Puglia, "A general design procedure for bandpass filters derived from low pass prototype elements: Part I," *Microwave J.*, vol. 43, no. 12, pp. 22–38, Dec. 2000.

[67] D. M. Pozar, *Microwave Engineering*. Asia: John Wiley and Sons, Inc., 2005.

[68] M. Dishal, "Alignment and adjustment of synchronously tuned multiple-resonant circuit-filters," *Proc. IRE*, vol. 39, pp. 1448–1455, Nov. 1951.

[69] D. G. Swanson, Jr., "Narrow-band microwave filter design," *IEEE Microwave Magazine*, vol. 8, no. 5, pp. 105–114, Oct. 2007.

[70] R. Rhea, "EM enables classic filter technique," *Microwave J.*, vol. 50, no. 2, pp. 138–146, Feb. 2007.

[71] R. Levy, "Filters with single transmission zeros at real or imaginary frequencies," *IEEE Trans. Microw. Theory Tech.*, vol. 24, no. 4, pp. 172–181, Apr. 1976.

[72] C.-M. Tsai, S.-Y. Lee, and C.-C. Tsai, "Hairpin filters with tunable transmission zeros," in *2001 IEEE MTT-S Int. Microwave Symposium Digest*, Mar. 2001, pp. 2175–2178.

[73] M. Sánchez-Renedo, "High-selectivity tunable planar combline filter with source/load-multiresonator coupling," *IEEE Microwave and Wireless Components Letters*, vol. 17, no. 7, pp. 513–515, Jul. 2007.

[74] C.-W. Tang, Y.-C. Lin, and C.-Y. Chang, "Realization of transmission zeros in combline filters using an auxiliary inductively coupled ground plane," *IEEE Trans. Microw. Theory Tech.*, vol. 51, no. 10, pp. 2112–2118, Oct. 2003.

[75] R. J. Cameron, "Advanced coupling matrix synthesis techniques for microwave filters," *IEEE Trans. Microw. Theory Tech.*, vol. 51, no. 1, pp. 1–10, Jan. 2003.

[76] R. J. Cameron, C. M. Kudsia, and R. R. Mansour, *Microwave filters for communication systems: fundamentals, design, and applications.* Hoboken, N.J.: Wiley-Interscience, 2007.

[77] L.-H. Hsieh and K. Chang, "Tunable microstrip bandpass filters with two transmission zeros," *IEEE Trans. Microw. Theory Tech.*, vol. 51, no. 2, pp. 520–525, Feb. 2003.

[78] M.-S. Chung, I.-S. Kim, and S.-W. Yun, "Varactor-tuned hairpin bandpass filter with enhanced stopband performance," in *Asia-Pacific Microwave Conference*, Dec. 2006, pp. 645–648.

[79] M. A. El-Tanani and G. M. Rebeiz, "Corrugated microstrip coupled lines for constant absolute bandwidth tunable filters," *IEEE Trans. Microw. Theory Tech.*, vol. 58, no. 4, pp. 956–963, Apr. 2010.

[80] R. York, A. Nagra, E. Erker, T. Taylor, P. Periaswamy, J. Speck, S. Streiffer, and O. Auciello, "Microwave integrated circuits using thin-film BST," in *12th International Symposium on Applications of Ferroelectrics*, 2000, pp. 195–200.

[81] A. Tombak, J.-P. Maria, F. Ayguavives, Z. Jin, G. T. Stauf, A. I. Kingon, and A. Mortazawi, "Tunable barium strontium titanate thin film capacitors for RF and microwave applications," *IEEE Microwave and Wireless Components Letters*, vol. 12, no. 1, pp. 3–5, Jan. 2002.

[82] E. Carlsson and S. Gevorgian, "Effect of enhanced current crowding in a CPW with a thin ferroelectric film," *IET Electronic Letters*, vol. 33, no. 2, pp. 145–146, Jan. 1997.

[83] W. Kim, M. F. Iskander, and W. D. Palmer, "An integrated phased array antenna design using ferroelectric materials and the continuous transverse stub technology," *IEEE Transactions on Antennas and Propagation*, vol. 54, no. 11, pp. 3095–3105, Nov. 2006.

[84] S.-Y. Lee and C.-M. Tsai, "New cross-coupled filter design using improved hairpin resonators," *IEEE Trans. Microw. Theory Tech.*, vol. 48, no. 12, pp. 2482–2490, Dec. 2000.

APPENDIX

Appendix A

Two-Pole Ferroelectric Based Hairpin Resonator Filter

A.1 Introduction

A quasi-elliptic filter response having steep filter selectivity on both sides of the passband is a desirable feature in a filter for certain system applications. Such a filter response can reject unwanted signals and increase the out-of-band rejection in the close vicinity of either sides of the passband. This appendix presents an alternative design to that described in the body of the dissertation. A topology based on the two-pole hairpin half-wavelength resonators discussed by Tsai *et al.* [72] is used to design a filter with a quasi-elliptic response. The input and the output feed lines make direct contact with the transmission line resonators used in the filter design. In this respect, it differs from the coupled-line feed filter topologies discussed in Chapters 4 and 5 of this dissertation

A.2 Filter Topology and Design

Figure A.1 is the layout of the two-pole hairpin resonator used in the design. Although based on a quick look at this topology one might infer that there are four open resonators in this

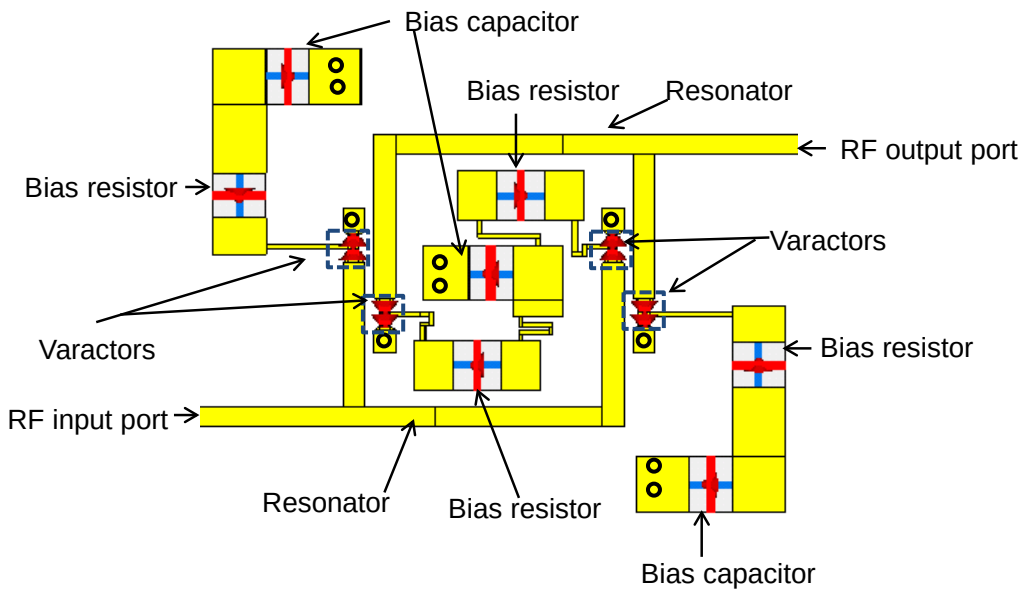

Figure A.1: Layout of the two-pole hairpin filter with tunable BST varactors and 0° feed structure.

design, there are actually only two-resonators — a single half-wavelength open resonator is folded to form one hairpin resonator. There are two such hairpin resonators in this design. Barium strontium titanate (BST) based varactors connected in series with the transmission line resonators make them tunable and also shorten the resonant length of the transmission lines. It must be noted that this filter structure uses a 0° feed structure, i.e. the signals at the input and output feed points are in phase at resonance. A 0° feed structure is preferred over a 180° feed structure (when the signals at the input and output feed points are out of phase at resonance) as two-transmission zeroes on either sides of the passband are generated giving rise to the quasi-elliptic filter response [72, 84].

The filter is simulated in Computer Simulation Technology's Microwave Studio (CST MWS). Hybrid EM simulation (EM-circuit co-simulation) of the complete filter circuit is performed. An alumina substrate with a dielectric permittivity (ϵ_r) of 9.9, thickness of 381 μm, and a loss tangent ($\tan\delta$) of 0.0002 is considered in the simulation. The integrated BST capacitors are treated as lumped elements and are simulated together with the rest of the microstrip filter

Table A.1: Filter Design Details.

Design details	Value
Resonator coupling length	659 μm
Inter-resonator spacing	170 μm
BST varactor value	1.2 pF
Bias capacitor	20 pF
Bias resistor	3 kΩ

layout. This is done to reduce the simulation time without trading off the accuracy of the results. All electromagnetic (EM) simulations here are lossless. The metal traces used in the design are considered lossless. Full-EM simulation of the integrated BST varactor used in the design is not performed and hence the equivalent resistance associated with the BST capacitor is not available. The bias resistors and capacitors used in the design are treated as lumped elements and are identified in Figure A.1. Table A.1 provides the filter design and layout details.

Figure A.2 is the lossless EM simulation result of the filter with zero-bias BST capacitor values. The filter has a 3-dB bandwidth of 0.49 GHz at a center frequency of 3.46 GHz. Figure A.3 is the lossless EM simulation tuning result of the filter with a 2:1 varactor tuning ratio. The tunability of the filter based on the simulations is 20%.

A.3 Filter Fabrication

The filter was fabricated using the same processing steps as that used for the two-pole modified combline filter discussed in Chapter 5. The steps are repeated here so that the fabrication process is clear.

The filter was fabricated using an alumina substrate chosen for its low cost, the close match of its thermal coefficient of expansion to that of BST, and its low loss tangent [60, 61]. Here the alumina substrate has a thickness of 381 μm, dielectric permittivity (ϵ_r) of 9.9, and a loss tangent ($\tan\delta$) of 0.0002. The thermal expansion match prevents the BST from cracking when

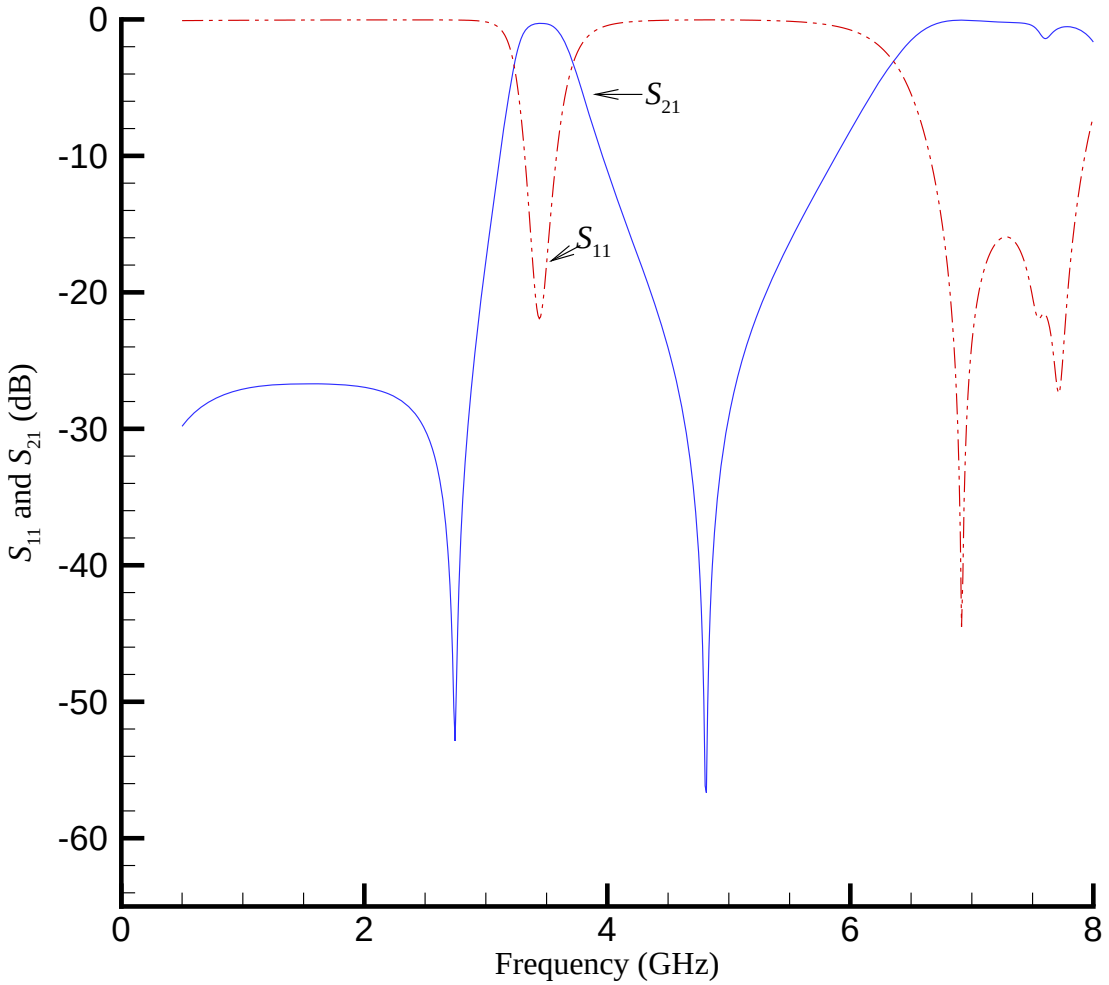

Figure A.2: Simulated lossless S_{21} and S_{11} results of the filter with zero-bias BST capacitor values. The filter has a center frequency of 3.46 GHz and a 3-dB bandwidth of 0.49 GHz. It has a return loss of 22 dB.

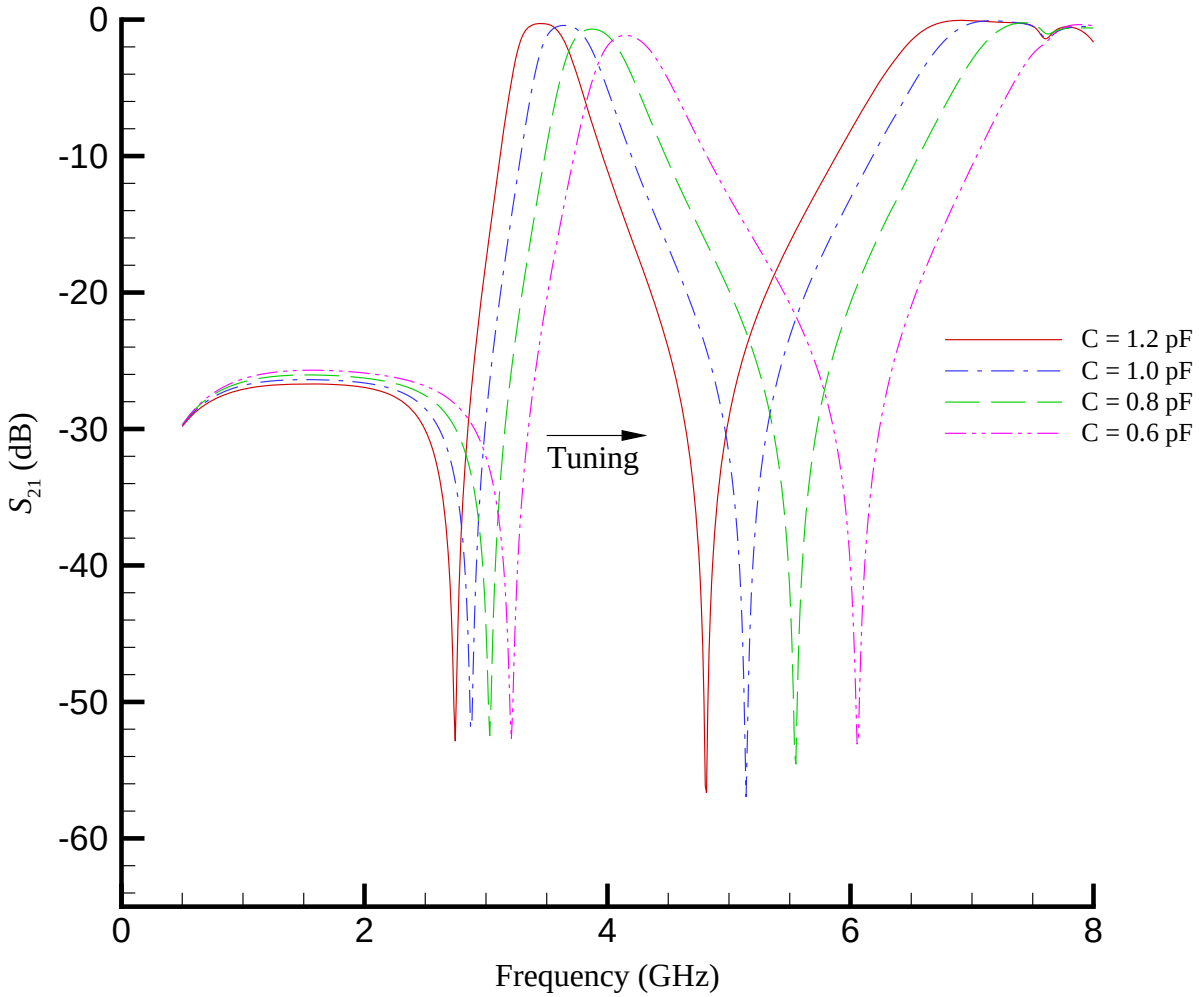

Figure A.3: Simulated S_{21} results. The filter tunes from 3.46 GHz to 4.14 GHz with a tunability of 20%.

subjected to high heat in the annealing step. The alumina substrates were polished on both sides by Coorstek Inc, Colorado. Via holes (150 μm in diameter) were laser drilled by LPT Inc, Oregon. These vias were then filled with a gold/glass frit and cured at 900°C by Hybrid-Tek, New Jersey. Magnetron sputtering was used to deposit a 0.70 μm-thick BST film across the wafer in a vacuum chamber for 2 hours with the following processing conditions: power density of 2.5 Watts/cm^2, deposition pressure of 10 mTorr, and deposition temperature of 300°C. After deposition, the dielectric was masked and patterned using a single layer photolithography step followed by etching using a 10% hydrofluoric solution for 2 minutes. This step was performed in order to remove BST from all areas of the substrate except where the varactors are located. The substrate was then annealed in air at 900°C for 20 hours which fully crystallized and densified the dielectric film.

Metallization of the device was performed in two steps. The initial metallization step consists of a sputtered chromium (Cr) layer followed by a layer of gold, 10 and 200 nm thick respectively. This metal stack was patterned and etched with a single layer photolithography step and ion beam etched. The patterns for this initial metallization consists of the interdigitated capacitors and the biasing lines. The bottom layer substrate metallization also consists of a Cr/Au metal stack providing a seed layer for the electroplating step. The second metallization step built up the rest of the circuit: the resonators; the input and output feed-lines; and the resistor pads. The metal stack from this step was patterned using single layer lithography which was then followed by a 450 nm thick silver film deposited by magnetron sputtering and patterned by lift-off. Finally the device was electroplated with copper up to a total thickness of 5 μm. The IDC fingers are masked with a photoresist layer before the electroplating step was performed to prevent shorting between the fingers. It should be noted that the entire device was plated except for the immediate region of the varactors [60].

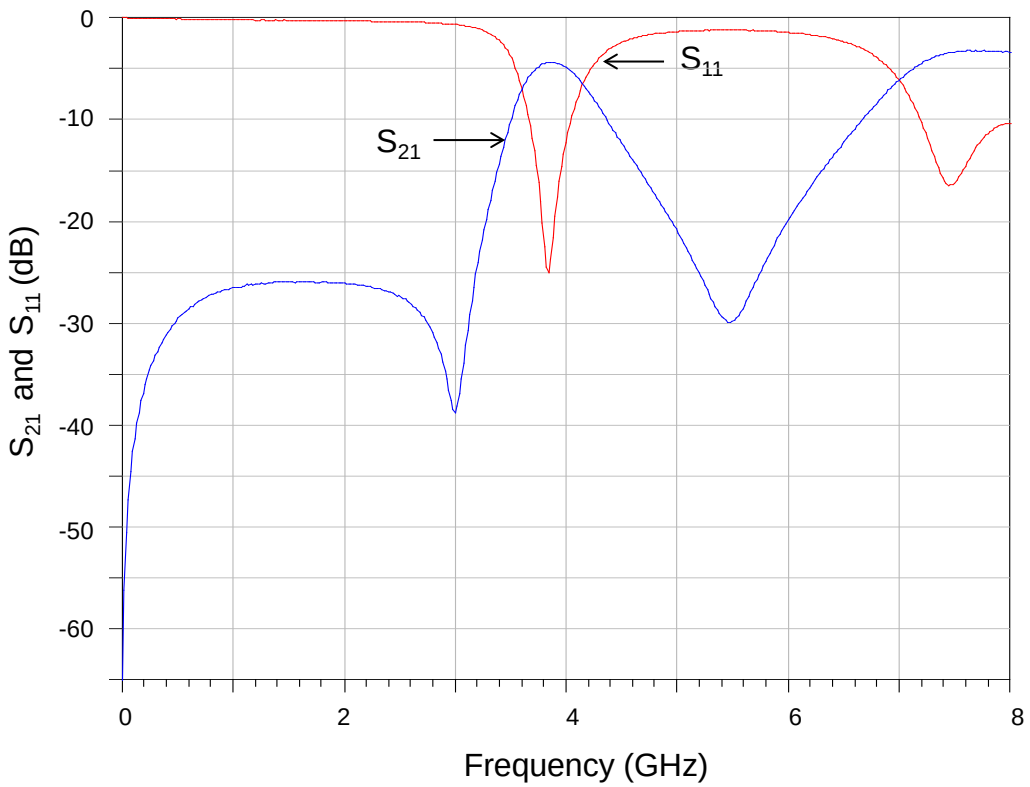

Figure A.4: Measured S-parameter result of the filter fabricated based on the layout in Figure A.1. The measurements were taken before assembling the surface mount bias resistors and capacitors. The measured insertion loss is 4.4 dB and 3-dB bandwidth is 0.62 GHz at a filter center frequency of 3.89 GHz. The return loss is 25.09 dB.

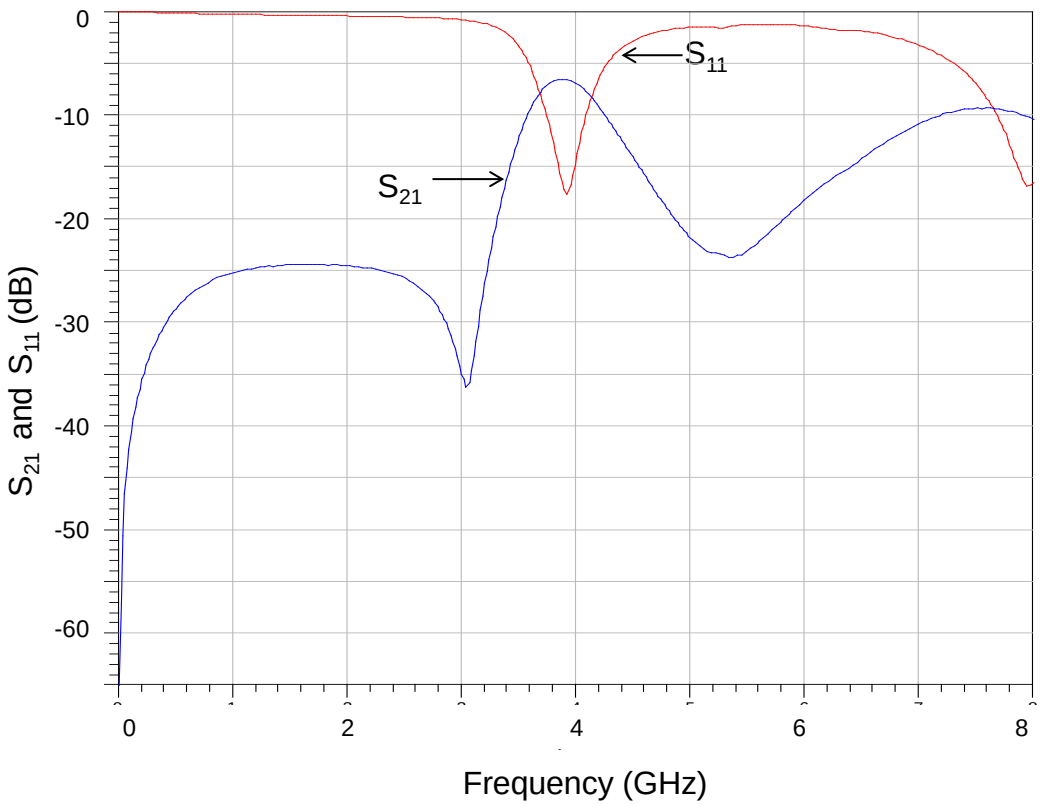

Figure A.5: Measured S-parameter result of the filter fabricated based on the layout in Figure A.1. The measurements were taken after assembling the surface mount bias resistors and capacitors. The measured insertion loss is 6.56 dB and 3-dB bandwidth is 0.62 GHz at a filter center frequency of 3.89 GHz. The return loss is 17.61 dB

A.4 Measured results

Figure A.4 shows the measured zero-bias S-parameter result of the filter without mounting of the bias capacitor and resistor chips. The results indicate a low insertion loss of 4.4 dB with a bandwidth of 0.62 GHz at a center frequency of 3.89 GHz.

Figure A.5 shows the measured S-parameter result after the bias capacitors and resistors were assembled on the filter circuit. The results indicate an insertion loss of 6.56 dB with a bandwidth of 0.62 GHz at a center frequency of 3.89 GHz. These results indicate that adding the bias chips increased the insertion loss by 2 dB. The close proximity of the bias resistors and capacitors to the resonators could be a possible cause for the increase in insertion loss and requires further investigation.

A.5 Conclusion

A prototype of the two-pole ferroelectric based hairpin resonator filter topology with a quasi-elliptic filter response was successfully designed, fabricated and characterized. The center frequency of the measured filter was higher than the designed value of 3.46 GHz as the fabricated capacitor values were lower (around 0.8 pF) than the design value of 1.2 pF. Initial zero-bias measured results indicated a low insertion loss of 4.4 dB. However, the loss increased by 2 dB once the bias resistors and capacitors were assembled on the filter circuit. The reasons behind this increase in loss requires further investigation. While the initial results are promising, additional design improvements will be required to further optimize the filter design, improve the width of the stopband and explore the tunability of the fabricated filter.